EPID-based 3D dosimetry for pre-treatment IMRT/VMAT Quality Assurance

Abdulaziz Alhazmi

München, 2018

EPID-based 3D dosimetry for pre-treatment IMRT/VMAT Quality Assurance

Abdulaziz Alhazmi

Dissertation
der Fakultät für Physik
der Ludwig-Maximilians-Universität
München

vorgelegt von

Abdulaziz Alhazmi
geboren in Makkah

München, den 19.11.2018

Erstgutachter: Prof. Dr. Katia Parodi
Zweitgutachter: Prof. Dr. Marco Riboldi
Tag der mündlichen Prüfung: 17.12.2018

Zusammenfassung

Die Behandlung von Krebs mit Photonenstrahlung hat sich in den letzten Jahrzehnten rasant entwickelt mit dem Ziel, das therapeutische Verhältnis zu verbessern, indem dem Tumor eine letale Dosis verabreicht wird bei gleichzeitiger Schönung des benachbarten, normalen Gewebes. Da der Erfolg der Krebstherapie von der Qualität der Dosisabgabe abhängt, wurde ein Qualitätssicherungsprogramm (QA, Quality Assurance) etabliert, um eine systematische Überwachung der Qualität und Angemessenheit der Patientenbehandlung durch die sogenannte Bestrahlungskette der Strahlentherapie sicherzustellen. Solch ein Programm sammelt Informationen aus verschiedenen Bereichen der Medizinischen Physik. Die Hauptaufgabe von Medizinphysikern besteht insbesondere darin, die Abgabe der geplanten Dosis an den Patienten sicherzustellen, wobei die Unsicherheit unter den international anerkannten Grenzwerten liegen soll. Die Bestrahlung ist jedoch mit der Entwicklung der Technologie komplizierter geworden. Daher ist die Entwicklung fortschrittlicher QA-Werkzeuge und -Methoden für neue Ausrüstungen und Techniken erforderlich. In der Praxis werden verschiedene QA-Protokolle verwendet, die auf kommerziellen oder selbstentwickelten Tools und Methoden basieren, um internationalen Empfehlungen Rechnung zu tragen. Die gegenwärtige Praxis hat jedoch Beschränkungen, entweder aufgrund der Abhängigkeit von Dosisberechnung oder Dosierungssystemen, was ein arbeitsintensives Verfahren oder mangelnde Genauigkeit impliziert. Das Ziel dieser Arbeit ist die Entwicklung eines QA-Tools für die patientenindividuelle Qualitätssicherung vor der Behandlung. Dieses Werkzeug ist ein dosimetrischer Ansatz, der schnell, genau und dreidimensional (3D) ist, unabhängig vom Behandlungsplanungssystem (TPS, treatment planning system) und der Abgabemaschine, dabei sensitiv für inhärente Fehler. Das Electronic Portal Imaging Device (EPID) ist ein planarer Detektor, der starr an modernen Linacs befestigt ist, die für Bildgebungszwecke verwendet werden. Da diese Detektortypen über dosimetrische Merkmale verfügen, wurden diese Merkmale des EPID, das an der Abteilung für Radiologie Onkologie der Universitätsklinik München (Klinikum der Universität München, Ludwig-Maximilians-Universität) installiert wurde, explizit untersucht. Ausgehend von den Erkenntnissen aus der EPID-Charakterisierung wurde ein Verfahren zur Kalibrierung des als Dosimeter in Wasser zu verwendenden EPID vorgestellt, wodurch das aus dem EPID gewonnene zweidimensionale (2D) Bild in eine 2D-Dosisverteilung umgewandelt werden kann. Die Genauigkeit der Kalibrierungsmethode wurde anhand der weit verbreiteten Gamma-Bewertung gegenüber Referenzdosimetern validiert. Das vorgeschlagene Verfahren liefert die 2D-Dosisverteilung mit einer Genauigkeit, die mit der Referenz von Dosimetern in einem Wassermedium vergleichbar ist, jedoch mit einer besseren räumlichen Auflösung und kürzeren Aufbauzeiten. In Anbetracht der Einführung neuer Behandlungstechniken wie der intensitätsmodulierten Strahlentherapie (IMRT, intensity modulated radiation therapy) und der volumetrisch modulierten Arc-Therapie (VMAT) ist eine Validierung unter dynamischen Gantry-Bedingungen von entscheidender Bedeutung, um festzustellen, ob die richtige Dosis unter dem richtigen Gantry-Winkel abgegeben wird. Zu diesem Zweck ist ein dreidimensionaler Dosimetrieansatz erforderlich. Daher wurde in dieser Arbeit ein neuartiger Ansatz zur Rekonstruktion einer 3D-Dosisverteilung aus 2D-Dosisverteilungen entwickelt. Eine Reihe mathematischer Operationen wurde implementiert, um eine 3D-Verteilung zu erzeugen, die mit der gewünschten räumlichen Auflösung übereinstimmt und eine mit der TPS-Dosisberechnung vergleichbare Genauigkeit aufweist. Die Operationen wurden

in einen Algorithmus eingebettet, der die 2D-Dosisverteilungen auf verschiedenen Stufen rückprojiziert und so eine 3D-Dosisverteilung in einem virtuellen zylindrischen Phantom bildet (rekonstruiert). Die rekonstruierten 3D-Dosisverteilungen wurden unter Verwendung der Gamma-Bewertung mit allgemein empfohlenen Kriterien (3%, 3 mm) für herkömmliche und komplexe klinische Behandlungspläne gegenüber Referenzmessungen validiert. Die Auswertung der verschiedenen IMRT- und VMAT-Pläne hat gezeigt, dass die Übereinstimmung den allgemeinen Toleranzwert (d. h. 95%) eingehalten hat. Da das QA-Instrument in der Lage sein sollte, dosimetrische und geometrische Ungenauigkeiten zu erkennen, wurde die Sensitivität der entwickelten Rekonstruktionsmethode bei beabsichtigten Abweichungen der Dosisabgabe in Bezug auf den Referenzplan bewertet. Es wird gezeigt, dass die Rekonstruktionsmethode in der Lage ist, geometrische Fehler des Multilamellenkollimator (MLC, multileaf colimator) in der Größenordnung von 2 mm, eine Winkelverschiebung des Portalwinkels von 1 Grad und einen dosimetrischen Fehler von $\pm$ 4% zu erkennen. Die entwickelte Arbeit stellt eine bevorzugte Methode gegenüber anderen in der Literatur vorgeschlagenen und auch gegenüber kommerziellen Geräten vor. Der Ansatz ist prädiktionsfrei, schnell und einfach in der klinischen Routine zu implementieren. Ausgehend von einer Aufnahme an Luft wird eine wasseräquivalente 3D-Dosisverteilung mit relativ hoher Auflösung ohne externes Phantom oder Dosimetriegerät erstellt. Der vorgeschlagene Ansatz erhöht somit die Effizienz und Genauigkeit der QA-Protokolle in der Strahlentherapie. Es ist möglich, die vorgeschlagenen Arbeiten in ein umfassendes patientenspezifisches QA-Programm zu integrieren, welches auch eine auf MC basierende Dosisberechnung und die vollständige Automatisierung des gesamten QA-Verfahrens umfasst.

Abstract

Treatment of cancer using photon radiation has rapidly developed in the last few decades. The development has aimed at improving the therapeutic ratio by delivering a lethal radiation dose to the tumor with sparing adjacent normal tissue. As the success of cancer radiation therapy depends on the quality of dose delivery, a Quality Assurance (QA) program has been established to assure the objective of systematic monitoring of the quality and appropriateness of patient care through the radiotherapy treatment chain. While such a program requires inputs from different disciplines, the primary task of medical physicists, in particular, is to ensure the delivery of the planned dose to the patient with an uncertainty below internationally accepted limits. However, the dose delivery has become more complicated with the development of technology. Hence, the development of advanced QA tools and methods to accommodate new equipments and techniques is required. In practice, different QA protocols relying on commercial or -in-house- developed tools and methods are used to accommodate international recommendations. However, the current practice has limitations due to either dependency on dose calculation or dose delivery systems, implying labor intensive procedure or lack of accuracy. The aim of the thesis is to develop a QA tool for patient-specific pre-treatment QA. The tool is to be identified as a dosimetric approach which is fast, accurate, three-dimensional (3D), independent of the treatment planning system (TPS) and delivery machine and sensitive to error. Electronic Portal Imaging Device (EPID) is a planar detector rigidly attached to modern linacs used for imaging purposes. As these types of detectors offer dosimetric features, the dosimetric characteristics of the EPID installed at the Department of Radiation Oncology of the University Clinic of Munich (Klinikum der Universität München, Ludwig-Maximilians-Universität) have been explicitly investigated. Making use of the knowledge gained from EPID characterization, a method to calibrate the EPID to be used as a dosimeter in water has been presented, thus converting the two-dimensional (2D) image, as acquired from EPID, into a 2D dose distribution. The accuracy of the calibration method has been validated against reference dosimeters by using the widely used gamma evaluation. The proposed method provides the 2D dose distribution with accuracy comparable to reference dosimeters in a water medium but better spatial resolution and set-up time efficiency. However, considering the introduction of new treatment techniques such as Intensity Modulated Radiation Therapy (IMRT) and Volumetric Modulated Arc Therapy (VMAT), a validation under dynamic gantry condition becomes crucial to determine that the correct dose is delivered at the correct gantry angle. For this purpose, a 3D dosimetric approach is required. Hence, a novel approach to reconstruct a 3D dose distribution from 2D dose distributions has been developed in this thesis. A series of mathematical operations have been implemented to generate a 3D distribution matching the desired spatial resolution and having comparable accuracy with the TPS dose calculation. The operations have been embedded in an algorithm that back-project the 2D dose distributions at different levels thus forming (reconstructing) a 3D dose distribution in a virtual cylindrical phantom. The reconstructed 3D dose distributions have been validated using gamma evaluation with commonly recommended (3%, 3 mm) criteria for conventional and complex clinical treatment plans against reference measurements. The evaluation for the different IMRT and VMAT plans has resulted in passing rate exceeding the common

tolerance level (i.e. 95%). As the rationale of the QA tool is to be capable of detecting dosimetric and geometric inaccuracy, the sensitivity of the developed reconstruction methodology has been evaluated in the presence of intentional dose delivery deviations with respect to the reference plan. The reconstruction methodology has demonstrated to be sensitive to geometric errors of the multi-leaf collimator (MLC) in the order of 2 mm, gantry angle shift of 1 degree and dosimetric error of $\pm 4\%$. The developed work presents a preferable methodology over others proposed in the literature and also over commercial devices. The approach is prediction-free, fast and easy to implement in clinical routine. Starting from an in-air acquisition, a water equivalent 3D dose distribution with relatively high resolution is obtained without an external phantom or dosimetric device. Thus, the proposed approach adds efficiency and accuracy to QA protocols in radiation therapy. The proposed work is foreseen to be integrated into a comprehensive patient-specific QA program including an MC based dose calculation and full automation of the whole QA procedure.

Contents

Chapter 1

Introduction and Motivation

Cancer is a group of diseases defined by an abnormal cell growth in any body organ spreading to another organ in a process called metastasizing. Metastases are the primary cause of death from cancer. Globally, cancer is the second leading cause of death [1] [2]. In 2013, there were 14.9 million incident cancer cases and 8.2 cancer-related deaths recorded worldwide [3]. Scientists predict that 23.6 million cases will be diagnosed with cancer worldwide each year by 2030 [4]. In order to fight this major societal challenge, three major types of treatment are typically adopted, individually or more often in combination. Namely: surgery, chemotherapy, and radiotherapy. Less common procedures and techniques for cancer treatment include immunotherapy, targeted therapy, stem cell transplant and hormone therapy. Choosing the adequate type of treatment depends on the cancer type and location. The treatment plan can include one or a combination of types mentioned above. However, radiotherapy is involved in about 50% of cancer treatment course in Europe and the US [5] [6]. Radiotherapy is based on the use of ionizing radiation (photons, electrons, ions and -in a few cases- neutrons) to deliver conformal dose (i.e. energy per mass) to the cancer target. Radiotherapy aims to improve the therapeutic ratio by delivering a lethal radiation dose to the tumor with sparing adjacent normal tissue.
Using photon for cancer treatment has begun in 1896 shortly after the discovery of X-rays by Röntgen. Since then, a substantial improvement in modalities and techniques has been implemented up to our current day.
An overview of the state of the art of radiation therapy modalities and techniques will be presented in this chapter. Then, a brief description about quality assurance programs in clinics will be addressed. Finally, the aim of this thesis will be presented.

1.1 Modern radiation therapy

Radiation therapy can be delivered using different modalities. Modalities are categorized based on the location of the radiation source relative to the patient (i.e. external or internal) and the type of radiation. Independently of the delivery modalities, the process starts, in general, with the treatment planning based on a patient image obtained using X-ray Computed Tomography (CT). Recently, functional and/or anatomical imaging modalities such as Positron Imaging Tomography (PET) and Magnetic Resonance Imaging (MRI) have been introduced to complement the anatomical information of the CT images(s) [7]. The tumor and the normal tissue are delineated and contoured on the patient image. The radiation delivery technique is chosen based on clinical consideration, including shape, size and location of the tumor. A brief description of radiation delivery modalities is given in the following:

1.1.1 External radiation therapy

1.1.1.1 Photon external radiation therapy

Photons with high energy ($\sim$ MeV) either emerge from a nucleus (gamma irradiation) or originated from its orbits (X-ray) are used to deliver a conformal dose to patients. Specifically, gamma rays originate from radioactive nuclei, while X-rays originate in a target bombarded with energetic electrons. The technologies used for dose delivery purpose include Linear accelerator (linac), Gamma knife, Tomotherapy and cyberknife [8]. The most common and versatile technology in use in clinics worldwide is the linac whereas the other modalities are designed to treat specific cancer types and locations. Since the linac is also the technology of interest in this work, a more detailed description will follow in section 2.3.

1.1.1.2 Particle external radiation therapy

The external radiation treatment in particle therapy uses accelerated beams (up to few hundreds MeV/u) of protons or heavier ions. By definition, electron and neutron therapy may also be categorized as particle therapy. But due to its different source and type of interactions, particle therapy is usually referred to ion beam therapy to exclude the electrons and neutrons. Ions have different dosimetric characteristics than the more widely used photons when traversing media. In water, the typical energy deposition of the photon beam is exponentially decreasing with depth after the build-up region. Differently, ions show a steady energy deposition for a certain depth and then a steep rise to the peak (the "Bragg peak") near the end of their range (figure 1.1) [8]. These characteristics of ions give the advantage in treatment by depositing the maximum energy within the target (the tumor) and sparing the healthy tissue from unwanted energy deposition. Although this

advantage represents a game changer in radiation therapy, it has not yet been considered for (entirely) replacing conventional photon therapy. It is argued that though the physics of particles and their interaction with matter are well understood, delivering them accurately and safely to the desired target area in a patient still has considerable uncertainties. Besides, the biological effectiveness of ion beams to tumor is not fully understood [9]. In addition, the technology of particle therapy is too expensive at present. For example, the cost of linear accelerator technology with proton therapy is higher in the order of 10-20 times more than photon therapy unit with the same technology. On the other hand, carbon ion therapy unit is about 100 times more expensive than proton therapy unit. [9].

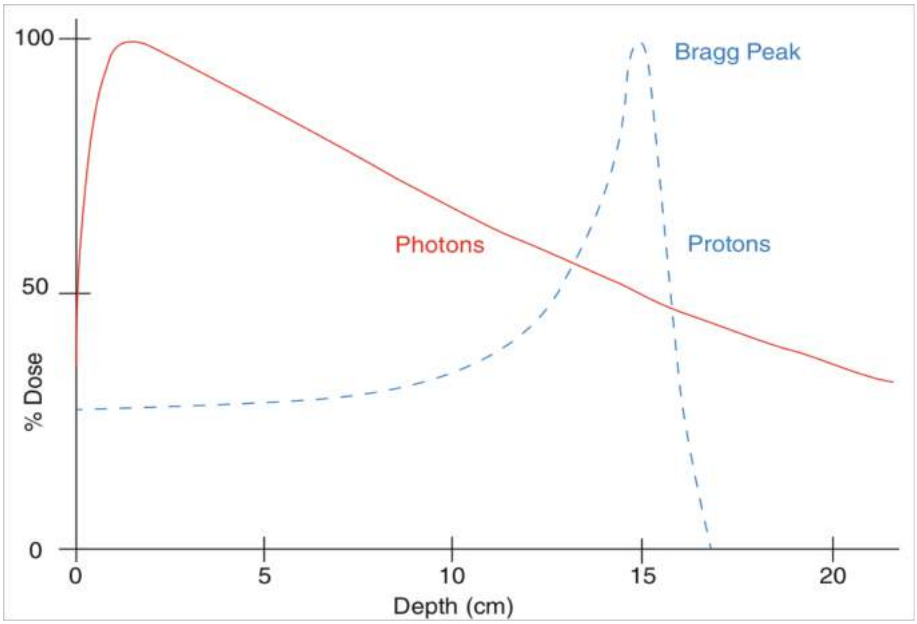

Figure 1.1: Typical depth dose characteristics of protons and photons in water [9].

1.1.2 Internal radiation therapy

1.1.2.1 Sealed source radiation therapy

Sealed source radiation therapy or so-called (brachytherapy) is a form of therapy performed by positioning a sealed source emitting high dose or low dose rates of beta and/or gamma radiation next to the desired tumor for a certain irradiation period. According to the type and location of the tumor, the treatment uses either interstitial, intracavitary, or surface application. The usage of brachytherapy gives the advantage of treating the tumor with typically a lower integral dose to normal tissue than external radiation therapy. The wide range of sources which can be used for this treatment (e.g. Cs^{137}, Ir^{192}, Au^{198}, I^{125}, and Pd^{103}) offers flexibility in choosing the appropriate radiation energy and half-time of the radionuclide. Additionally, technical developments are in the direction of artificial manipulation of sources sizes, shape and activity to fulfill the clinical requirement [8].

1.1.2.2 Unsealed source radiation therapy

In contrast to sealed source radiation therapy, unsealed source radiation therapy is a method where radioactive substances are injected (or ingested) to a patient in order to target a specific organ using the chemical properties of the a tracer to which the radioactive isotope is bound, and the behavior of the digestive and circular systems of the human body. The method uses a similar concept as functional diagnostic imaging in nuclear medicine but different types and quantities of radiopharmaceuticals. However, unsealed source radiation therapy is confined to a few clinical usages or applications. (I^{131}) used to treat thyroid cancers and (Ra^{223}, Sr^{89} or Sm^{153}) used to treat bone metastases [8].

1.2 Linac-based radiation therapy techniques

Modern linacs in combination with auxiliary dose delivery systems provide different techniques of external radiation therapy based on 3D anatomical information provided by CT and/or PET and MRI. A description of the most common techniques, with focus on those related to the thesis scope, is pointed out in the following.

1.2.1 Three-dimensional Conformal Radiation Therapy (3D-CRT)

3D-CRT is a treatment technique making use of several treatment projection angles and complex fields defined by Multileaf collimator (MLC) to geometrically conform the therapeutic dose as close as possible to the target volume based on ”forward treatment planning” method. Most treatments are delivered with a flattened beam (made uniform by the use of flattening filters) and with uniform intensity across the field (within the flatness specification limits). Physical and non-physical wedges or compensators are occasionally used to modify the intensity profile to correct for contour irregularities of the human body in order to produce more uniform dose distribution [8]. Figure 1.2 illustrates a typical six-field technique to treat a prostate tumor case using 3D-CRT.

1.2.2 Intensity Modulated Radiation Therapy (IMRT)

IMRT is based on the delivery of several treatment fields that adapt the therapeutic dose according to a modulation of the photon fluence. In addition to the use of different projection angles and different MLC fields than used in 3D-CRT, the dose can be more optimized to the target volume utilizing a nonuniform intensity beam. Intensity modulation is performed by MLC modulation in step-and-shoot (segmental) or sliding-window (dynamic) fashions per projection angle. The planned fluence is electronically transmitted to the synchronized MLC and linac for treatment delivery. A linac control system guarantees

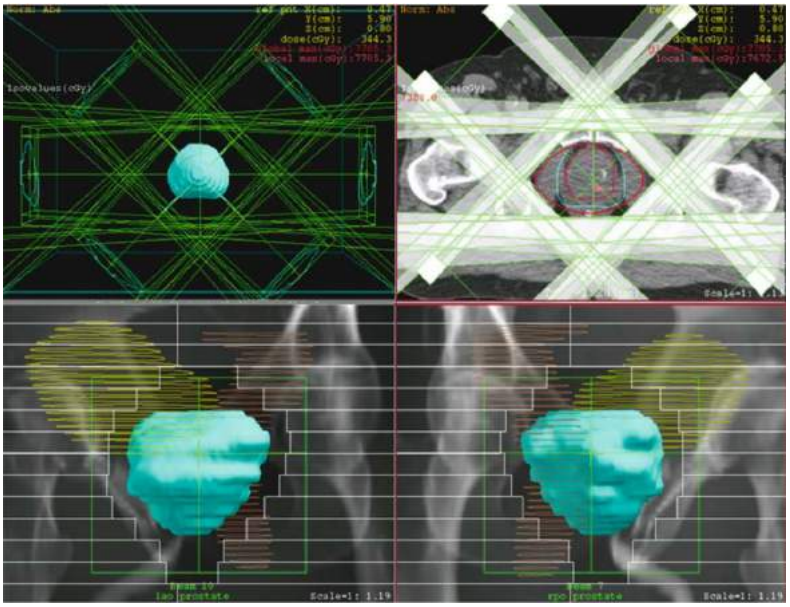

Figure 1.2: The upper left panel displays a six-field 3D beam arrangement for a prostate case viewed along the superior-inferior axis. The upper right panel shows the uniform conformal dose zones (red line) covering the tumor volume and prostate in the isocenter axial plane. Lower panel displays a beam shaping relative to the contour of the tumor volume (solid light blue) and shielding of of the rectum (brown wire cage) and bladder (yellow wire cage) [10].

the integration of treatment planning and delivery to ensure accurate and efficient data transfer [11].

1.2.3 Volumetric Modulated Arc Therapy (VMAT)

VMAT is based on the delivery of a rotational cone beam with variable shape and beam intensity. As an advanced form of IMRT, VMAT delivers the dose continuously as the gantry rotates, leaves shift and dose rates change. The planner optimizes field shape and beam intensities for a large number of projection angles, according to one or two full gantry rotations. Unlike IMRT, the projection angles are not fixed, and the angular resolution and rotational speed are dependent on the linac. However, the MLC movements and the gantry rotation have to be synchronized to deliver the exact field shape at the exact projection angle as planned. The large number of projection angles gives the advantage of more conformal dose to the tumor and better sparing for organs at risk than the fewer fixed projections used in IMRT. Moreover, VMAT is usually preferred to IMRT because of superior delivery efficiency. The amount of saved time in comparison to other techniques is dependent on the adopted system and the planning protocol of the specific clinic [12].

Typical dose distributions for the treatment of prostate tumor using the described three techniques are illustrated in figure (1.3).

1.2.4 Stereotactic Body Radiation Therapy (SBRT)

SBRT refers to a technique that uses ultrahigh doses and precise treatment fields to be delivered in a lower number of fractions than conventional techniques. The higher dose rate brings more fatality to the fast recovering tumor cells but requires additional measures for dose conformation. For instance, the penumbra (fall-off) region around the radiation field has to be well-defined to minimize the dose to normal tissue or more importantly organs at risk. Accordingly, the dose delivery accuracy is of critical importance when using this technique. Thus, the recommended tolerance level for SBRT is more restrictive in comparison to other radiation therapy techniques [13].

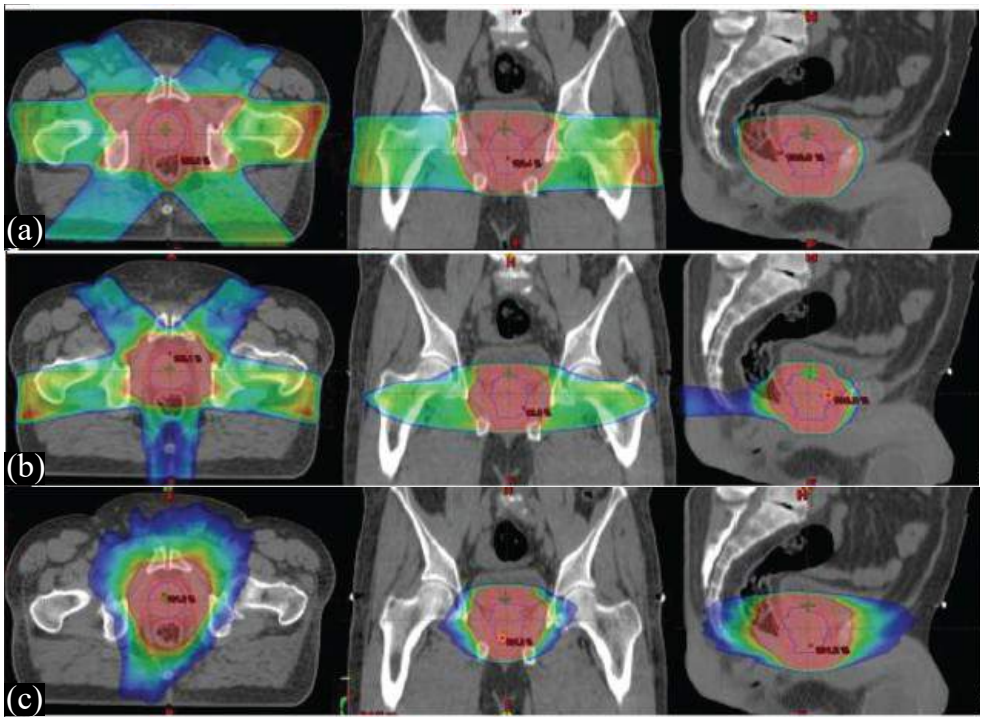

Figure 1.3: Dose distributions for the treatment of prostate tumor using different techniques (a) 3D-CRT (b) IMRT and (c) VMAT (adopted from [12]).

1.3 Quality assurance for radiation therapy

”The purpose of a quality assurance program is the objective, systematic monitoring of the quality and appropriateness of patient care. Such a program is essential for all activities in radiation oncology. The quality assurance program should be related to structure, process and outcome, all of which can be measured. Structure includes the staff, equipment, and facility. Process covers the pre- and post-treatment evaluations and the actual treatment application. Outcome is documented by the frequency of accomplishing stated objectives, usually tumor control, and by the frequency and seriousness of treatment-induced sequelae” [14]. Thus, the quality assurance (QA) program in radiation therapy

includes efforts from different disciplines. With reference to figure 1.4, each step requires inputs either from the radiation oncologists, physicists, engineers or therapists. Although medical physicists are more involved in the technical than medical aspects of QA, their efforts substantially interplay with those of the other groups. In particular, the primary task of medical physicists is to ensure the delivery of the planned dose to the patient with an uncertainty inferior to 5% [15].

Uncertainties in treatment can be systematic and random. While the random errors cannot be controlled, the systematic errors can be controllable if a comprehensive QA program is conducted. In the framework of linac based radiation therapy, the program should be able to catch errors of different origins including: (a) linac output, (b) patient image used for treatment planning, (c) dose calculation in the patient image, (d) data transfer between the TPS and the linac control system and (e) daily variations in patient positioning (e.g. using inaccurate positioning lasers within treatment room). The rapid evolution of more conformal dose delivery combined with the advancement in imaging techniques is adding potential for improving the therapeutic ratio between tumor and normal tissue response. However, the new advances have resulted in a recognized need for greater accuracy tests in the radiation treatment process [16]. Thus, national and international organizations provide local clinics with QA regulations and recommendations for these specific techniques. Unfortunately, the regulations are general and usually cannot keep pace with development in technology [10]. The lack of specific QA guidelines makes the clinics develop their own protocols depending on in-house or commercial methods and detectors [17]. Especially for delivery QA, the developed programs are focused on detecting IMRT/VMAT related errors which cannot be detected by conventional QA procedures used for the conventional treatment techniques. Relevant aspects to tests for correct beam delivery include: accuracy and reproducibility of the MLC leaf positioning, measurements of the inter- and intra-leaf leakage, leaf speed control, dose and dose rate linearity and -specifically for VMAT- gantry rotational speed.
After having established these procedures, several clinics start to implement a pre-treatment patient-specific QA for IMRT/VMAT plans in their practice. Implementation of patient-specific pre-treatment QA proved to be crucial for treatment chain but needs more investment in human resources and machine time [18]. Research communities are working on optimization of QA tools to perform comprehensive tests more efficiently.

1.4 Rationale for EPID based dosimetry

Delivering the intended radiation dose to the patient is a complex process. The assurance of the correct dose delivery needs equipment that accurately measures the dose with high spatial and temporal resolutions. Additionally, in IMRT/VMAT techniques, a 3D dosimeter is desirable. The required features are not available in a single commercial device. Thus, physicists use different dosimeters to satisfy these requirements. In practice, the QA time efficiency is becoming an essential aspect of QA procedure. Optimizing the set-up and processing time of current dosimetric methods without sacrificing the testing

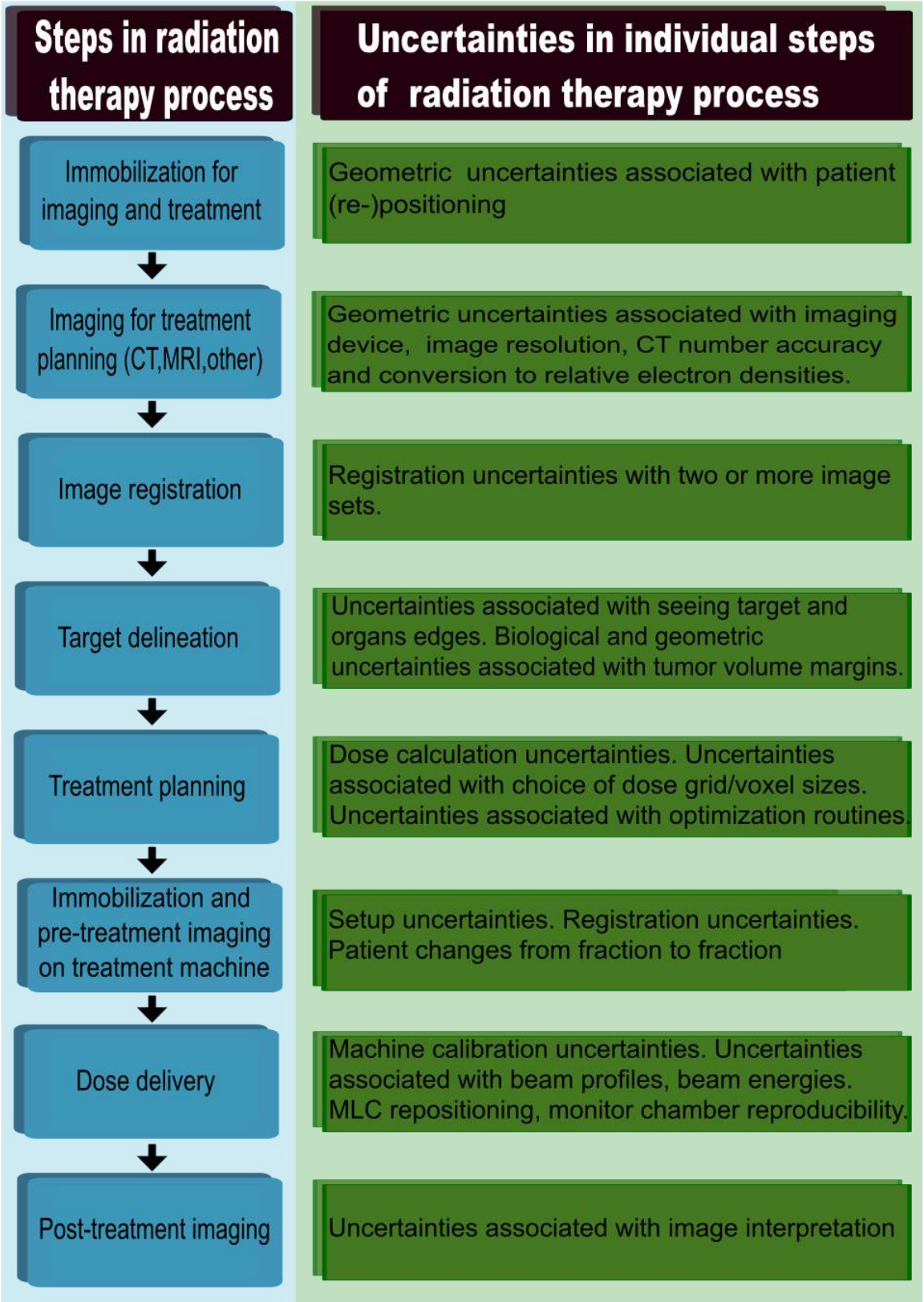

Figure 1.4: Steps in radiation therapy process and major uncertainties associated with each step (adapted from [18]).

quality is a goal. Hence, it is desirable to identify a dosimeter which is fast, accurate, 3D, independent of TPS or delivery machine and sensitive to error dosimeter.

Electronic Portal Imaging Device (EPID) is a planar detector rigidly attached to modern linacs with a primary function of 2D anatomical imaging of the patient prior to treatment. It has been used for more than a decade for positioning verification. Prior to dose delivery, the oncologist checks the alignment of bony structures or other landmarks between EPID images acquired on-site and reference images. The reference image is a digitally reconstructed radiograph (DRR), which is a virtual radiograph generated by simulating the X-ray transport into the patient CT and incident onto the detector plane [19].
Despite being used for imaging, EPID has been found as a candidate tool for QA. It provides a relatively large detection area with a high spatial resolution. It requires no set-up time and generates real-time images with sub-second temporal resolution which with special computational approaches can be used to generate 3D dose distribution, as will be discussed in chapter 3.

1.5 Thesis context and objective

The aim of this thesis is to develop a novel method to reconstruct a 3D dose distribution using EPID technology for pre-treatment QA. The investigated 3D dosimetry is tailored to IMRT/VMAT treatment plans. The dose reconstruction algorithm is implemented and tested based on the equipment installed at the Department of Radiation Oncology of the University Clinic of Munich (Klinikum der Universität München, Ludwig-Maximilians-Universität). To illustrate the roadmap towards achievement of this goal, the content of the thesis is divided into steps that span from the physics background of the EPID technology to the performed experiments in the clinic.

In particular, chapter 2 explains the physics of photon and particle interactions with matter and presents a theoretical description of the radiation detectors typically used in clinics and the clinical X-ray generation among those techniques that are of interest for the thesis. Chapter 3 illustrates the technology of EPID and signal acquisition as well as image processing. Chapter 4 presents the dosimetric characteristics of the EPID in comparison to other dosimeters used in clinics followed by a complete literature review of the different approaches to EPID dosimetry. Then, chapter 5 outlines the proposed novel method for calibrating the EPID to produce a 2D dose distribution. The chapter then explains the novel dose reconstruction method in chapter 6. The explanation includes a step by step verification and result illustration. The overall accuracy in comparison to different dosimetry methods is illustrated at the end of the chapter, with evaluation of IMRT/VMAT treatment plans of real clinical cases. Chapter 7 presents the tests of the sensitivity of the proposed method detecting delivery errors along a description of the experiment design and result. Chapter 8 is dedicated to discuss the findings and the potential usage of the proposed dose reconstruction method with a comparison to other methods. The thesis ends with a chapter giving the summary of the work and putting forward perspectives for the development of radiation therapy QA.

Chapter 2

Fundamentals of radiation therapy and dosimetry

2.1 Interaction of radiation with matter

2.1.1 Interaction of photons with matter

In contrast to charged particle, photons are not detected by either electrical or magnetic fields. Their electrical and magnetic properties are relevant to interaction with matter. They can indirectly ionize the orbital electrons of the target atoms by undergoing various possible interactions. Moreover, they can also directly ionize the atom by interacting with the electrostatic field of the nucleus. The probability for each interaction depends on the energy $h\nu$ of the photon and the atomic number Z of the target. These interactions could be categorized into five types: coherent (Rayleigh) scattering, photoelectric effect, Compton effect, pair production and photonuclear disintegration. Since coherent scattering and photonuclear disintegration occurs mainly in energies range $\leq$10 keV and $\geq$8 MeV respectively, these interactions are out of the energy used in this thesis (i.e. up to 6 MeV). The other three interactions, as described in the following, have fundamental roles in radiotherapy, imaging as well as radiation dosimetry.

2.1.1.1 Photoelectric effect

The photoelectric effect occurs when a photon is absorbed by an atom causing the ejection of an orbital electron. As a condition in this effect, the photon energy is fully absorbed by the atom. The kinetic energy equals the difference between the photon energy and the electron binding energy. The ejected atomic electron creates a vacancy in the shell causing an electron-ion pair and atomic instability. As a consequence, an electron from an outer shell fills the vacancy with energy loss in the form of characteristic X-rays or

Auger electrons. The interaction mechanism is schematically illustrated in (figure 2.1).

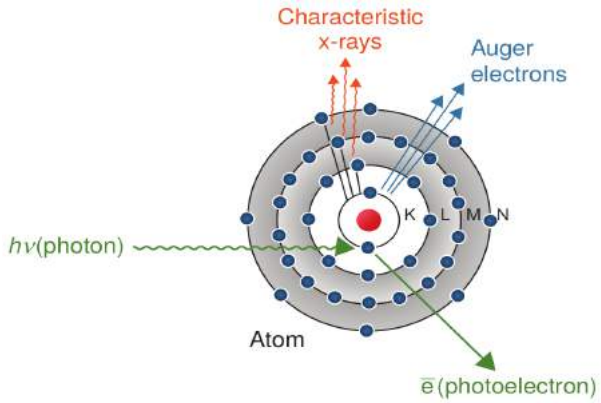

Figure 2.1: Diagram illustrating the photoelectric effect [8].

The interaction probability of the photoelectric effect has a complex dependence on the medium and electron energy, In principle, The energy dependence of the cross section is assumed to be = $1/E^3$ at low photon energies and gradually changes into $1/E$ at high energies. Regarding atomic number dependence, the cross section is assumed to be Z^n where n ranges from 4 to 5 [20]. Figure 2.2 displays the atomic cross section for the photoelectric effect against incident photon energy for various absorbers ranging from Hydrogen to lead. The sharp spikes in all curves (except for H and C) indicate the absorption edges which correspond to the electron binding energies of the K-, L- and M- shells of the absorbing material, showing that an incident photon with energy identical to one of the absorption edge energies will experience a sudden increase in the photo absorption. Accordingly, the maximum probability of a photoelectric effect occurs when low energy photon interacts with a high Z material. In radiotherapy, the importance of the photoelectric effect appears in transmission imaging for X-ray CT. For instance, bone (high Z) absorbs more photons than soft tissue (low Z) resulting in image contrast.

2.1.1.2 Compton effect

In Compton effect, the incident photon collides inelastically with a free or loosely bound electron. A fraction of the photon energy is transferred to electron kinetic energy whereas the rest is preserved in the scattering photon (see figure 2.3). Practically, in Compton effect, the incident photon has a much larger energy than the electron binding energy and can assumably interact with a free electron, since it satisfies the energy and momentum conservation principle. Accordingly, The scattered photon energy E_s as a function of the incident photon energy E_i and the scattering angle θ is calculated by:

$$E_s = \frac{E_i}{1 + \frac{E_i}{m_e c^2}(1 - \cos\theta)} \tag{2.1}$$

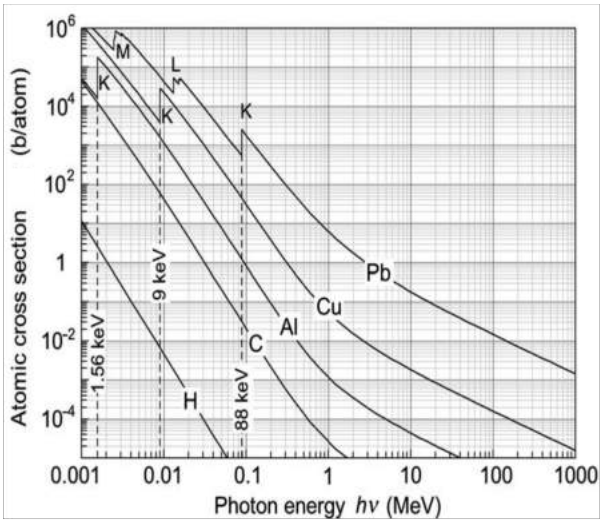

Figure 2.2: Photoelectric atomic cross section against photon energy $h\nu$ for various absorbers. Energies of different absorption edges are also indicated [20].

where m_e is electron rest mass and c is the speed of light. For the recoil electron, the sum of its kinetic energy E_e^k can be obtained depending on the conservation principle and equation (2.1) as follows:

$$E_e^k = E_i - E_s = E_i \left[\frac{\frac{E_i}{m_e c^2}(1 - \cos\theta)}{1 + \frac{E_i}{m_e c^2}(1 - \cos\theta)} \right] \tag{2.2}$$

In the energy region not affected by electron binding effects, the atomic cross section for Compton scattering ${}_a\sigma_c$ is determined from the electronic cross section ${}_e\sigma_c$, which is calculated by integrating the differential electronic cross section per unit solid angle, using the relationship:

$${}_a\sigma_c = Z\,{}_e\sigma_c \tag{2.3}$$

As the ${}_e\sigma_c$ is given for free electrons and consequently independent of Z, the atomic cross section ${}_a\sigma_c$ is linearly dependent on Z. Compton mass attenuation coefficient σ_c/ρ is calculated from the ${}_a\sigma_c$ as follows:

$$\sigma_c/\rho = \frac{N_A}{A}\,{}_a\sigma_c \tag{2.4}$$

where N_A is Avogadro's number and A is the mass number.
By using equation (2.3) in equation (2.3), σ_c/ρ is given by:

Table 2.1: Compton atomic cross sections ${}_a\sigma_c$ and mass attenuation coefficients σ_c/ρ at photon energy $h\nu$ of 1 MeV for various absorbers [20].

Element	Symbol	Z	A	${}_a\sigma_c$ (b/atom)	σ/ρ (cm2/g)
Hydrogen	H	1	1.01	0.21	0.1261
Carbon	C	6	12.01	1.27	0.0636
Aluminum	Al	13	26.98	2.75	0.0613
Copper	Cu	29	63.54	6.12	0.0580
Lead	Pb	82	207.20	17.32	0.0500

$$\sigma_c/\rho = \frac{ZN_A}{A}\,{}_e\sigma_c \tag{2.5}$$

Since Z/A = 0.5 for low Z elements (except hydrogen) while increasing Z gradually decreases Z/A to $\approx$ 0.4 for very high Z elements, the mass attenuation coefficient is roughly independent of Z and proportional to the electron density (see table 2.1). For instance, the Compton attenuation for constant energy per g/cm^2 for bone is nearly the same as that for soft tissue. Yet, 1 cm of bone would attenuate equivalent to 1.53 cm of the soft tissue. This low difference in σ_c/ρ is a disadvantage in transmission imaging but an advantage in therapy as the contribution to dose delivery of Compton scattering at the same energy results uniform within different tissues.

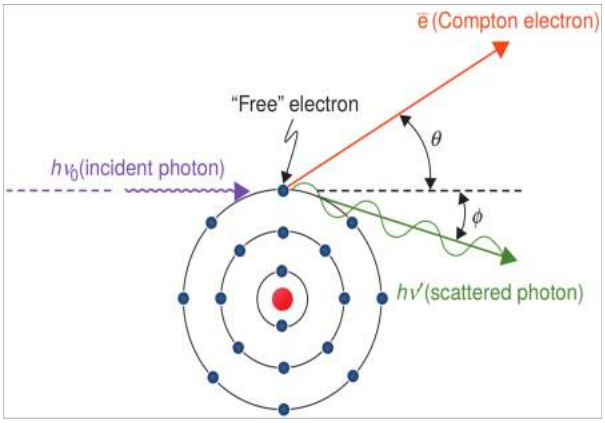

Figure 2.3: Illustration of Compton scattering [8].

2.1.1.3 Pair production

When a photon with energy above 1.022 MeV interacts with the electromagnetic field around the nucleus, its energy may be converted into electron and positron. Interestingly, this photon to mass conversion process is an example of the famous Einstein's theory $E = mc^2$. The photon energy exceeding the 1.022 MeV threshold is shared between the particles as kinetic energy. The positron subsequently annihilates by combining with one

electron of the medium close to its generation point, producing two annihilation photons each with E = 0.511 MeV (fig 2.4). The annihilation is a reverse process of converting mass to energy. The probability of pair production increases proportionally with Z^2 and increases as the logarithm of the incident photon energy above the threshold energy with dominance over Compton interactions at energies above 10 MeV. Hence, the impact of this interaction is minimal in therapy where the typical maximum energy is 6 MeV. In addition to pair production, a much less probable interaction could occur when the incident photon has energy equal or higher than 2.044 MeV. In a process referred to as electronic pair production or triplet production, the incident photon interacts with an orbital electron of the absorber resulting in the photon to disappear and three light charged particles are released: the original orbital electron and the electron-positron pair produced in the interaction.

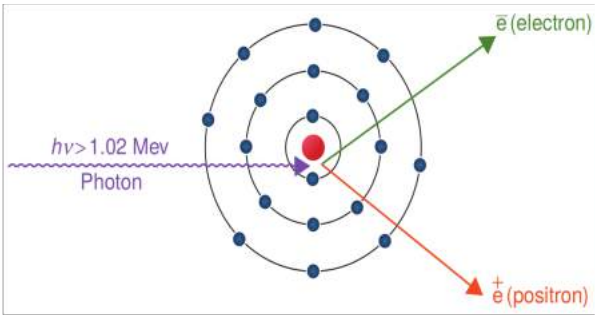

Figure 2.4: Diagram illustrating the pair production in the nuclear Coulomb field [8].

2.1.1.4 Attenuation

Overall, photon attenuation when passing through matter is an exponential process as a function of path length. Attenuation occurs either by absorption (e.g. photoelectric effect) or scattering (e.g. Compton scattering). The attenuation is defined as the probability of occurrence that the photon is removed from the beam per unit path length. The number of transmitted photons I is described by Beer-Lambert's law as follows:

$$I(x) = I_0 e^{-\mu x} \tag{2.6}$$

Where I_0 is the initial intensity (i.e. number of photons before attenuation), and x is the path length of the absorbing material. μ is the linear attenuation coefficient in cm^{-1}.

2.1.2 Interactions of charged particle radiation with matter

Charged particles are surrounded by the Coulomb electric field. When traversing an absorber, the particle may interact with the Coulomb electric field of the orbital electrons or the atom nucleus resulting in elastic or inelastic scattering. The charged particle may

transfer some of its kinetic energy to the medium (collision loss) or to photons (radiation loss). However, the interaction type is depending on the mass of the charged particle and the trajectory with respect to the absorber atom. The charged particles of interest in clinical application can be either light (electrons and positrons) or heavy particles (protons and helium, carbon and oxygen ions). General aspects of their interactions with the medium are listed below.

2.1.2.1 Light charged particles

Light charged particles have a considerably smaller mass compared to the mass of atoms. As for electrons with high energy, they experience radiative losses within Coulomb field of nucleus and to less extent electrons. Low energetic electrons mainly experience ionization/excitation with other electrons besides some Coulomb scattering. In the radiative losses, the electron may undergo a significant loss of its energy accompanied by an emission of X-ray photons. This type of interaction is called bremsstrahlung and has the major significance in X-ray generation in X-ray tubes and linacs, as discussed in section 2.3. Furthermore, the electrons may collide with an orbital electron causing electron ejection (atom ionization) or electron shell elevation (atom excitation). Overall, the electrons experience multiple scattering when traversing through a media. The radiative yield, defined as the average fraction of its energy that a beta particle radiates as bremsstrahlung in slowing down completely, increases directly with the absorber atomic number Z and the kinetic energy of electrons. In X-ray targets for imaging applications (energy around 100 keV), the radiation yield is of the order of 1%, whereas for radiation therapy (energy in the range of 6-25 MeV) the radiation yield amounts to 10–20%.

As for positrons, they travel a small distance through the media and interact with surrounded electrons through positron-electron annihilation mostly producing two 511 keV photons.

2.1.2.2 Heavy charged particles

As ions have a mass considerably larger than electrons, they can be categorized as heavy particles. Examples include protons, helium, carbon and oxygen ions. These particles may undergo elastic and inelastic interactions with electron or nuclei similar to light particles but different in magnitude. As for heavy particles, they mostly interact inelastically with electrons and do not change direction considerably when passing through a medium due to their large masses. The heavy particles lose energy and slow down by ionizing or exciting the orbital electrons. The slow traveling heavy particle has more probability of inelastic interaction with Coulomb field of the nucleus. The rate of energy deposition per unit path length is proportional to the square of the particle charge and inversely proportional to the square of its velocity, according to the well known Bethe-Bloch formula [20]. That is the physical foundation of the Bragg peak, as maximal energy deposition close to the range of the ion beam, and its use in particle external radiation therapy.

2.2 Radiation detector properties

The primary function of radiation detection systems is to measure, either directly or indirectly, the radiation quantity. Their basic principle is relying on the interaction of radiation with the detector material. For detectors relying on ionization measurements, radiation quantity is defined by the number of the charge carriers, either electron-ion pairs or electron-hole pairs, created by the ionization process in the active region of the detector volume. The average energy required to generate one electron-ion or electron-hole pair is approximately constant (W) with energy of the radiation and varies in dependence on the detector type. For instance, W value ranges from 1 to 5 eV for semiconductor detectors and $\sim$30 eV for gas detectors [21]. Consequently, the total number of the created electron-ion or electron-hole pairs is proportional to the deposited radiation energy. Accordingly, the signal measured by the detector may be converted to absorbed dose with special calibration and correction factors. As a radiation dosimeter, the detector must be provided with adequate accuracy and precision, linearity with respect to the dosimetric quantity, dose rate independence and the desired spatial resolution. Unfortunately, there is no single dosimeter that can satisfy all these characteristics. Therefore, the choice of the used dosimeter is highly dependent on the measurement purpose and requirements. In this section, an overview of the different types of dosimeters used in conventional radiation therapy is presented with particular focus on its advantages and disadvantages.

2.2.1 Ionization Chambers

The gold standard in accuracy and precision for radiotherapy dosimetry is the air filled ionization chamber (IC). An ionization chamber is a gas-filled cavity having two parallel collecting electrodes or one central electrode surrounded by a conductive outer wall. The wall has different density but the same effective atomic number of the air to ensure similar radiation interaction mechanisms to tissue. Although in principle the charge measured by an air filled ionization chamber should be directly proportional to the adsorbed dose in water the linearity is actually very sensitive to changes in temperature, pressure, humidity and the applied voltage. As suggested by the IAEA in their code of practice and American Association of Physicists in Medicine (AAPM) [22] [23], a few corrections must be considered. For example, calibrations are applied according to the following equation:

$$D_w^Q = M k_Q N_{D,w}^{60_{Co}} \tag{2.7}$$

where D_w^Q is the absorbed dose in water for a certain "beam quality" Q, k_Q is a conversion factor specific for the chamber and the beam quality and $N_{D,w}^{60_{Co}}$ is the absorbed dose to water calibration factor for the reference beam quality of ^{60}Co while M is the corrected charge measured by the ionization chamber through an electrometer and given by:

$$M = P_{ion} P_{TP} P_{pol} P_{elec} M_{raw} \tag{2.8}$$

where P_{ion} corrects incomplete ion collection efficiency, P_{TP} is the temperature–pressure correction which corrects the reading to the standard environmental conditions for which the ion chamber's calibration factor applies, P_{pol} corrects for any polarity effects, P_{elec} takes into account the electrometer's calibration factor if the electrometer and ion chamber are calibrated separately and M_{raw} is the raw ion chamber reading in Coulombs C.

Ionization chambers come in various shapes and sizes; the most widely used design is the cylindrical "thimble" chamber due to its stability, accuracy and relative ease of use in clinical environment. Figure (2.5), schematically illustrates the design of a typical cylindrical chamber (i.e. Farmer chamber). However, when measurements of strong radiation field gradients are required, Farmer chambers do not represent the elective choice due to large effective volume (of about 0.60 cm^3) and low spatial resolution. Thus, different chamber models with smaller sizes are used in this case.
Different from cylindrical chambers, the parallel plate ionization chamber has a flat plane (toward the radiation source) making the point of measurement at the front surface of the cavity. The parallel plate ionization chambers also have a fundamental role in radiotherapy as they represent the monitoring systems of the linear accelerators (see section 2.3).

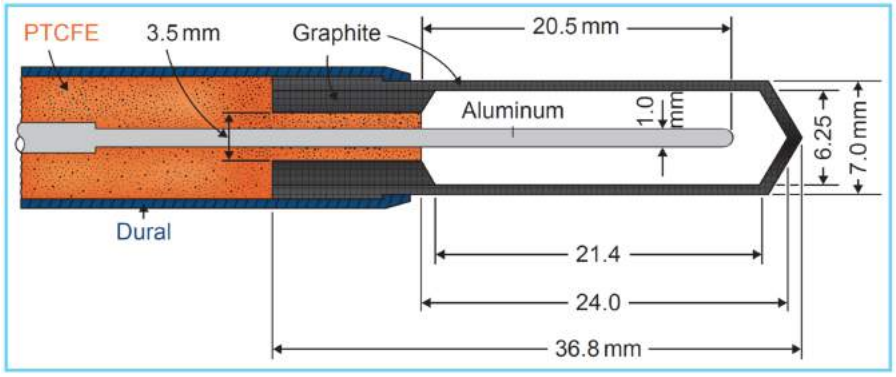

Figure 2.5: Basic design of a cylindrical Farmer graphite/aluminum chamber. Nominal air volume, 0.6 mL [8].

2.2.2 Diode Detectors

Diode detectors consist of semiconductor silicon crystal doped with different impurities on the two sides. The N-type side is the electron rich region while the P-type side is the hole rich region. Applying voltage upon these two sides creates a depletion region which may act as the air cavity of ionization chambers. The ionizing radiation generates electrons (free charge carriers) and holes when passing through the depletion region. The electrons move towards the P-type region and create an electric current that can be measured with high precision. The average ionization energy needed to form an electron-hole pair in silicon is around 3 eV whereas the ionization energy for ICs is about 30 eV. This feature in combination with the crystal density, about 1800 times denser than air, leads to

a relative efficiency per unit of volume four orders of magnitude larger than ICs. Thanks to the relatively small size of these detectors, the construction of high spatial resolution dosimeter is enabled. However, these detectors exhibit angular dependence. Thus, the detector orientation during measurements has to match the calibration orientation. Furthermore, the diodes are made of a non-tissue equivalent material and due to that, these detectors are highly energy dependent. These drawbacks make the diodes suitable for high resolution relative dosimetry, but not for absolute dosimetry. The calibration should be as a function of the beam energy with specific correction factors for field size, physical attenuators, projection angle, source to surface distance and temperature. The diodes are commercially available in forms of single diodes, 2D array, and 3D array (see 2.6). Diodes are used for routine QA programs and even dose measurement during treatment (in vivo dosimetry).

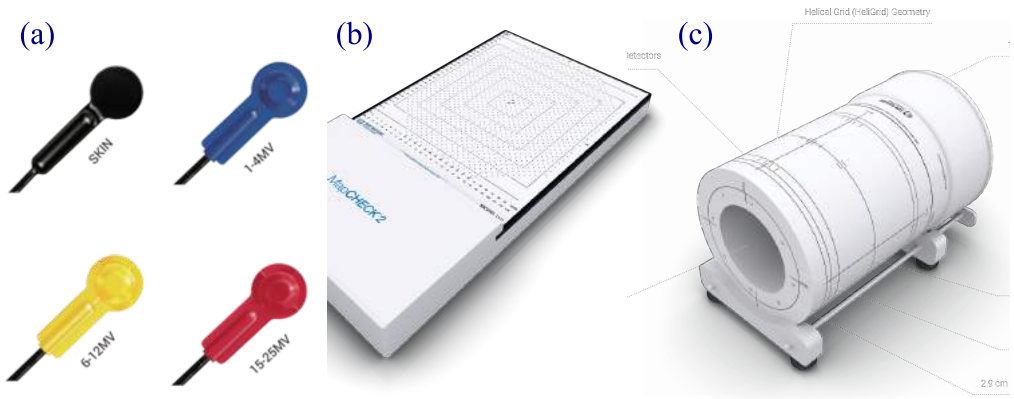

Figure 2.6: Sun Nuclear® diodes in different forms: (a) single, (b) 2D array and (c) 3D array.

2.2.3 Diamond Detectors

The diamond detectors are classified as semiconductor detectors made of diamonds synthetically produced in laboratory through the process of Chemical Vapor Deposition (CVD). Due to a relatively large ionization energy of 5.54 eV compared to semiconductor silicon crystal, the free charge carriers are less and hence, diamond detectors offer higher resistivity and correspondingly lower leakage currents with respect to diode detectors. Furthermore, the incident radiation interacts with the active region of the detector creating electron-hole pairs without being depleted. A current is generated and measured using an electrical field across the detector contacts. The signal is then linearly amplified, thus making it proportional to the induced charge. Commercially, these detectors are manufactured with a very small sensitive volume in the order of a few mm^3 with high sensitivity, resistance to radiation damage and encapsulated in a waterproof isolator (see 2.7).
Diamond detectors are tissue equivalent, have no energy dependence, have small sensitive volume (and thus, high spatial resolution) and have no strong angular dependency. This gives the diamond detectors the merits to be used in radiotherapy clinics as an abso-

lute dosimeter for regular measurements and exclusively for high dose gradient and small fields. However, diamond detectors have a relatively high cost due to the scarcity of high quality material making their use in common practice limited [24].

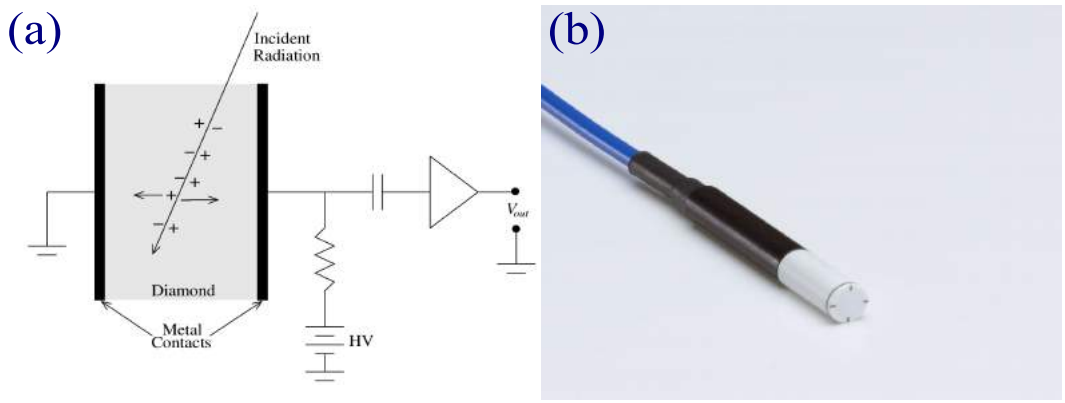

Figure 2.7: (a) Sketch of a diamond based detector [25]. (b) PTW® micro-diamond detector.

2.2.4 Films

Films could serve in diagnostic radiology, radiation therapy, and radiation protection. For films dosimetry, radiographic or radiochromic films can be used. The former type once was the cornerstone of detection systems in transmission imaging and was used also in relative dosimetry. However, nowadays, it is replaced by digital detectors for imaging purposes and radiochromic films for dosi3metry. Radiochromic films are colorless films with tissue equivalent composition. The commonly used type is the GafChromic film with active layer of a thickness = 30 μm [26] (figure 2.8). When ionizing radiation interacts with the active layer, the dye of the film polymerizes and develops a different color. A laser scanner is used to produce a (Red, Green, Blue) colored image out of the irradiated film. The degree of coloring in the each channel is expressed in optical density (OD) and defined as:

$$netOD = OD_{irradiated} - OD_{unirradiated} = -log_{10} PVR_{irradiated}/PVR_{unirradiated} \quad (2.9)$$

where (PVR) is the raw pixel value typically from the correspondent color channel. The relationship between the (OD) and the dose (D) is expressed by:

$$D = A_0 \times netOD + A_1 \times netOD^{A_2} \quad (2.10)$$

where A_i $(i = 0...2)$ are the fitting parameters. The calibrated radiochromic films perform relative or absolute dosimetry with sub-millimeter spatial resolution and accuracy

in dose determination $\pm 3\%$ with even better results when using a more complex triple channel [26]. Although the self-developing radiochromic films are easier to use than the radiographic films (e.g. no need for dark room, film cassettes or film chemical processing), radiochromic films are still categorized as passive dosimeters and could not provide a real-time measurement. However, these films are used in radiotherapy clinics in IMRT/VMAT pre-treatment QA programs due to their superior spatial resolution over other dosimeters.

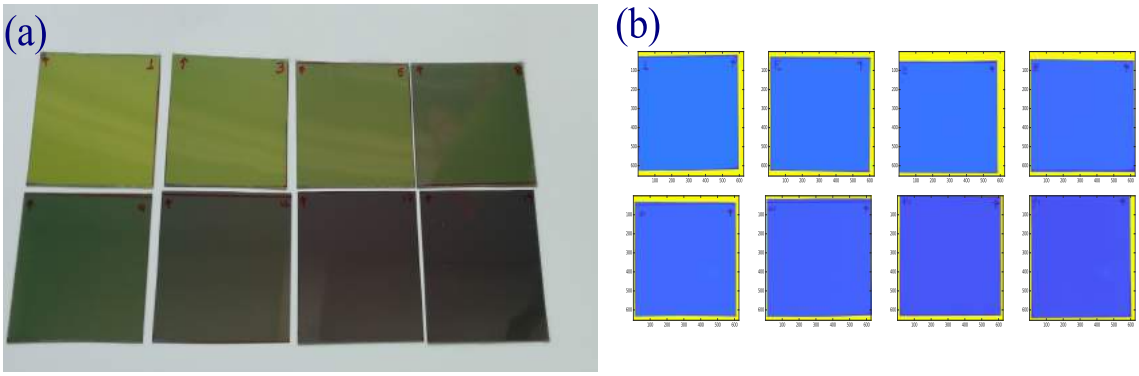

Figure 2.8: (a) Picture of cutted GafChromic films irradiated with different doses. (b) Scanned images of correspondent films. The images represent the pixel values in the red channel.

2.2.5 Thermoluminescent detectors

Thermoluminescent detectors (TLD) used in medical applications is almost composite of tissue equivalent crystalline materials (e.g. lithium fluoride doped with magnesium and titanium, LiF: Mg, Ti). When ionizing radiation interacts with the crystal lattice, orbital electrons are excited to a higher state, but instead of subsequently relaxing to the ground state, they remain trapped in the so-called "electron trap" made by the lattice impurities (usually magnesium or titanium). The electron cannot escape the trap at room temperature and therefore, the charge is stored till the entrapment process of heating the crystal is applied. The electrons lose the excitation energy as visible light, which is converted to electrical current by a photomultiplier and subsequently measured. The measured signal is then calibrated to dose. TLD is meant for measuring a cumulative dose. However, the crystal reaches the saturation once all traps are occupied by electrons. Though, the heating process clears electrons traps and the TLD is then annealed and may be reused for dosimetry.
TLDs are commercially available in various forms (e.g. powder, chips, rods and ribbons). Due to their small sizes and no need of connecting wires, they are used in radiotherapy either in routine QA procedure, in-vivo dosimetry or implanted in phantoms. TLDs are also used as personal dosimeters for radiation workers.

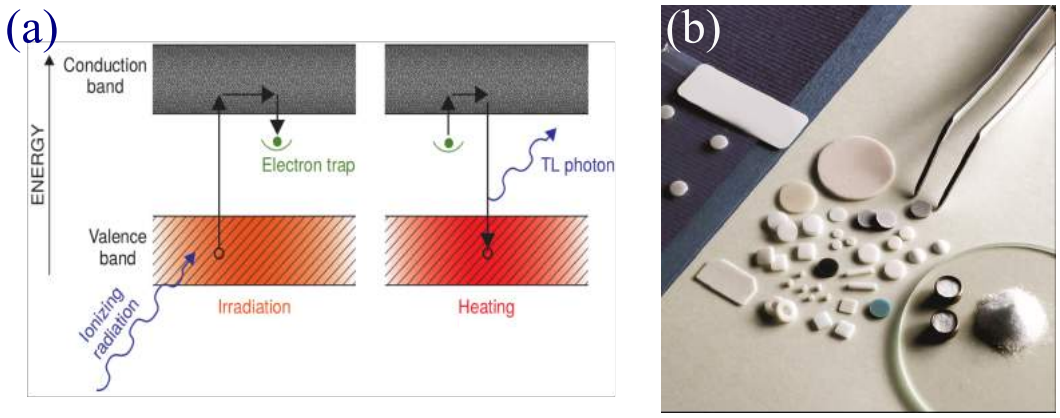

Figure 2.9: (a) A simplified energy-level diagram illustrating the thermoluminescence process [8]. (b) Different shapes of TLDs.

2.2.6 Polymer Gels

Polymer gels are composed of radiosensitive chemicals dissolved in gelatin. In brief, when irradiated, the chemicals polymerize forming free radicals that can be quantified by measuring the changes of nuclear magnetic resonance spin-relaxation time using an MRI scanner, or estimating the density changes using typically optical or X-ray CT or ultrasound. Polymer gels can be molded to any desired shape or form, and since the gel is approximately tissue equivalent, they can be used as phantoms (figure 2.10). Consequently, gel dosimetry is the only 3D dosimetry system, providing a 3D dose distribution with high spatial resolution.

Polymer gel dosimetry proved its usefulness for dose verification in IMRT/VMAT [27]. However, similar to film dosimetry, polymer gels are designed for single measurements, and as passive dosimetry systems, they require long processing time and sophisticated readout systems.

2.3 Clinical linac

Linac is a device that accelerates charged particles (electrons) using high-frequency electromagnetic waves in a linear tube. The medical linac accelerates electrons to a nominal energy that ranges from 6 to 25 MeV. Accelerated electrons can be used to treat superficial tumors or to strike a target to produce X-rays for treating deep seated tumors. The modern linac components are illustrated in figure 2.11. The working principle of the system is described in the following. First, the electrons are generated in the electron gun by thermoionic emissions from a hot tungsten filament (cathode) and guided by the anode towards the waveguide tube. In the waveguide tube, high pulse microwaves produced by a magnetron or a klystron accelerate the electrons to velocity comparable to the speed of light. The strong magnetic field inside the tube focuses the electrons in a pencil beam

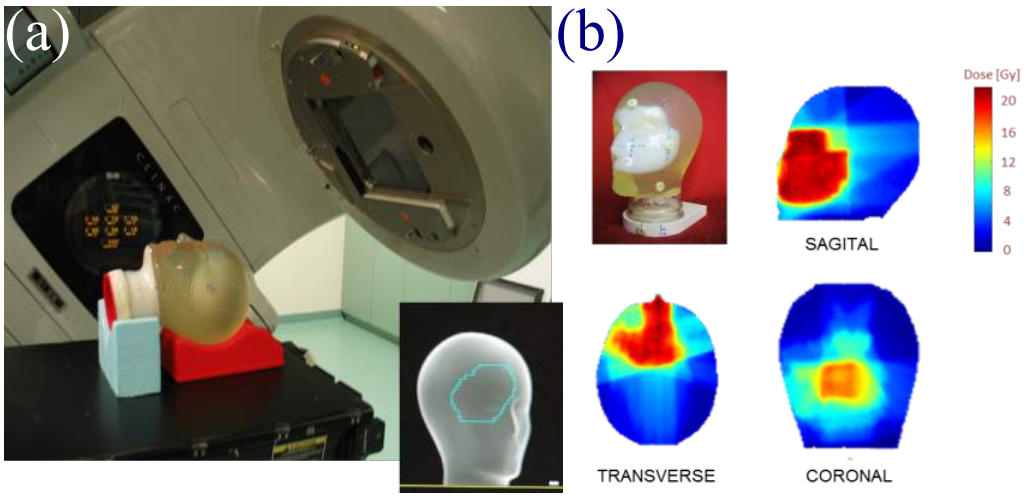

Figure 2.10: (a) Polymer gel dosimeter irradiated according to 3D-CRT techniques. (b) The upper left picture illustrates the irradiation effect (white region) on the dosimeter. The rest; different views of the dose distribution obtained by use of MRI scanner [18].

with a diameter of about 2 mm. The pencil beam is bent across the bending magnet to perpendicularly strike a high Z target. Bremsstrahlung X-rays are produced by the interaction between the electron beam and the target with a spectrum of energies from 0 up to the nominal (maximal) energy of the incident electrons. Due to the high energy of the electrons, the X-ray beam produced in the target is mainly peaked forward in the beam direction. The process of shaping the photon beam starts in a component of the linac called head. Although the compositions and elements of the linac head are specific to manufacturer, the general scheme mainly consists of a flatting filter, monitoring chambers and three collimators (i.e. primary, secondary and the multi-leaf collimator (MLC)). The generated photons are collimated by the primary collimator and their intensity is made fairly uniform by the flattening filter. The beam is controlled and monitored by a monitor chamber (parallel plate ionization chamber) located immediately after the flattening filter. The secondary collimator placed after the flattening filter is movable and used to define the rectangular field shape with two upper and two lower independent jaws. In modern linacs this function is embedded in the MLC and the four jaws are replaced by two guardian jaws (diaphragm) placed downstream the MLC. The MLC is an array of high Z leaves that can be individually controlled to create regular and irregular beam shapes. Modern linacs incorporate up to 160 leaves with 5 mm width creating fields up to 40 $\times$ 40 cm^2 (figure 2.12). Dose delivery techniques based on MLC (e.g. VMAT) set technological challenges requiring high precision of leaf positions with high-speed movement of the MLC. In addition, to modulate the intensity of the beam, the MLC and the rigidly attached diaphragm can rotate around a vertical axis and the linac head is mounted on a gantry that can rotate around the patient in the longitudinal axis. Additionally, leakage of radiation through the MLCs (known as intraleaf and interleaf transmission) adds extra dose to the patient. In order to minimize this effect, leaves are designed to have stair-step leaf-sides, and adjacent leaves interlock in a 'tongue-and-groove' arrangement. Even more, the leaves edges in the beam direction contribute to the dose distribution and

field penumbra. The leaf thickness along the beam direction ranges from 6 cm to 9 cm, depending on the type of accelerator [7].

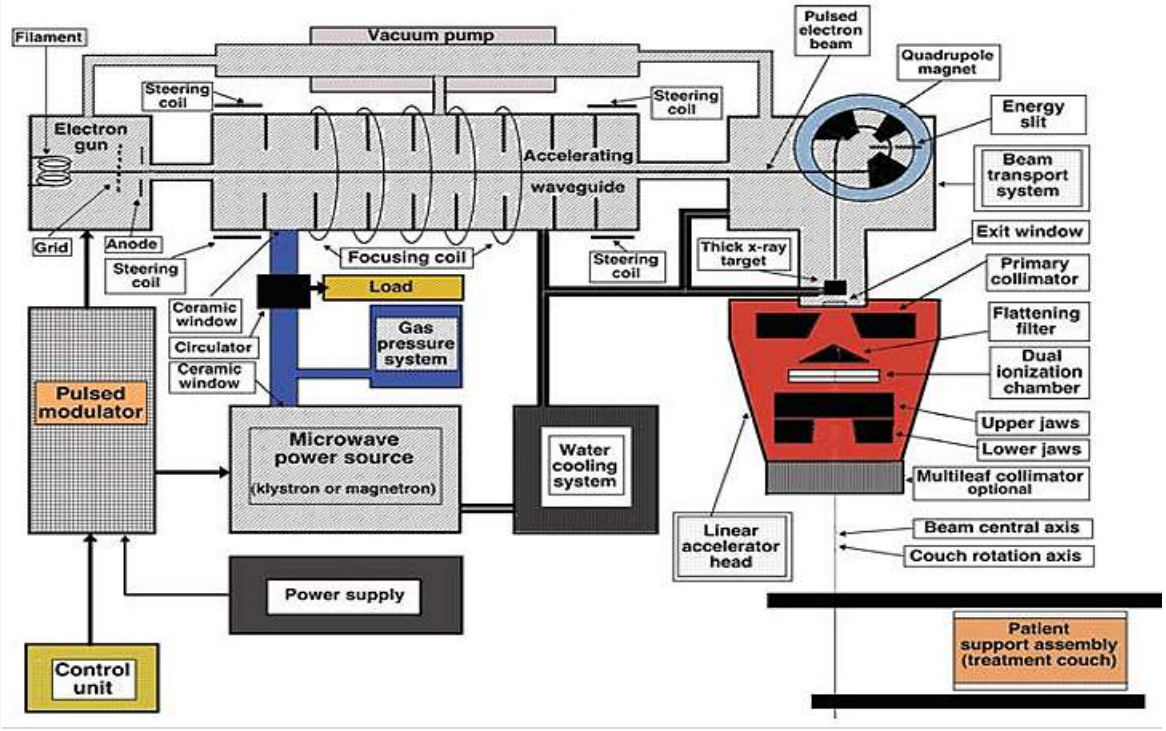

Figure 2.11: Schematic diagram of a medical linear accelerator [20].

2.4 Quantification and Measurement of Dose

Quantification of radiation deposition in the human body is essential for any medical use of radiation. All radiation dosimetry systems are designed to represent the energy deposition to the human body either by directly or indirectly ionizing radiations. In the medical field, dosimeters are used for diagnosis, treatment or protection of patients, workers, and the public. The goal in transmission imaging is to obtain the maximal image quality with the lowest radiation dose. In radiotherapy instead, the best compromise between the therapeutic dose to the tumor and the unwanted dose to normal tissue is searched. In radiation protection, the radiation exposure is minimized according to the principle of As Low As Reasonably Achievable (ALARA) for all the involved people. Depending on the specific applications, several quantities and units have been introduced to describe dosimetric quantities. The dosimetric quantities of interest for the thesis work are described.

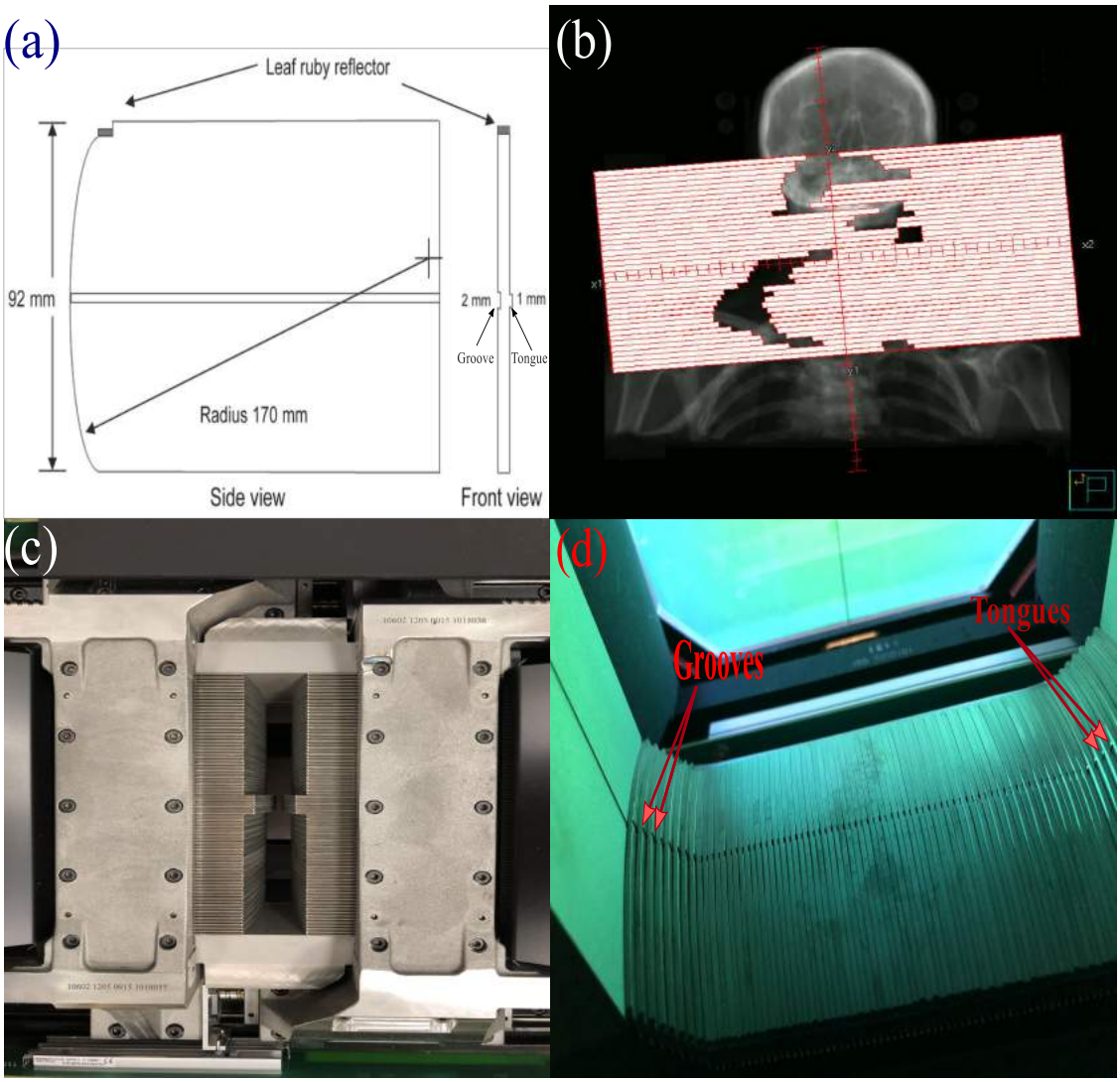

Figure 2.12: (a) A schematic side and front views of a single leaf of Agility® MLC [28]. (b) Beam's eye view of a field modulated using MLC [29]. (c) and (d) Different pictures of an Agility® MLC illustrating 160-leaf arrangement.

2.4.1 Photon fluence and energy fluence

The particle fluence (Φ) is defined as the number of particles (dN) incident on a sphere of cross-sectional area (dA):

$$\Phi = \frac{dN}{dA} \tag{2.11}$$

The International System of Units (SI) unit of particle fluence is m^{-2}. The energy fluence (Ψ) is defined as the radiant energy (dE) incident on a sphere of cross-sectional area (dA):

$$\Psi = \frac{dE}{dA} \tag{2.12}$$

The SI unit of energy fluence is J/m^2. The relation between energy fluence and photon fluence for a monoenergetic beam is given by:

$$\Psi = \frac{dN}{dA}E = \Phi E \tag{2.13}$$

2.4.2 Exposure

The exposure (X) is the absolute value of the total charge of the ions (dQ) of one sign produced in air when all the electrons and positrons liberated by photons in air of mass (dm) are completely stopped in air.

$$X = \frac{dQ}{dm} \tag{2.14}$$

The unit of the exposure is typically roentgen (R) which is equivalent to a charge of 2.58×10^{-4} C produced per kilogram of air in SI unit.

2.4.3 Kerma

The Kerma (K) is an acronym for kinetic energy released in the medium and it is defined as the as the expectation value of the energy transferred (dE_{tr}) form the indirectly ionizing radiation (photons or neutrons) to charged particles per unit of mass of the absorber (dm):

$$K = \frac{dE_{tr}}{dm} \tag{2.15}$$

The SI unit of Kerma is (Gy) which equals 1 Joule of energy transferred per kilogram of a medium.
In reference to energy transfer method, Kerma can be divided into two components: the collision kerma K_{col} and the radiative kerma K_{rad}. K_{col} refers to the energy transfer resulted from Coulomb force interactions with atomic electrons. Thus, K_{col} leads to the

production of electrons that dissipate their energy as ionization in or near the electron tracks in the medium. K_{rad} refers to the energy transfer resulted from radiative interactions (bremsstrahlung and less-likely electron-positron annihilation). Thus, K_{rad} leads to the production of radiative photons that transfer a fraction of the energy out of the medium.

2.4.4 Dose

The Dose (D) is defined as the expectation value of the absorbed energy ($d\varepsilon$) per unit of mass of a medium (dm). Unlike Kerma, dose applies to the expectation value of both indirectly and directly ionizing radiations:

$$D = \frac{d\varepsilon}{dm} \tag{2.16}$$

Similar to Kerma, the SI unit of the absorbed dose is (Gy).

2.4.5 Charged Particle Equilibrium

The energy transfer from the photon beam to the charged particles (Kerma) at a particular location does not lead in principle to a dose deposition at the same location. The secondary electrons move away according to their range in any direction and can escape the location of interest. Thus, given a certain photon fluence, the Kerma is easily estimated but not the dose. In a homogeneous medium, Kerma is maximal at the entrance of the medium, while the absorbed dose initially builds up as a function of depth until a maximum dose is reached (Z_{max}) (figure 2.13). Where the two curves meet, the charged particle equilibrium (CPE) is reached. Then, at depths greater than the maximum depth (Z_{max}), there is a transient charged particle equilibrium (TCPE) in which both D and K_{col} decreases at the same rate. Thus, the absorbed dose D to a medium can be calculated from the energy fluence (Ψ) following the following equation:

$$D = \beta\Psi(\mu_{en}/\rho) \tag{2.17}$$

where (μ_{en}/ρ) is the mean mass energy absorption coefficient and β is the quotient of D at a given point and K_{col} at the same point. β is < 1 at the build-up region, = 1 at the CPE point and > 1 at the TCPE region.

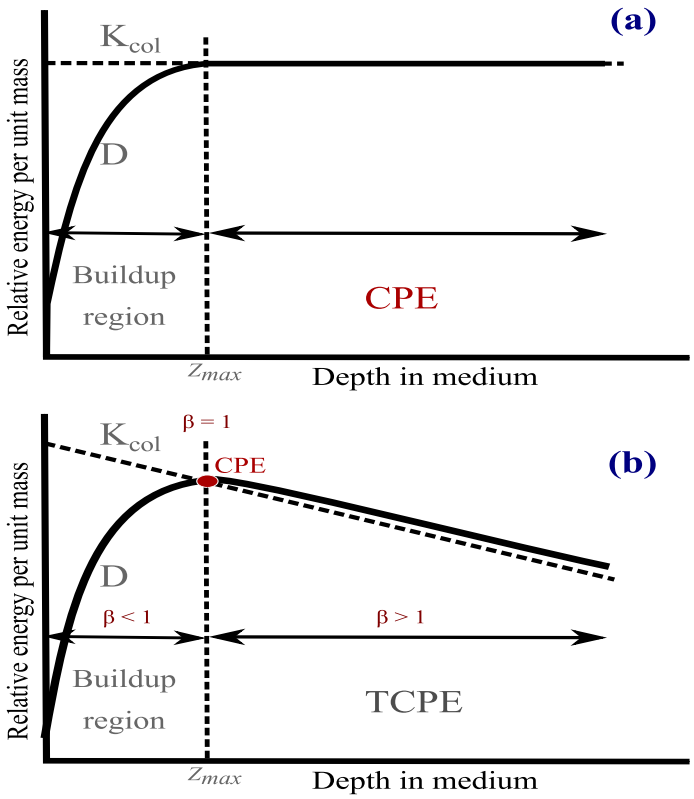

Figure 2.13: Kerma K_{col} and absorbed dose D as a function of depth in a homogeneous medium irradiated by high energy photon beam for (a) the hypothetical case of no photon attenuation and for (b) realistic case adapted from [15].

2.5 Dosimetry of Photon Beams

2.5.1 Characteristics of Photon Beams

In radiation therapy, photon beams generated by the linac are polyenergetic and have a wide distribution in energy that spans from 0 eV to the nominal energy of the accelerated electrons. The shape of the spectra depends on the shape of the electron beam energy, the target (photon source) thickness, the fixed collimators (used for shielding), flattening filter and movable collimators (jaws, MLC, diaphragm ...). Particularly, the movable collimators (i.e. jaws, MLC and diaphragm) are those determining the field shape that changes the energy distribution of the machine specific reference field to variable standard fields. Different spectra for different energies generated by Monte Carlo simulation [30] are illustrated in 2.14

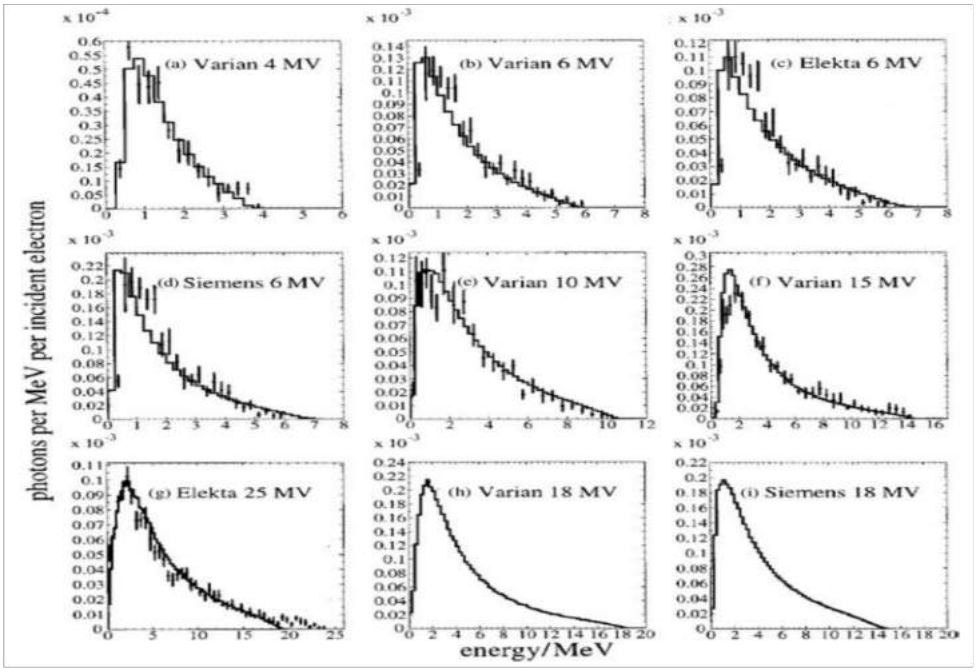

Figure 2.14: Comparison of MC calculated spectra for different commercial linacs [30].

The energy distribution is the most exhaustive description of the photon beam quality but difficult to measure. Typically, the beam quality is indirectly assessed by measuring the percentage dose as a function of depth and lateral dose profile in a water phantom. This assessment is incomplete, but sufficient for operation of treatment routine. However, recently, some clinics uses a comprehensive characterization of beam quality in order to improve the dose calculation accuracy.

2.5.2 Dosimetric measurements used to characterize the photon beam

The attenuation of a photon beam traversing air is negligible and the intensity due to divergence can be determined using the inverse square law. When traversing media with varying density, on the other hand, the photon beam undergoes attenuations which are more complicated to calculate. Therefore, various dosimetric quantities and methodologies have been introduced to facilitate dose calculation in radiation therapy situations. The dosimetric measurement is usually performed in a water phantom due to its similar absorption and scattering properties of muscle and other soft tissues. For practical reasons, the dosimeters and also preferred to be made of water or tissue equivalent material in terms of response to Compton effect (the most predominant interactions in photon therapy energy range). Hence, the given material must have the same electron density as that of water. With reference to the dosimetry of photon beams in water, additional dosimetric quantities of interest to the thesis objectives are described below.

Depth dose distribution
As the photon beam propagates through a water medium, the dose deposition varies per depth in dependence of the beam energy, depth, and distance from the source. Therefore, measurements of the central axis dose distribution for different field sizes provide a good beam characterization method. Percent Depth Dose (PDD) is a quantity used for beam characterization and obtained by measuring the absorbed dose at any depth Z divided by the absorbed dose at a reference depth Z_{max} along the central axis of the beam, thus:

$$PDD = \frac{Z}{Z_{max}} \times 100\% \tag{2.18}$$

In practice, PDD is measured for different nominal energies and different rectangular field sizes during linac commissioning. The commissioning data are then used as a benchmark for future QA measurements.

Linac output
The linac output is defined as the variation of the absorbed dose at Z_{max} as a function of the field size in water. Multiple factors were shown to affect the output factor. Namely, the Scattered photon from the linac head structure, backscattered photons, and electrons into the monitor chamber and, at very small filed sizes, the effect of X-ray source obscured by the collimator [31]. Accordingly, the output is considerably differed from one type of linac to another. As a necessary procedure in linac commissioning and periodic QA, the output factor of each representative field size is measured for each available energy. The measured output is referred to a selected standard field size (commonly the 10×10 cm^2 field) at the distance from the source to the axis of gantry rotation known as the iso-center.

Field size and shape play a significant role in determining the PDD curve. In general, as the field size increases, the contribution of scattered photons to the absorbed dose increments (figure 2.15). On the other hand, the variation of energy distribution inside

a medium influences the responses of detectors especially the highly energy-dependent ones. Hence, accurate estimation of the output is required in order to accurately correct for energy over or under response of detectors for different squared field sizes.

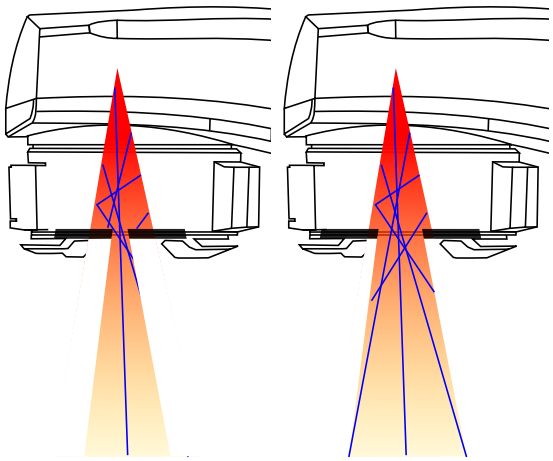

Figure 2.15: Scatter radiation increases with field size.

However, in clinical practice, the majority of the treatments fields are irregularly shaped (not squared). in such scenarios, accurate determination of the output factor is challenging. Thus, a rule-of-thumb method of equivalent squared fields to different field dimensions and shapes has been developed and proved to be useful for quick calculation of the equivalent field parameters [32].

Beam lateral profiles and off-Axis ratio (OAR)
The off-axis-ratio (OAR) between the dose at an off-axis point, either in the cross-line (x direction) and in-line (y direction) directions, and the dose on the central beam axis for any given depth provides a 2D information on the dose distribution inside the phantom. This measurement is performed in QA programs to assess the beam flatness and the beam symmetry, which are relevant also for dose calculations. Beam lateral profiles consist of three regions: central, penumbra and umbra. The central region represents the portion of the beam including doses over 80% of the maximum dose. The penumbra represents the fall-off area at the beam edges. Specifically, the penumbra region is the part of the dose that lies within 20-80% (or sometimes 10-90%) of the maximum dose. The size of the penumbra is geometrically determined by the focal spot of the photon beam (source shape and size) (figure 2.16a), the field size, the MLC shape (figure 2.16b) and the lateral electronic disequilibrium due to Compton scattering. The umbra is where the doses are below the 20% (10%) of the maximum dose. These low doses result from radiation transmitted through collimators and scattered radiation from the linac head shielding.

2.5.3 Dosimetry of photon beams in a patient

Unfortunately, dose calculation in water does not apply to the patient since the patient tissues are not perfectly water equivalent and the patient surface is not entirely flat. The

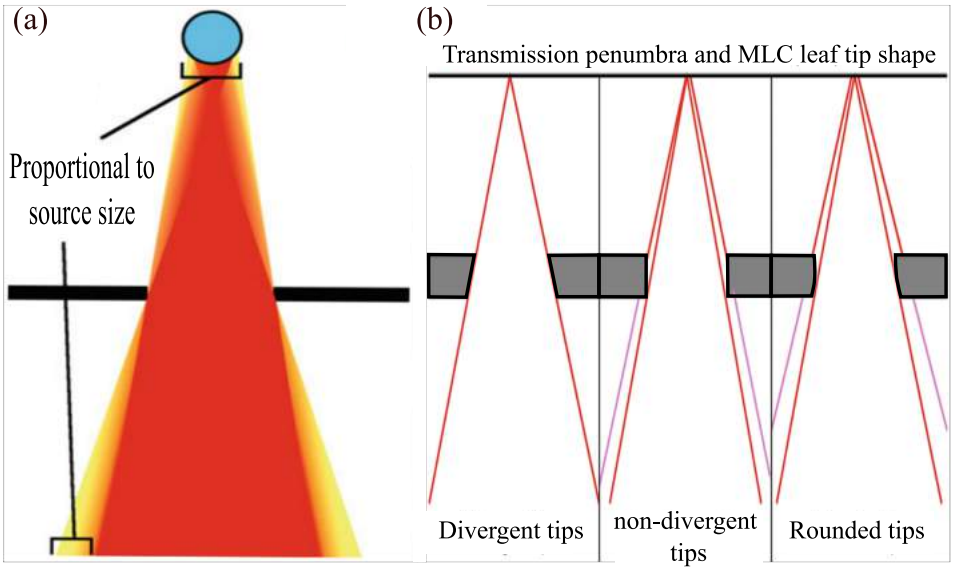

Figure 2.16: (a) The penumbra appears as blurring of the field edge (yellow) and it is directly proportional to the physical size of the source. (b) The penumbra depends also on the MLC tip shape [33].

beam traverses inhomogeneities so that high density tissues (e.g. bone) increase the attenuation whereas low density tissues (e.g. lung) decrease the attenuation. To account for this, complex models are needed thus making dose calculation in inhomogeneous media a complicated task. Therefore, water dosimetry is adequate to characterize the radiation beam but not sufficient to calculate the deposited dose into a patient.

2.6 Treatment planning systems and dose calculation

Current radiation therapy techniques require sophisticated systems to encompass and control the entire clinical work-flow of the treatment. The Treatment Planning System (TPS) represents the heart of that systems and the first key to ensure an accurate dose delivery. In principle, the TPS is responsible for importing the patient CT and PET or MRI images. The tumor and organs at risk delineation and contouring occur within the TPS. According to the tumor location, size and organ at risk constraints, the oncologists along with the physicists (dosimetrists in a few clinics) define the setting parameters relevant to the chosen radiation therapy techniques, for example, the projection angles for IMRT/VMAT. The settings are given as input to the TPS by the operators. In accordance to the setting parameters, the treatment parameters (including leaf sequencing for fluence modulation in IMRT/VMAT) that optimize the planned therapeutic dose are calculated by the TPS. The treatment parameters are determined by “inverse planning”. Briefly, the planner calculates the 3D dose distribution relying on a virtual therapy simulation having as input the patient image provided with the contours of the target volume and the

organs at risk as well as the planning aims (dose prescription, ...). After this calculation, a quantitative assessment of the dose distribution for a set of control points are evaluated to check if dosimetric constraints are met. If not, the TPS iteratively optimizes the treatment parameters by changing them until a clinically acceptable dose is achieved. Figure 2.17 illustrates schematically the process of radiotherapy planning cycle.

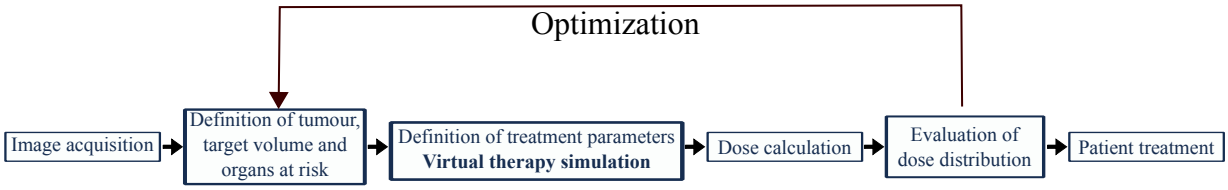

Figure 2.17: Radiotherapy planning cycle [7].

As the dose calculation and evaluation are of concern for this thesis, more detailed information about those processes is in the following.

2.6.1 Approaches to dose calculation

The calculation of 3D dose distributions within the patient is a cornerstone procedure in radiotherapy. The calculation has to satisfy speed and accuracy requirements for clinical implementation. Originally, doses have been calculated using correction factors applied to dose calculation in water to account for irregularities in surface contour and inhomogeneities in tissue. With the increasing complexity of the treatments, this method was replaced by more sophisticated model-based or Monte Carlo dose calculation engines. A brief overview of the predominant dose calculation algorithms used currently in radiotherapy clinics is outlined.

2.6.1.1 Model-based dose calculation engines

In general, most of the model-based methods use convolution kernels that have been precomputed using Monte Carlo simulations. The algorithms differ in modeling methodologies and the magnitude of approximations used to speed up the calculation. Different calculation methods are described:

Pencil beam (PB)

PB is a model-based dose calculation method based on beamlets (pencil beams) generated from predefined energy fluences. The photon beam is therefore assumed as a linear combination of beamlets. The interaction point of the beamlet is assumed to lay on its central axis and the dose deposition in water is defined for each beamlet which is derived from the measured beam data. Here, inhomogeneities are accounted for by scaling the

path length of the dose kernel in water to any tissue according to the relative electron density differences along the beamlet penetration depth. The scaled path length is called radiological length and it is used to calculate the Total Energy Release per unit MAss (TERMA) along the central axis of the PB. TERMA can be calculated using the formula:

$$TERMA = (\mu_{total}/\rho)\Psi_{pr} \tag{2.19}$$

where (μ_{total}/ρ) is the mass attenuation coefficient and Ψ_{pr} is the primary photon energy fluence. Consequently, the dose $D_{\vec{r}}$ is the product of TERMA $T_{\vec{r}}$ and the dose kernel $A(\vec{r}\text{-}\vec{r}')$, which is the dose matrix generated per unit terma, integrated (i.e. equivalent to a convolution) over a volume:

$$D_{\vec{r}} = \int T_{\vec{r}'} A(\vec{r} - \vec{r}')d^3\vec{r}' \tag{2.20}$$

Collapsed Cone
Similar to the PB method, the collapsed cone method uses a convolution between TERMA and the dose deposition kernel. However, the kernel is represented analytically and expressed in polar coordinates. The collapsed cone is based on point spread convolution kernels to be collapsed into a certain number of photon rays of different directions to save considerable calculation time.

Analytical anisotropic algorithm (AAA)
The analytical anisotropic algorithm is based on the pencil beam convolution technique. Different from PB, AAA uses separate models for primary photons, scattered photons, and the fundamental secondary electrons. The radiological length in this case is also used to account for the electron densities in lateral directions. The total doses are obtained by superposing the doses from the photon and electron convolutions.

These models have been extensively tested and compared by several scientific groups [34] [35] [36] [37] [38].

2.6.1.2 Monte Carlo (MC) dose calculation engines

MC simulation methods are based on computational algorithms that utilizes random sampling of physical event probabilities to numerically describe radiation transport. The probabilities for any kind of interaction between the particle and the media rely on fundamental laws of physics or experimentally determined cross sections. The transport of a primary particle is called history. Hence, the number of projected particles determines the accuracy of the MC simulation. It has been estimated that 10^9 events are required to achieve adequate precision of a Monte Carlo simulation for dose calculation in radiotherapy [18]. To achieve the desired accuracy, the MC simulation has to include comprehensive modeling of the electron beam, linac head, patient anatomy and surrounding objects. Comprehensive modeling is computationally expensive and may require access

to unavailable confidential information from the manufacturer, as a consequence, it does not match requirements for clinical routine. The MC dose calculation is the most accurate method to determine the dose distribution in inhomogeneous media. Separately, general purpose codes such as EGS4/EGSnrc [39], Penelope [40], MCNP [41], and GEANT4 [42] have been developed for simulating the transport of electron and photons. As these codes have incorporated specialized features, they have been optimized for radiation therapy proposes. The optimizations include avoiding the full simulation of the treatment head by replacing primary histories with pre-defined phase space or virtual source models [43] [44] [45]. Additionally, these codes are optimized for calculating the dose within the patient, relying on tissue compositions mapped from the CT image and using energy cut-offs satisfying clinical significance. As a result, the optimization reduces the calculation time down to minutes (instead of hours). Examples of these MC dose calculation engines are Voxel Monte Carlo [46] and Dose Planning Methods (DPM) [47]. Commercially, optimized MC dose calculation engines have been recently provided by ELEKTA (Monaco®), Varian (Eclipse®), Brain Lab (iPlan®). A comprehensive comparison between the full Monte Carlo simulation and the optimized one has been published in [48] [49].

2.7 Quantitative assessment of dose distributions

Since the advent of IMRT techniques, it has become standard practice to verify the delivery of IMRT plans using either direct measurement of radiation dose distribution in a phantom [50] [51], or indirect methods that compare the TPS calculation with an independent computer calculation [52] [53]. Both verification methods require a comparison tool to quantify the difference between the two dose distributions. Such comparison is subject to several challenges that make the extraction of clinically significant results difficult. The complexity of comparison increases with the dimensionality of distributions being evaluated. For instance, simple single points (0D) comparison is conducted by calculating the mathematical difference of the reference and the measurement in terms of absolute or relative doses, depending on the situation. The interpretation is straightforward (assuming the data are well coregistered) and a certain threshold can be used to make the clinical decision on accepting or rejecting the result. On the other hand, although the difference between corresponding points of one dimensional (1D) dose profiles can be easily calculated, the 1D comparison results in problematic interpretation of the differences. For example, dose differences could be small in the regions of uniform dose and large in high gradient regions where the alignment of profiles is not perfect. The large difference may or may not be of clinical significance depending on the location in the patient anatomy. This dilemma prevents the use of a single threshold value to accept of reject the result. Additionally, as the dimensionality of dose distribution increases (2D, 3D, 4D), the interpretation of results in the presence of local dose gradients becomes more complex. To handle these complications, different approaches have been introduced to qualitatively and quantitatively compare the dose distributions.

2.7.1 Qualitative comparison methods

Visual inspection of the dose distribution is commonly used in clinics [18]. The main advantage of this qualitative inspection is the fast identification of the major differences between the dose distributions. In practice, several evaluation software packages view the two dose distributions, within the same patient CT, side by side with highlighted dose differences. Other software packages display the dose level contours of the two distributions within the patient CT on one figure. For both display formats, in addition of failing to catch differences in the order of 3-5%, this comparison method leads to interpersonal variability in the interpretation [54]. Thus, a quantitative method is required to support the safety net for the radiotherapy chain.

2.7.2 Quantitative comparison methods

The quantitative comparison is based on calculating the difference of the dose distribution with respect to a reference one. Assuming that the two distributions are coregistered, the comparison can include the relationship between dose level and geometry. In the following, a description of the most used methods in modern clinics is presented.

2.7.2.1 Dose Volume Histogram (DVH)

DVH is a representation of dose distribution within a particular volume of interest (VOI) by means of the frequency distribution of variable dose within the volume. DVH can be defined as differential and cumulative. The differential DVH indicates the volume of a certain structure that receives the dose corresponding to the bin, ranging from the minimum to the maximum dose. Differential DVH provides information about changes in dose within the considered structure and easily visualizes minimum and maximum dose. A cumulative DVH represents the volume of a certain structure that at least receives the dose corresponding to the bin. In other words, cumulative DVH is a plot of dose bins receiving a dose equal to or greater than the indicated dose as a function of volume (or percentage volume). The construction of both types of histograms is outlined in figure (2.18)

Generating a DVH for each dose distribution for which underlying structures exist may help the user to evaluate the quality of the plan and when comparing to a measurement, the user may appraise the contribution of the dose differences to the tumor and organs at risk. However, the accuracy of the DVH curves relies on the accuracy of the dose calculation algorithm, choice of grid spacing, volume delineation limited by the observer bias and imaging resolution [55] [56]. Accordingly, DVHs should always be inspected in conjunction with graphical representations of the dose distributions [57]. A practical comparison of DVH distributions with the aid of 3D viewing of the dose distribution is shown in figure (2.19).

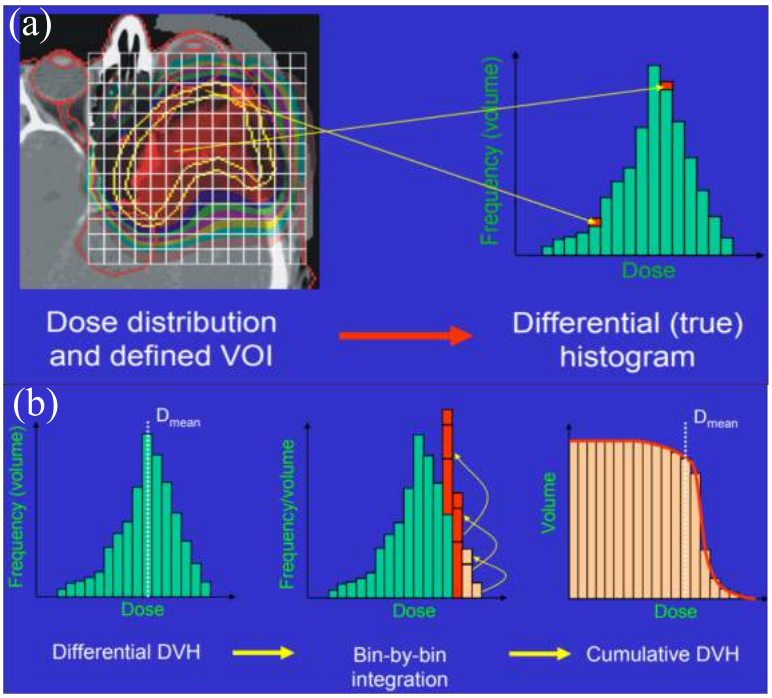

Figure 2.18: Illustration of (a) differential DVH and (b) cumulative DVH. Source: Tony Lomax, PSI, CH.

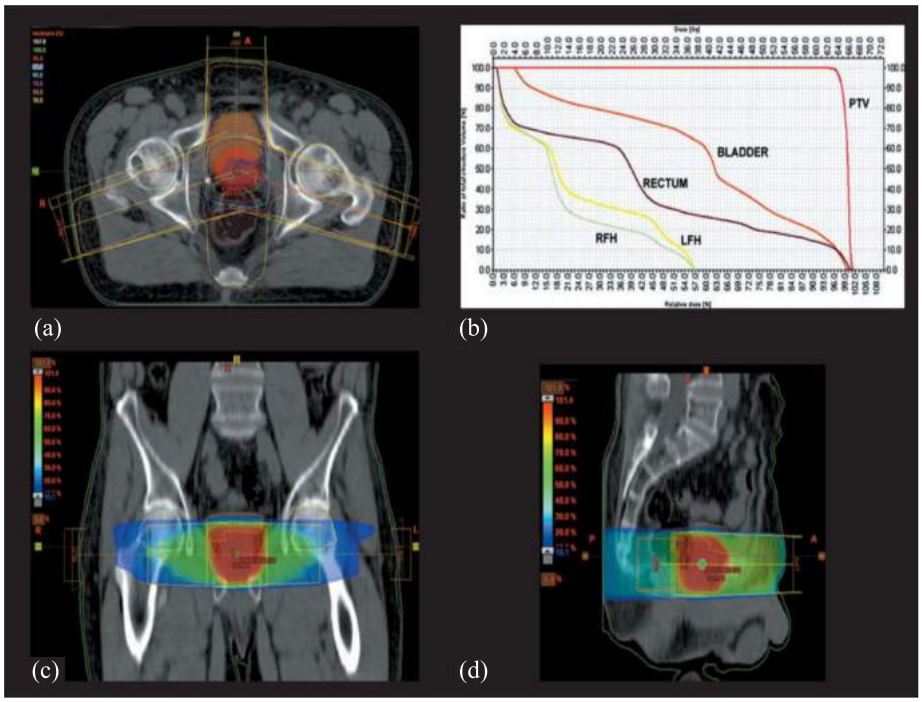

Figure 2.19: Dose distribution of a plan of prostate case showing (a) axial view (b) DVH of doses to the prescribed planning dose volume (PTV), bladder, rectum, left (LFH) and right (RFH) femoral head (c) coronal view (d) sagittal view [58].

2.7.2.2 Gamma analysis

The gamma evaluation is a tool utilizing the criteria of geometric distance to agreement (DTA) and a percentage dose difference (DD) to calculate a gamma index with respect to the reference for each pixel/voxel in an image/volume. Gamma evaluation aims at finding the shortest Euclidean distance between a given point in the reference dataset and the compared dataset in terms of DD and DTA. DTA and DD criteria permit small disagreements between the doses of varying geometric extent and magnitude with reference to dedicated tolerance limits. To calculate the gamma index, a point is taken in the reference dose (RD) and compared to all points in the evaluated dose (ED) distribution in term of DTA and DD. The point in the ED with the lowest gamma index is considered the best match. The search for the best match is limited in a geometrical region of interest (ROI) around the given point in the RD. The gamma index (γ) for a reference point p_r in the RD can be calculated using the equation:

$$\gamma_{(p_r)} = min\{\sqrt{\frac{\Delta d^2_{p_r,p_e}}{DTA^2} + \frac{\Delta D^2_{p_r,p_e}}{DD^2}}\}\forall\{p_e \in \dot{v}\} \tag{2.21}$$

Where p_e is any point within the search circle or sphere $\dot{v}$ of a radius (ROI) in the ED (see figure 2.20). $\Delta d_{p_r,p_e}$ and D_{p_r,p_e} are the geometrical distance and dose difference between points p_r and p_e respectively. Pixels (in 2D evaluation) or voxels (in 3D evaluation) with $|\gamma| > 1$ fail the comparison for the given criteria [59]. Typical tolerance criteria used in IMRT are DD = 3% and DTA = 3 mm [18]. The overall evaluation of the comparison is usually estimated by the result of the percentage of passing pixels/voxels.

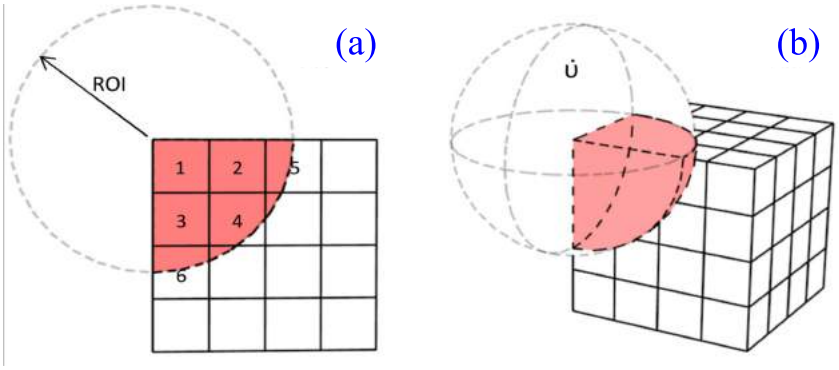

Figure 2.20: Illustration of (a) the circular search region for 2D evaluation and (b) the spherical search region for the 3D evaluation [59].

2.8 Rationale for patient specific pre-treatment QA

As illustrated in the previous sections, dose delivery becomes more complicated with the development of technology. Unfortunately, the complexity adds potential sources of errors, and hence, end-to-end patient management is prone to uncertainty. International and national organizations legislate a series of QA programs to be enforced in radiotherapy clinics. In principle, the primary goal of the overall program is to ensure the correct diagnosis of cancer, the optimum treatment plan, accurate dose delivery and best achievable follow-up program. However, the regulations are falling behind the fast developments in imaging and dose delivery technologies due to various reasons. Research communities are working intensively to develop QA tools and methods to accommodate with new advanced equipments and techniques. The need for more comprehensive QA programs for the new techniques has been presented in several articles [18] [60] [61]. In this thesis, the interest revolves around the pre-treatment QA part of the whole radiation therapy chain.

The International Atomic Energy Agency (IAEA) and International Commission on Radiological Protection (ICRP) conducted several studies on the mis-administration of radiation dose and the causes of the inadequacy of the existent QA programs within the clinics of the study [62] [63] [64] [65]. In brief, the causes includes 1) Incorrect data transfer from the imaging system to the TPS, then to the record and verify system (or oncology information system) and finally to the linac. 2) Incorrect IMRT or VMAT treatment planning especially in the early days of emerging techniques where the dose calculation accuracy was an issue of concern. Moreover, inexperienced handling of new software and delivery techniques could lead to inaccurate optimization process. 3) Mis-calibration of the dose delivery unit. Traditional calibration procedures are not incorporating aspects relevant to advanced dose delivery techniques (finite sizes of the leaves, dynamic MLC, rotating gantry). 4) Inappropriate usage of the dosimeters. Dosimeters are calibrated to specific radiation conditions. The calibration is affected by changes in environmental conditions (such as temperature, pressure ...). Moreover, depending on the goal of the measurement, the choice of the appropriate dosimeter is required. The wrong choice can compromise the accuracy of the measurement.

For those reasons mentioned above, medical physics communities agree on the need for additional components in QA programs [18]. For instance, independent dose calculation engine and dose delivery verification have to be implemented for each patient. The new components have to be compatible with clinical time frame and not add (if not decrease) workload to the personnel. To this end, several approaches have been introduced and translated into certified apparatus and software packages specifically designed for the pre-treatment QA.

Most of the treatment planning systems can create a verification plan that suits the adopted dosimeter and phantom. A region of interest within the phantom that matches

the dosimeter is defined. The dose calculated in the verification plan within the region of interest of the phantom is compared against the measurement performed by the dosimeter. Historically, the pre-treatment QA was performed using single point measurements utilizing ion chambers or TLDs. As an advancement, radiochromic films and 2D arrays of ion chambers or diodes have been introduced within tissue-equivalent or anthropomorphic phantoms. Recently, commercial devices embedding a detector configuration for 3D volumetric dosimetry have also been adopted. Though, these devices rely on interpolation and extrapolation algorithms from several 2D projections (not just measurement) to provide a 3D dose distribution. The only dosimeters that actually measure full 3D dose distributions are polymer gel dosimeters and radiochromic 3D detectors [18]. Though, these types of detectors are not widely used to their passive and single use nature.

Chapter 3

Electronic Portal Imaging Device design and clinical usage

3.1 Background

In radiation therapy, daily checks for accurate treatment setup are crucial. Despite the advances in technology, verification of the dose delivery to the tumour as planned remains practically difficult. The difficulties manifest in several factors which vary daily. Namely, tumor shape, size and location changes over the treatment course which could last for weeks. Moreover, patient positioning on the treatment couch adds uncertainty factors. Hence, a methodology to ensure the intended tumor (and organs at risk) position prior to treatment is required. For decades, film cassettes were used to acquire images from the linac beam or an external X-ray source for landmark localization purposes. The images produced by films are satisfying for the intended purpose but have disadvantages. During the time required for film development, misalignment between the imaging phase and delivery phase can occur. Additionally, imaging using cassette films is labor intensive and extend the treatment time. These weaknesses motivate the development of electronic portal imaging devices (EPID).

In the 1980s, the usage of a fluoroscopic system to acquire megavoltage transmission images was introduced [66]. The proposed EPID was designed as a large flat screen fluoroscopic system. A decade later, manufacturers introduced camera-based fluoroscopic EPIDs. This approach was refined and developed by several research groups leading to the introduction of the commercialized camera-based fluoroscopic EPIDs 3.1. During the 1990s, this type of EPIDs was widely used as positioning imaging device in clinics. However, camera-based EPID has several drawbacks. In particular, the low light output of the fluorescence screen in combination with the poor light conversion due to the lens aperture yields a low Detective Quantum Efficiency (DQE) of below 1%, while large lens aperture would lead to poor resolution due to spherical aberrations [19]. To enhance the DQE, ionization chamber were explored as an alternative detector but filled with a liquid of

much higher density than air. The commercial version of the liquid based EPID consisted of a matrix of 256 $\times 256$ ionization chambers filled with an organic liquid (isooctane) over an area of 32 $\times$ 32 cm^2 [67]. In parallel, medical physicists investigate thin-film photodiodes and transistors for use in photoelectronic imaging devices [68]. The technology subsequently developed into a flat-panel amorphous silicon (a-Si) imaging array system (see 3.2). Since the beginning of of 21th century, most of the EPIDs used in clinics are based on this technology [68]. A comprehensive review of EPID clinical practice is outlined in [69] [70] [71] [72].

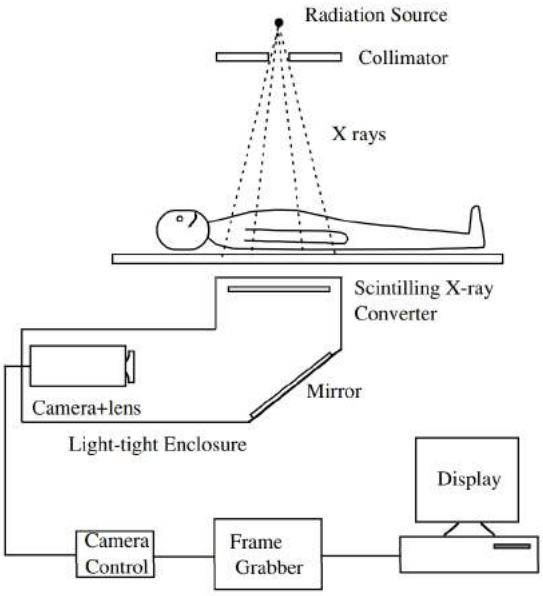

Figure 3.1: Schematic illustration of camera-based EPID [72].

Currently, imaging using EPIDs has applications including the assessment of patient setup before and during treatment delivery and the advanced assessment of patient motion for image guided radiation therapy (IGRT) [73]. Depending on the X-ray beam, different imaging is enabled by EPID. The use of the therapeutic beam enables the acquisition of planar or (by gantry rotation) tomographic MV images. MV images acquired by EPIDs have poor contrast in comparison to kV images due to low DQE of these detectors at the high energies where Compton interactions are dominant. Novel structure designs and image processing methods have been proposed to enhance the DQE and spatial resolution [74] [75]. When EPID is integrated in the linac gantry, also X-ray kV images can be acquired and a cone beam computed tomography (CBCT) can be reconstructed [76].

3.1.1 EPID structure and response to ionizing radiation

As stated before, several EPID designs have been introduced and commercially produced by different vendors. In this thesis, focus is given to the structure and specification of the EPID installed at the University Clinic. In this clinic, the ELEKTA synergy (ELEKTA

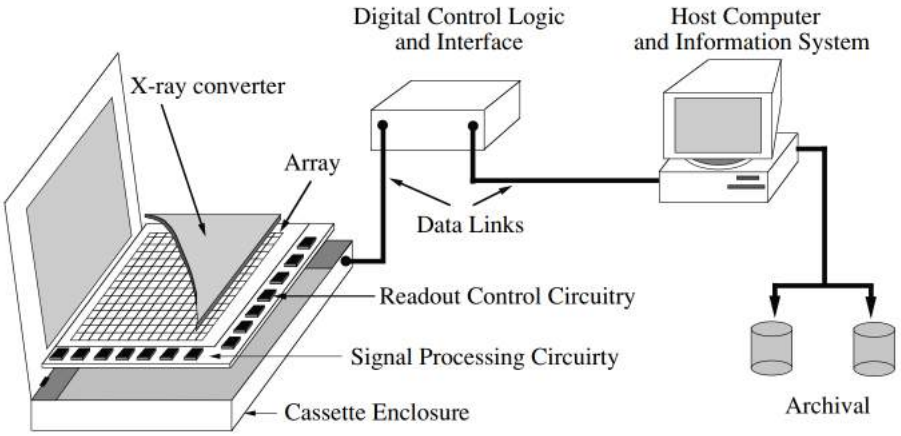

Figure 3.2: Conceptual drawing of a flat-panel imager proposed by [68].

Oncology Systems, Crawley, UK) linac is equipped with the PerkinElmer XRD 1640 AL5 P a-Si EPID (ELEKTA iViewGT).

Modern EPIDs are based on indirect photon to signal conversion, relying on electron to photon conversion mechanism (scintillation). The EPID exploits the so called active matrix flat panel imager (AMFPI) technology [77]. The imager consists of a pixelated photodiode array based on hydrogen-doped amorphous silicon (a-Si: H) semiconductors. Each photodiode is connected to a thin film transistor (TFT) to switch the readout signal, and both are mounted on a glass substrate. A scintillator made of terbium doped gadolinium (Gd_2O_2S:Tb) or cesium iodide (CsI) is sandwiched between the array and a 1 mm thick copper build-up plate. The imager is encapsulated in a low-density plastic cover and laterally connected to a readout electronics. Figure 3.3 schematically illustrates the structure of the EPID.

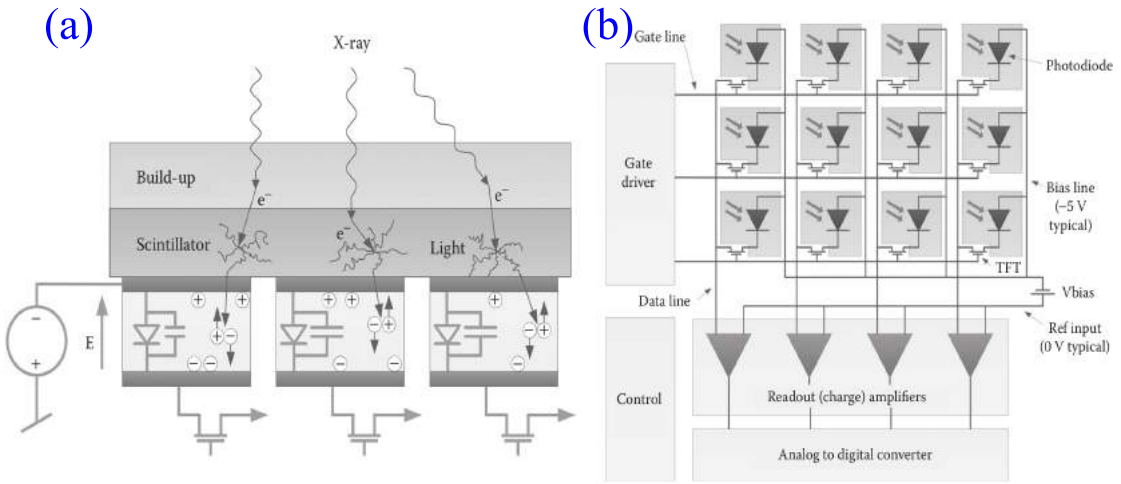

Figure 3.3: (a) Schematic structure of EPID and the indirect conversion of ionizing radiation through scintillation. (b) An example of an a-Si 3×4 pixel array and associated electronics [19].

When the incident ionizing photon beam strikes the imager, the low energy scattered ra-

Table 3.1: Comparison of two state-of-the-art EPIDs.

EPID model	PerkinElmer XRD 1640	VARIAN a-Si1200
Scintillator screen	CsI	Gd_2O_2S:Tb
Pixel number	1024×1024	1280×1280
Active area (cm^2)	41×41	40×40
Pixel size (mm)	0.40	0.39
Maximum frame rate (fps)	3.5	25

diation is attenuated by the build-up plate while the high energy photons are converted into secondary electrons. The converted electrons (and the unconverted photons) interact with the scintillation layer producing a shower (glare) of optical photons which is efficiently absorbed by the photodiode array generating an electric charge. The charge is integrated into the capacitive element of each pixel and controlled by the TFT switch which manages the bias between the photodiodes and the signal line 3.3(a). The unconverted incident photons may be directly detected by the photodiodes, however, the indirect detection has a gain which is one order of magnitude larger [78]. EPIDs using a-Si technology shows a conversion efficiency superior to other technologies, considering that about 50% of the light emitted from the scintillator is converted into a charge signal [72]. Furthermore, solid state technology gives the advantages of almost real-time, digital and pixelated readout with relatively large detection area. Thus, all the modern linacs are combined with a-Si EPID to enable IGRT applications.

Commercially, a-Si EPIDs are manufactured by PerkinElmer® to be integrated into ELEKTA and Siemens® linacs and VARIAN® to be mounted on VARIAN's linacs. Both manufacturers share the same conceptual design [77], though, they vary in technical specifications. The state-of-the-art EPID specifications for the two vendors are given in table 3.1.

3.1.2 Imager readout and acquisition system

The a-Si EPID structure is the same for both manufacturers but electronics and signal readout systems can vary in approach. In this work, PerkinElmer EPID is used and hence, signal readout and image acquisition is presented in depth.

The EPID panel is split electronically into two halves. Each half has eight separate readout regions (ROG). Each ROG is read row by row from the edges to the center, thus in opposite direction for the two halves. Figure 3.4(a) illustrates the electronic separation on a schematic layout of the panel and ROGs while figure 3.4(b) depicts the readout separation effect in an offset image (with no radiation applied).

Using a relatively complex reading layout introduces many advantages. For instance, the

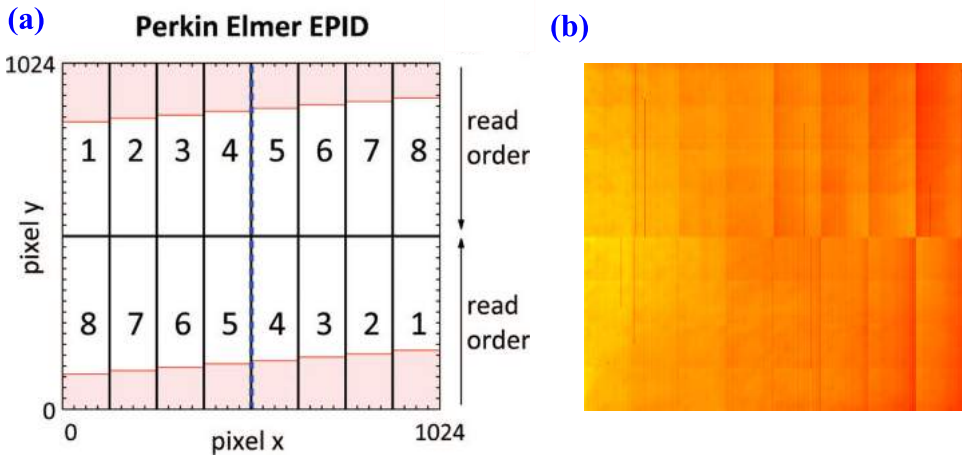

Figure 3.4: (a) Schematic layout of a PerkinElmer EPID with two isolated halves, 8 ROGs per half [79]. (b) Offset image acquired with a PerkinElmer EPID.

reading pattern enables to minimize the bias in signal collection of a large sensitive area, leading to optimized collection time and negligible dead time. Because of the capacitive feature of each pixel, the signal is stored till reading and, subsequently, annealing. After reading completion, the pixel signals are transferred as a single frame to a frame grabber equipped computer. Typically, the frame acquisition time for PerkinElmer EPID is between 0.43 to 0.14 sec. In principle, the frame acquisition time includes the integration time (depending on acquisition setting) and the reading time (depending on electronics). It is worth emphasizing that during signal integration, the pixels keep collecting the signals till the end of acquisition or saturation. This feature is crucial in low dose measurements, which are relevant for this thesis. Figure 3.5 illustrates the readout scheme for each frame.

Image acquisition, in general, follows two modes. Firstly, in integrated mode all image frames are summed to produce a single image. This imaging mode works well for localization purposes but not for tumour tracking, IGRT or dosimetric purposes. Secondly, in cine "or movie" mode image frames are continuously transferred to the computer at a fixed rate. Both major linac vendors (ELEKTA and VARIAN) provide the user with the two modes. Yet, the acquisition options (e.g. spatial resolution, frame rate, image type and extension ...) vary with a dependence on vendor, linac type and operating software (and version).

3.1.3 EPID for dosimetric purposes

EPID has been proved to be a useful tool for landmark localization prior to and during the treatment. Yet, geometrical accuracy does not guarantee the dose delivery to be as planned. To this purpose, several researchers have been proposing the possibility to extract dosimetric information from the EPID images. The fact that EPID has an approximatively linear response to radiation, digital and real-time readout, high spatial resolution and rigid attachment to the linac motivates the researchers to investigate and

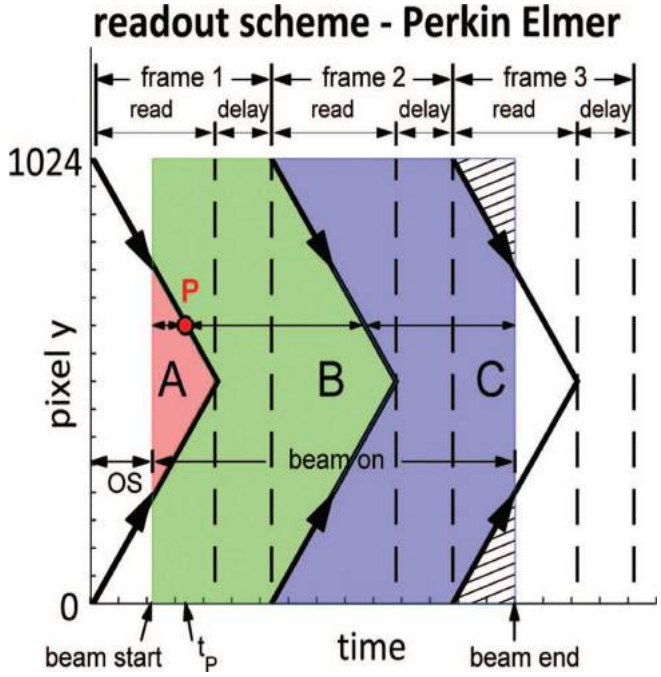

Figure 3.5: Readout pattern of a Perkin Elmer EPID. Regions A, B, and C are the integrated signals from frame 1, 2, and 3, respectively [79]

develop such detector type to fulfill the dosimetric requirements. Before the a-Si EPID introduction, the dosimetric properties of the liquid-filled ionization chamber EPID have been clinically investigated [80] [81]. On the other hand, also the camera-based EPID dosimetry has been studied and developed by several groups [82] [83] [84]. Both EPID-based dosimetry systems showed interesting characteristics and superior advantages over other dosimetric devices back then [67]. Nonetheless, a-Si EPID has paved the way for a new era of EPID-based dosimetry, and almost all modern linacs are equipped with this type of EPID.

3.1.3.1 EPID dosimetric properties and challenges

There is a considerable variety of EPID dosimetric characterization tests in the literature. Although the typical layout of the a-Si is similar for both vendors (i.e. PerkinElmer and VARIAN), technical details like pixel size, array size, image acquisition mode implementation and the physical housing of the EPID make every model somehow unique [18] [85] [86]. Here, the focus will be on the major challenges of PerkinElmer EPID-based dosimetry.

1. **Pixel response linearity with dose**: In principle, the pixel should respond linearly with radiation intensity. In practice this is approximately true but some deviations may occur. These deviations could be due to photodiode saturation, pixel defect, incomplete signal acquisition, ghosting effect or dose rate dependency. The level of

deviation varies with EPID model and acquisition software version. Thus, absolute dose calibration of pixels has to be EPID specific. The literature extensively investigates different EPID types, and several corrections are proposed [79] [87] [88] [89] [90].

2. **Energy dependent response**: EPID exhibits higher response to low energy photons (< 0.5 MeV) as compared to a water equivalent detector due to the increased occurrence of the photoelectric interaction in the copper plate and the scintillation layer (figure 3.6) [91].

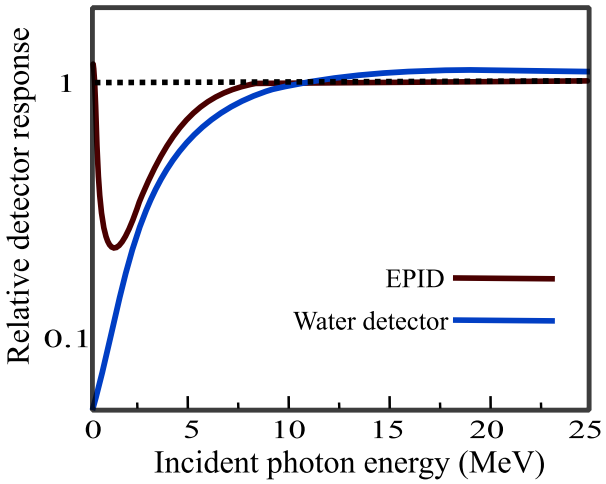

Figure 3.6: Energy sensitivity of an a-Si EPID, normalized at 10 MeV, compared to a water equivalent detector [92].

Over-response could reach 20% difference with respect to ionization chambers, especially in low dose areas (e.g. inter-leaf transmitted radiation). Scatter radiation from the MLC and other linac head components increases the low energy radiation component of the beam. In addition, the EPID component itself adds unwanted scatter to signal. This impacts the readout in the off-axis region and the dose response of different field sizes (regular and irregular filed shapes). Several approaches have been proposed to model the low energy components using simulation or empirical methods [79] [92] [93]. However, modelling becomes harder for the VMAT technique where continuous modulation of the beam shape is applied.

3. **Pixel sensitivity variation**: Each pixel in the a-Si array has a specific offset signal and a specific gain response to radiation. The signal variation is due to the intrinsic response difference between pixels in combination with differences in the readout system [94]. In general, the difference in pixel specific offset and gain response can be corrected by irradiating the entire array to a uniform mono-energetic beam. However, this is not achievable in practice because the linac generates a spectrum of energies with non-uniform intensity distribution. Nevertheless, the non-uniformity of the beam is negligible for imaging purposes and, hence, manufacturers use a

flood-field, that is an open field covering all sensitive area of the EPID, to create a Pixel Sensitivity Map (PSM) and then normalize each pixel response. In contrast, non-uniformity has a significant impact on calibration of the pixel response for dosimetric purposes, especially when the EPID is moved away from the central axis. Two methods have been proposed to create beam independent PSM. In reference [95], authors suggest that using a 10 cm water equivalent build-up medium (above the EPID) could improve the uniformity of the beam intensity. On the other hand, to ensure a uniform intensity irradiation, authors of reference [87] propose a method to irradiate all pixels by a fixed small field at the center. The latter method proved to be more useful for dosimetric calibration.

4. **Optical glare**: The scintillation layer of the EPID converts the incident secondary electron into optical photons to be detected by the photodiodes. A secondary electron yields a shower of optical photons diffused downward resulting in a blurring effect (figure 3.7). The blurring could quantitatively affect the dose, and similar to imaging, should be accurately characterized to compensate for partial volume effect. However, this effect on modern EPIDs is limited thanks to the relatively small thickness of the scintillation layer and the short distance to the photodiode. Though, a simple kernel representing the point spread function of the system response is proposed to enhance image sharpness and consequently dose distributions [96].

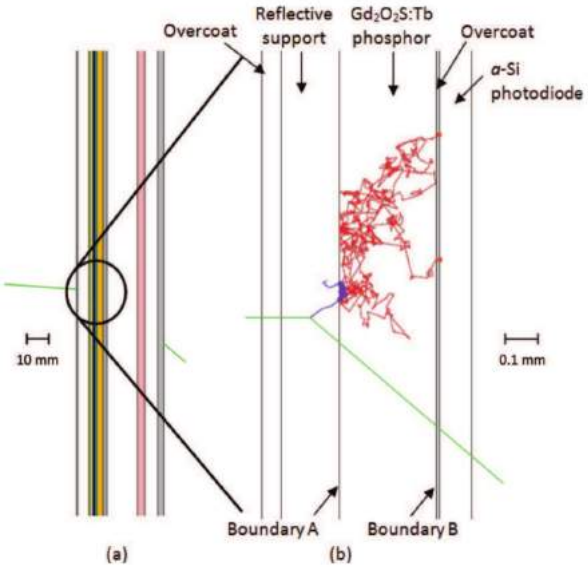

Figure 3.7: (a) An X-ray incident from the left undergoes Compton scattering in the reflective support layer. (b) The Compton electron proceeds and deposits energy within the scintillation (phosphor) layer, thereby generating optical photons. Some optical photons are then absorbed by the photodiode, after scattering throughout the scintillation layer [97].

In the past two decades, researchers have investigated and proposed numerous methods for EPID dosimetry serving several purposes. Extensive reviews about EPID dosimetry have been carried out, covering the period 1991-2008 [67] and till mid 2016 [18]. In

this thesis, the historical development of currently used techniques and methods, covering publications till mid 2018 is presented.
There are more than 100 publications on EPID dosimetry ranging from the investigation of detector properties, problem-solving and developing of new methodologies. In general, the developed methods are either to conduct transit dosimetry or non-transit dosimetry. Transit dosimetry is referred to a dosimetry of a beam passing through media (either patient or phantom) while non-transit dosimetry referred to a dosimetry of unattenuated beam or in–air dosimetry. Though, another categorization could be done based on the dosimetry purposes. Namely, pre-treatment or during treatment (in-vivo) verification dosimetry. Since the thesis is developing pre-treatment verification dosimetry, EPID dosimetry review is categorized accordingly. However, in addition to pre- and during-treatment categorization, each category is sub-categorized in dosimetric dimensionality (i.e. 1D, 2D, 3D or 4D).

3.1.4 Dosimetry for pre-treatment QA

In order to develop a pre-treatment QA dosimetric tool based on EPID technology, the main task is to develop a methodology that enables to compare the dose delivered by the linac with the planned dose distribution. Serving this principle, two main approaches are used to conduct EPID-based dosimetry for pre-treatment QA.

3.1.4.1 2D Dosimetry

- Predicting the EPID image: Using the dose calculation engine of the TPS or independent engines, the expected 2D EPID image obtained by delivering each beam of a treatment plan is predicted. For non-transit dosimetry, this approach has to incorporate two models for prediction. One to account for the energy fluence from the linac head component (including MLC positions) and the other to account for the EPID response (including detective quantum efficiency, dose to signal conversion, attenuation per layer). Predicting 2D images is widely used in clinics nowadays. VARIAN distributes a commercial software (Portal Dosimetry®, Varian Medical Systems, Palo Alto, CA) and numerous investigations have been conducted on different versions of this software [98] [99] [100] [101] [102] [103] or on developed versions of the algorithm [104] [105]. Other groups have independently developed algorithms that predict the 2D image at the EPID level using a dose calculation engine different from the TPS [106] [107] [108] [109] [110]. However, this approach may be designated as 2D verification method rather than a dosimetric method since the EPID image is not a representative of dose in water and cannot be used as a clinical dosimeter.

- Converting the EPID image into dose in water: In order to enable the measurement verification, few groups have developed algorithms to convert 2D EPID images to 2D dose distributions [79] [111] [112]. Other groups have proposed changing the

EPID structure. For example, increasing the build-up plate thicknesses, removing the scintillation layer or adding backscatter shielding. Based on the 2D dose distribution at EPID level, some researchers have proposed methods to reconstruct (back-project) the 2D dose distribution as imparted into a virtual water cubic phantom at patient level [111] [113] [114].

3.1.4.2 3D dosimetry

Two approaches have been proposed to reconstruct a 3D dose distribution in a phantom or patient. In the first method, the EPID image is converted to energy fluence and then back-projected upstream to the linac head level. The back-projected fluence is then inserted to a dose calculation engine to generate the dose within the phantom/patient [115] [116] [117]. The second method has been recently proposed and is based on directly converting the EPID image to 2D dose distribution and then back-project it to a virtual water phantom [118] [119].

3.1.5 In vivo dosimetry

Proposed methods for in-vivo dosimetry are essentially utilized for patient transit dosimetry.

3.1.5.1 1D dosimetry or point dosimetry

As a first step, researchers have worked on finding a correlation between the signal measured by the EPID and the dose along the central beam axis using back-projection algorithms [120] [121]. The approach has gained success due to its simplicity and has been validated for different treatment plans [122] [123]. Several groups have investigated and developed point dose verification even for complex radiation delivery techniques [124] [125]. This approach is also commercially available as SOFTDISO (Best Medical, Italy) and EPIgray (DOSIsoft, Cachan, France).

3.1.5.2 2D dosimetry

As an extension of the point dose verification, authors of reference [126] developed a method to reconstruct a 2D dose distribution at the iso-center level using semi-empirical conversion factors extracted from a measured 2D dose distribution in a water equivalent phantom. A similar approach but using patient radiological thickness (acquired from patient CT) to account for attenuation has been initially proposed in [127] and developed in [128] [129]. Authors of reference [130] have also quantitatively investigated this approach. Another method for 2D verification has been implemented by predicting the dose,

energy fluence or even the image at the EPID level with the presence of the patient. In principle, this approach requires EPID calibration to convert the 2D image into 2D dose distribution or 2D energy fluence or, in case the image at the EPID level is predicted, an exhaustive prediction modeling of the dose delivery and imaging systems. For all cases, the prediction can either use a MC or analytical dose calculation engine [131] [132] [133].

3.1.5.3 3D dosimetry

Instead of predicting the 2D dose distribution at the EPID or iso-center levels, the EPID image is converted to dose or energy fluence, back-projected upstream above the patient entrance point and then inserted into a dose calculation engine to generate the 3D dose distribution relying on patient CT. With minor technical differences, this approach has been proposed by groups [115] [134] and the works are mostly focused on developing the dose calculation to incorporate the variables relevant to VMAT treatment plans [135] [136] [137] [138] [139] [140]. ELEKTA adopted this approach and distributes the system as Iview-Dose software to be exclusively implemented in ELEKTA linacs.

3.1.5.4 4D dosimetry

Recently, the inclusion of the time variable in in-vivo dosimetry has been proposed. The effective clinical need of such approach is argued in [141] [142]. Authors of reference [79] proposed a time-dependent method for EPID dosimetry. This method has been initially proposed for pre-treatment QA and is now under development for 2D time resolved in-vivo dosimetry. A simulation has been recently published proving the feasibility of time-resolved dosimetry [143].

Chapter 4

Dosimetric characterization of the EPID

4.1 Introduction and motivation

The advantages of EPID performing dosimetry were widely presented in the previous chapter. Though, prior to being clinically useful, EPID requires a calibration process supported by several measurements. Literature has proposed numerous methods for calibration. Each method has advantages and disadvantages depending on its specific performance and applicability. The results of these methods vary considerably within different EPID technologies and generally are not even consistent for the same EPID model [90]. When comparing different EPID models, the dosimetric characteristics are influenced also by the acquisition systems [144]. Consequently, there is no a method that can be generally applied to all EPID models. For this reason, a comprehensive characterization of the EPID, including the readout system and the image acquisition modes are required before the establishment of a calibration method. In this chapter, the EPID used throughout this work is characterized in terms of the signal profile, offset signal, image lag, linearity with dose and dose rate, response to different energy spectrum and variation of pixel sensitivity.

4.2 Materials

4.2.1 Linear accelerator and EPID

All measurements were performed on ELEKTA synergy (ELEKTA Oncology Systems, Crawley, UK) linac using 6 MV photon beams. The linac is equipped with Elekta Agility collimator, consisting of 80 leaf pairs and two perpendicular diaphragms and two PerkinElmer XRD 1640 a-Si EPIDs (ELEKTA iViewGT^{TM} and XVI). The two EPIDs

share the same physical structure and electronics except for the additional build-up layer on top of the MV EPID. The XVI EPID is used for kV imaging and is mounted perpendicularly to the X-ray source for the treatment. The iViewGT EPID is the most widely used detector for MV imaging and, unless stated otherwise, it will be addressed as the EPID from now on. The EPID is mounted at a source-surface distance (SSD) of 160 cm (z direction) having the freedom to move in cross-line (x) and in-line (y) directions. The EPID has a sensitive area of 41×41 cm^2 corresponding to a field size of 26×26 cm^2 at the iso-center plane. Detailed technical specifications of the used EPID is outlined in table (3.1). The structure of linac and EPID is typically designed as presented in chapter 2.3. Figure 4.1 shows the outer appearance of the Linac head and the EPID.

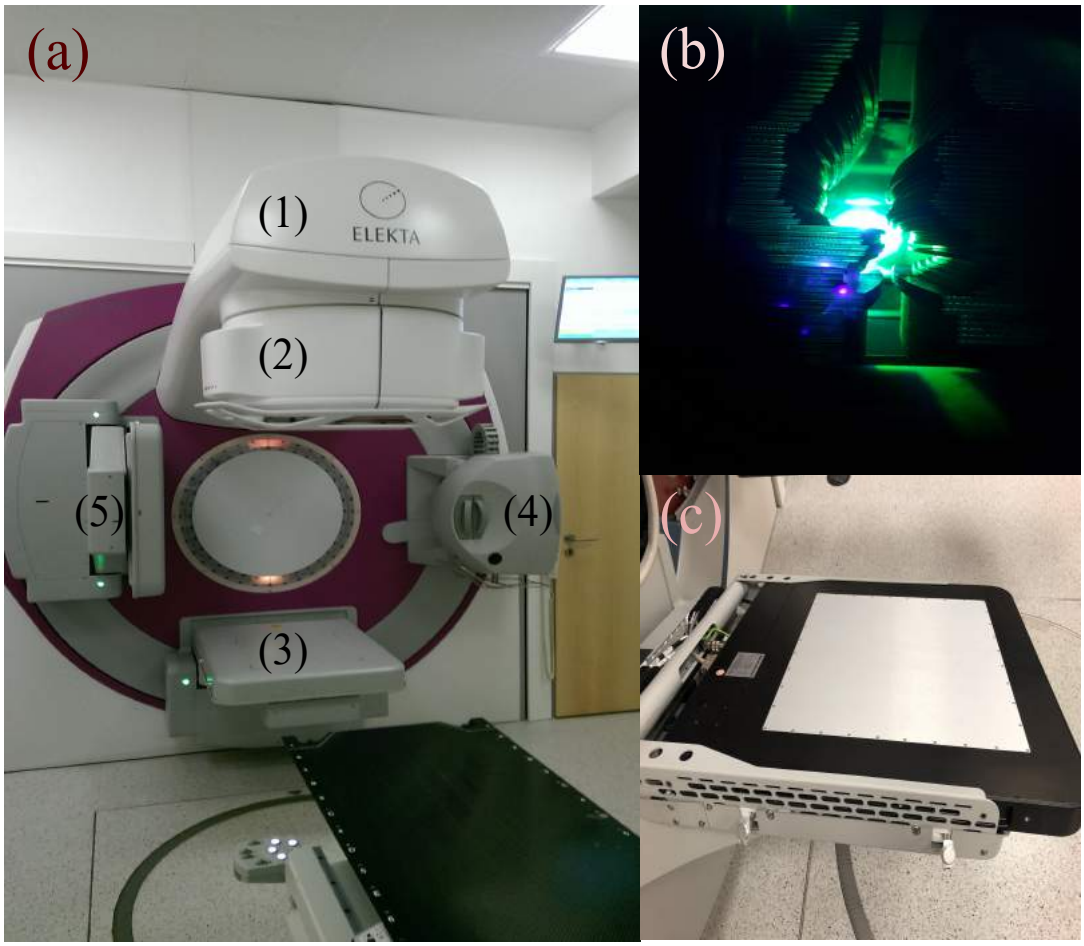

Figure 4.1: (a) ELEKTA linac components: (1) beam source, (2) linac head (includes MLC and jaws), (3) EPID, (4) X-ray source, (5) kV EPID. (b) A picture of the MLC defining the field shapes. (c) The EPID, without the plastic cover.

4.2.2 Image acquisition and software

Originally, ELEKTA has separate Personal Computers (PC) and software for linac, patient data, EPID and kV imaging system. The EPID is connected to the PC (labeled

iViewGT^{TM} as the EPID) via a frame grabber module through an independent digital cable. The frame acquisition is managed using the X-ray imaging software (XIS) provided by Perkin Elmer. The XIS captures 16-bit raw (uncorrected) images in Heinemann imaging (HIS) format. The software includes the different image corrections and adjustment tools. The software offers three acquisition modes: the single acquisition mode, the double or multiple-exposure mode and the movie-exposure mode. For each mode, a frame averaging parameter can be set before the acquisition. However, the number of acquired images is limited to 256 image frames and there is no possibility to enable free raw image acquisition. To overcome this limitation, a stand-alone PC was used to acquire the raw images directly generated by the EPID. The PC was equipped with a frame grabber and and a c++ code (named: iCom-logger) developed at the LMU by Dr. M. Podesta in the framework of the European Society for Radiotherapy and Oncology Technology transfer grant from Maastricht University. ICom-logger is designed to capture the image frames in a free-running mode with a resolution of 1024×1024 pixels and pixel size of 0.4×0.4 mm^2. These image frames were labeled with their acquisition time in time Unix timestamp format with a temporal resolution of hundreds of millisecond. The image frames storage was triggered and stopped manually at the beginning and the end of the measurement and had a frame rate of 2.3 frame per second (fps). In parallel, ELEKTA system includes a package named iCom-Vx which provides an interface between the PC iViewGT^{TM} and the linac control system. The iCom-Vx functions include the automatic selection and creation of patient data and the automated acquisition of images on the PC iViewGT^{TM}. An in-house code was developed to mimic the generation of the linac control system trajectory file (namely, the linac log file). The developed code extracts also the linac output files labeled with time Unix timestamp format in nanosecond resolution. The linac trajectory file registers instead four messages per second.
All image processing conducted in this chapter were carried out using MATLAB (Mathworks Inc., Natick, MA) on an off-line PC.

4.3 Method

The features that are adopted to characterize the EPID are structured according to the following sequence:

1. **EPID signal profile** As described earlier, the EPID collects the signals from the 16 readout regions of the sensitive area according to a specific pattern to produce the image frame. The annealing of the photodiodes after integrating the signal generates a dead time which influences the image frame especially at the beginning and the end of the beam delivery. The general characteristics of the EPID signal profile are assessed during irradiation (beam-on) using the default maximum dose rate (i.e. 530 MU/min).

2. **Offset correction** Each pixel detects a persistent signal so that the pixel value (PV) is always above zero even when no radiation is incident (beam-off). The raw im-

age acquired during beam-off is called offset (also referred to as dark current or dark field) image. The pixel values of the offset image are subtracted from each consecutive image frame allowing response values to start from zero.

3. **Image lag (ghosting effect)** The image lag (also referred to as ghosting effect) characterizes the image frame with the presence of signal from the previous frame(s). This effect influences the absorbed dose by adding spurious signal to the image frame(s) during irradiation (beam-on) or after (beam-off). The effect of the image lag on the EPID signal fall off during beam-off is quantified for doses varying from 2 MUs to 1000 MUs.

4. **Dose response linearity** Linearity of the EPID signal with respect to the absorbed dose is the essential feature required for any detector to be used as a dosimeter. In order to assess the linear response of the EPID, the average signal of a 9 by 9 pixel matrix centered in the image frame is calculated for irradiations with 5, 10, 20, 50, 100, 300 and 500 MUs. To assess the dose response linearity, the cumulative sum of these average signals is reported as a function of dose. The considered acquisition starts 10 frames before beam-on and ends 10 frames after beam-off.

5. **Dose rate dependence** In conventional treatment techniques, the dose rate is constant during beam delivery. In contrast, VMAT is distinguished by the continuous modulation of the dose rate. Hence, the linac is set to deliver a dose corresponds to 50 MU by applying 100, 150, 300, 500 as maximum dose rates (MU/min). The EPID signal is measured for the different dose rates and the deviation with respect to the integrated EPID signals is calculated to quantify the dose rate dependence.

6. **Pixel sensitivity** The individuality of the offset signal exhibited by each pixel on the image frame is manifested also in gain caused by pixel specific response or different efficiency of the readout system. To obtain an estimation of the pixel sensitivity, the EPID is irradiated with a uniform flood-field covering the entire sensitive area (i.e. 26×26 cm^2). Image frames acquired during stable irradiation are averaged and subtracted to the offset image, thus resulting in the pixel sensitivity map. The obtained map is normalized and used to correct for pixel sensitivity the image frame and produce a uniform image.

7. **Field size effect (output factor)** Field aperture has a significant impact on the beam spectrum and energy distribution (figure 2.15). As stated before, the energy dependent response is one of the main difference between the a-Si EPID and the water equivalent dosimeter. To characterize the field size effect, the average of the EPID signal within a central 3 by 3 pixel matrix is determined for irradiation with different field sizes of 3×3, 5×5, 10×10, 15×15 and 26×26 cm^2. For comparison, corresponding reference measurements are performed using the Farmer ionization chamber (IC) in a water equivalent phantom (RW3 slab phantom). The IC is placed at the center of the field at a distance of 160 cm from the source and 3 cm depth in a $30\times30\times30$ cm^3 phantom.

4.4 Results

1. **EPID signal profile**

   The pixel values at the center of the raw image of the EPID irradiated with 10, 50 and 100 MUs are plotted in figure 4.2. The signal profile over time for each dose may be categorized into three regions. (a) The first region starts with non-dose related signal (offset signal) that increases as the EPID is irradiated. This region can be modeled depending on the linac ramp up and the EPID reading pattern. (b) The second region is where the response is expected to be constant, however, it shows a slight fluctuation and gradual increase in gain. (c) The fall off region represents the signals after the beam-off. The signal decreases according to an exponential decay indicating the ghosting effect of the detector (see 3).

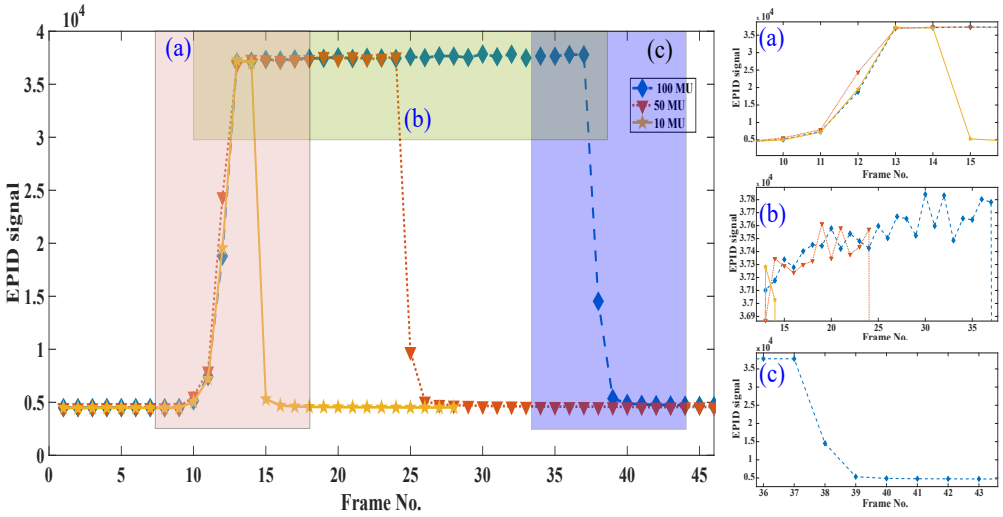

Figure 4.2: The EPID central signal profiles without corrections for 10, 50, and 100 MUs at a dose rate of 530 MU/min. The three regions characterizing the EPID signal profile (a)(b) and (c) are zoomed.

Figure 4.3 illustrates the image frame reading of a 10×10 cm^2 field from the beginning of irradiation till the end. The reading pattern appears to start from the EPID center propagating outward. After few image frames, the EPID shows a uniform reading. After the beam-off, the EPID detects the preserved signal from its center outward to the edges.

2. **Offset correction** Several offset images are acquired after 20 frames, minutes and hours after irradiation. Image ghosting effect (see 3) is found to affect the irradiated regions after the beam-off for minutes, especially with high doses. Though, signals return to the initial state eventually. Figure 4.4 shows an example of an offset image.

3. **Image lag (ghosting effect)**

   In figure 4.5, the pixel value at the center of the image frame recorded by the EPID as a function of time is compared to the delivered dose rate, as obtained from the

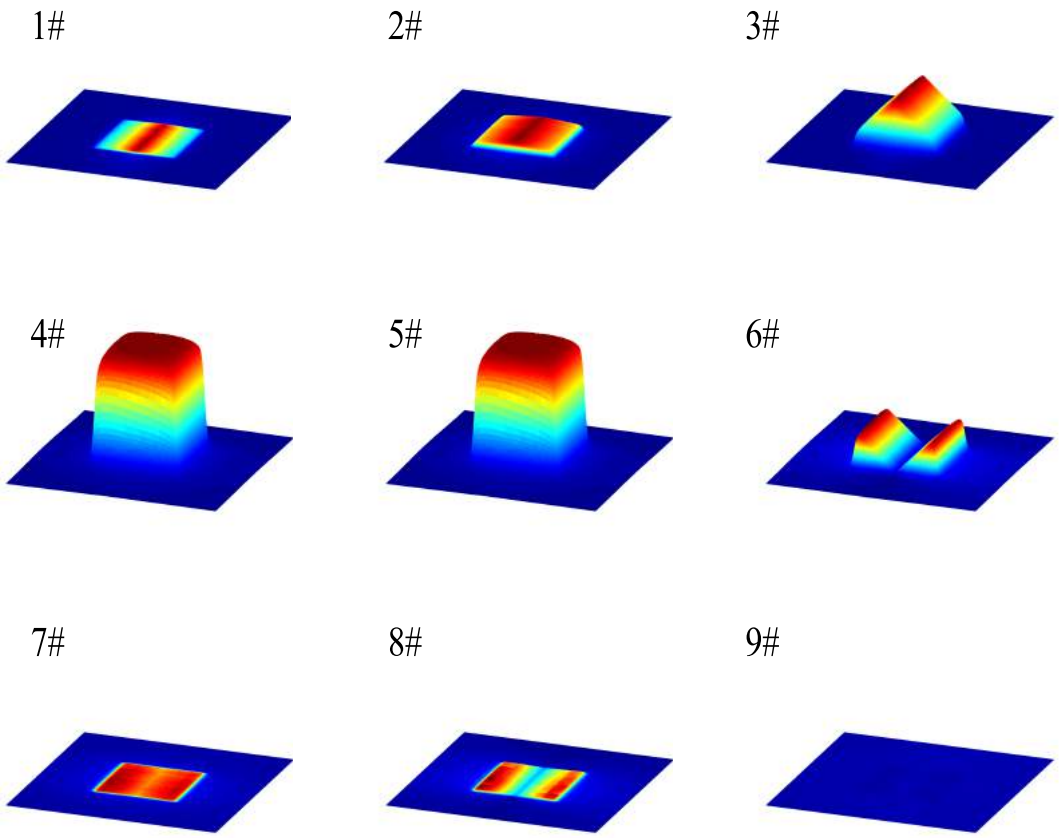

Figure 4.3: Measured image frames indicating EPID reading pattern.

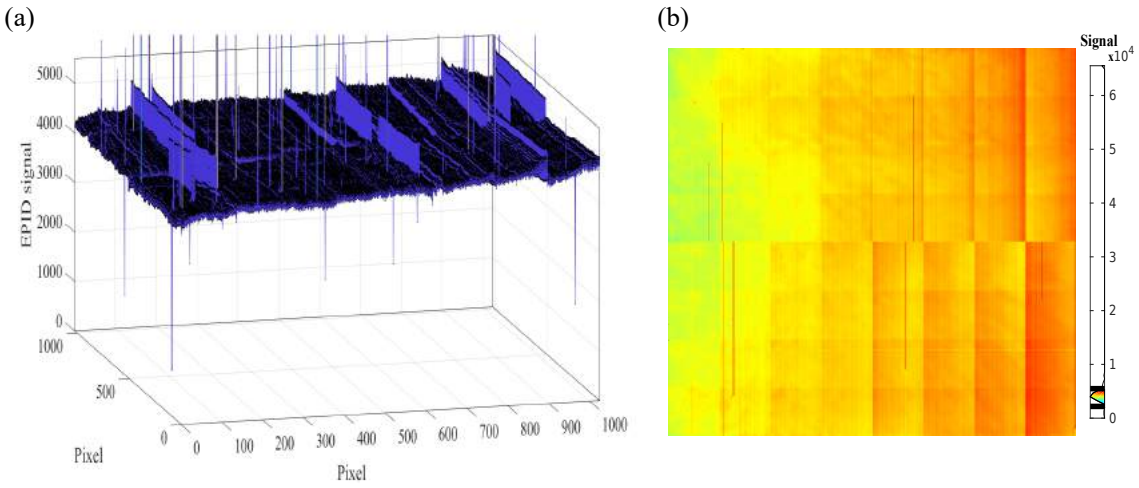

Figure 4.4: (a) Scatter plot of the offset signal. (b) offset (dark field) image.

linac trajectory file. The figure eases the discrimination between direct and indirect effects of the irradiation on the EPID signal. The signal starts a few milliseconds after irradiation and rises up as dose increases. However, the signal keeps increasing slightly even when the dose rate reaches stability. When the beam is off, the signal still gives positive readings indicating the ghosting effect. For quantification, the fall off for different dose rates is illustrated in figure 4.6. For 500 MU, the EPID requires 10 frames to reach 1% difference with respect to the offset in pixel value.

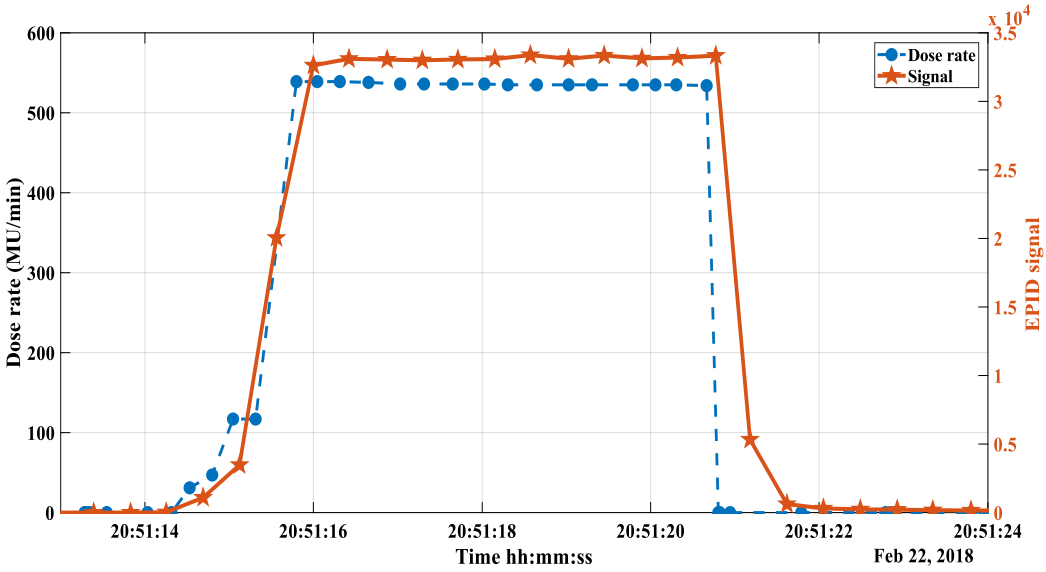

Figure 4.5: EPID signal at the centre of the panel for a 50 MU delivery and the linac output in terms of dose rate. Both plots are in function of time.

4. **Dose response linearity**

   Based on the EPID signal acquisition with different dose rates, the cumulative central signals are reported against doses in figure 4.7(a). A first-degree polynomial fitting function is applied resulting in coefficient of determination $R^2 = 1$. The parameters of the function are expressed in the formula:

$$Dose(MU) = 0.16 \times 10^{-3}(IntegratedSignal(PV)) + 0.33 \tag{4.1}$$

   Figure 4.7(b) is similar to figure 4.7(a) but the ordinate axis is scaled logarithmically to illustrate the validity of the fitting even for low MUs.

5. **Dose rate dependence** Since the dose rate during delivery differs from the one of the user settings, the real dose rate is retrieved from the linac log file as a function of time. In figure 4.8, the central EPID signals are reported for each dose rate. Notably, since the EPID signal starts increasing milliseconds before irradiation, either the recorded time for the dose rate delivery or the EPID frame acquisition time are affected by a time offset. In figure 4.9, the integrated signals acquired for the different nominal dose rates are normalized to the central value and displayed

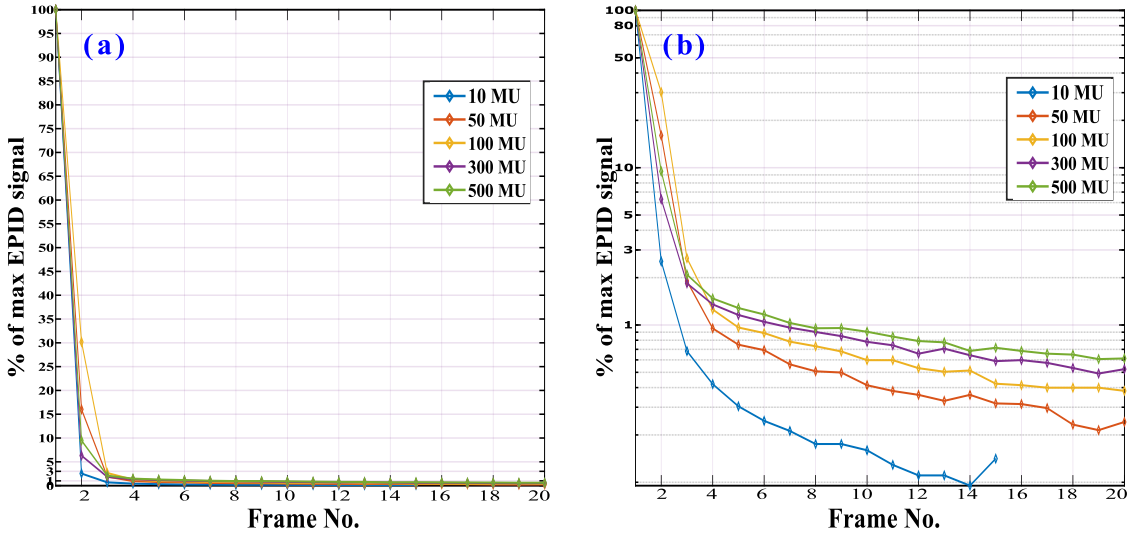

Figure 4.6: Central EPID signal after beam-off for different MUs (a) Linear ordinate axis scale. (b) Logarithmic ordinate axis scale.

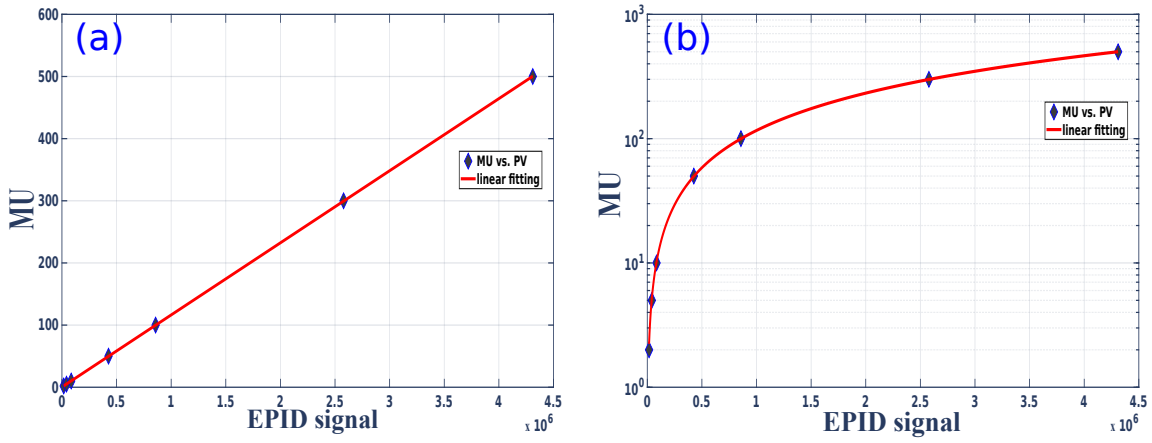

Figure 4.7: Cumulative central signals for different MUs and the applied linear fitting. The ordinate axis is scaled (a) linearly and (b) logarithmically.

against the average real dose rate recorded in the linac log file. The maximum deviation between the integrated signals obtained by the maximum and lowest dose rate is found to be $\approx 3\%$.

6. **Pixel sensitivity** Figure 4.10(a) shows the energy distribution of a flood-field as calculated by the TPS while figure 4.10(b) shows the EPID signal in response to the same flood-field. Normalized cross-line and in-line profiles of both distributions are plotted in figure 4.11.

7. **Field size effect (output factor)** Central doses acquired by the ionization chamber (IC) and integrated central EPID signals are plotted as a function of different field sizes. In both figure, the values are normalized to the value of the 10×10 cm^2 field.

4.5 Outlook

The EPID signal in response to radiation shows the desired features for dosimetry. The EPID provides a real-time image acquisition synchronized with the linac beam delivery. For frame by frame dose representation, however, EPID suffers from ghosting effects which influence the linearity of the overall dose, as already presented in literature [88] [89] [122]. Surprisingly, EPID showed excellent linearity for integrating dose-response comparison even with low doses suggesting two possible explanations. Either the signals recorded after irradiation are dose-related and emerged as a result of signal storing and reading mechanism of the system, and hence, elimination of these signals affect the linearity. Alternatively, the lag is proportional with overall dose elimination of these signals have no direct impact on the integrated dosimetry. Either way, authors of reference [90] suggested that non-linearity can be explained by the lack of image acquisition and read-out system characterization. Nevertheless, the excellent linearity of the ELEKTA's EPID implies that all signals are adequately preserved. The image acquisition software provided by the manufacturer starts the frame acquisition a few milliseconds after beam-on and stops a few milliseconds after beam-off. This results in missing information which demonstrates to be valuable for dosimetric usage of the EPID. Hence, a software enabling the free running image acquisition is needed to account for the offset image (directly before the irradiation) till the fall off. Dose rate shows to have an impact on the integrated EPID signal when compared to the total delivered dose. The difference can be due to the unstable linac output especially for low dose rate. The EPID signal, however, demonstrates a direct correlation with pulses generated by the linac for the different dose rates which gives room for adequate accounting of dose rate dependence. The EPID exhibits non-uniform pixel sensitivity to radiation. Furthermore, the flood-field shows non-uniformity in dose distribution in comparison to the flood-field energy fluence. The signal increases when propagating radially away from the center. Though, the radial distribution is not fully symmetric as the cross-line profile next to the EPID electronics shows over-response than the others. Comparing the fluence and EPID profiles of the flood-field demonstrates the effect of EPID inner scatter radiation and the over response to the off-axis radiation. This effect requires robust correction for pixel sensitivity, as a function of

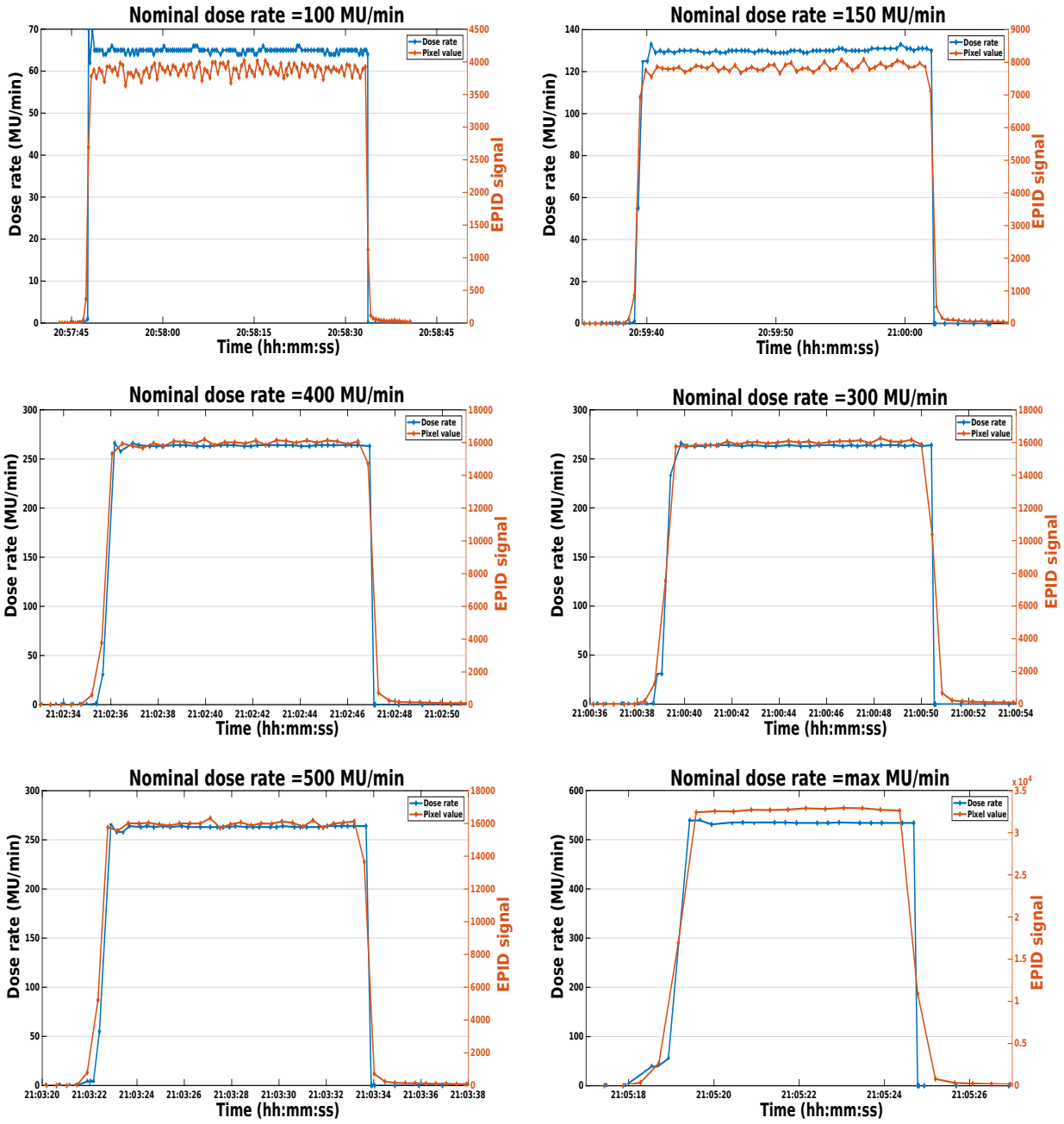

Figure 4.8: Different nominal dose rate sets and the real dose rate recorded by the linac log files in conjunction with the central pixel values acquired by EPID for the correspondent time.

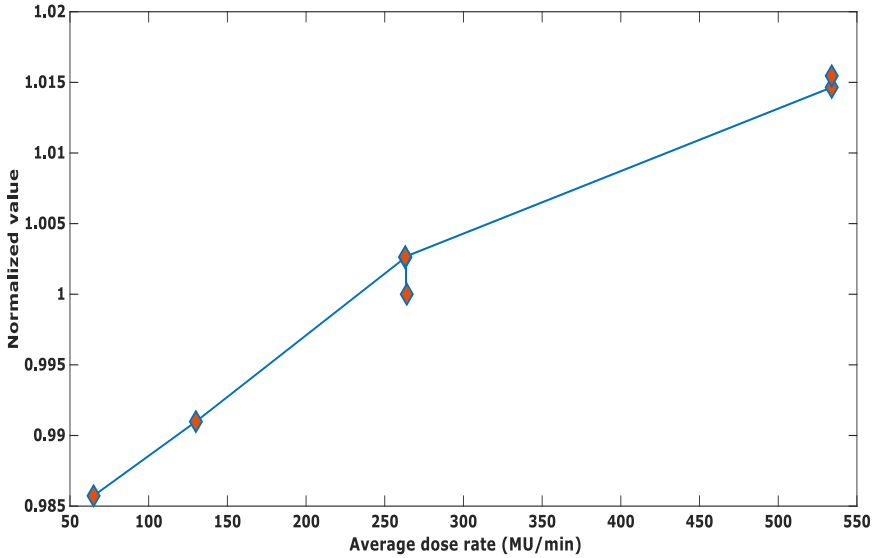

Figure 4.9: Normalized values to the center of the integrated central pixel values as a function of the average recorded dose rates for different nominal dose rates (100, 150, 300, 500, 600 and maximum dose rates (MU/min)).

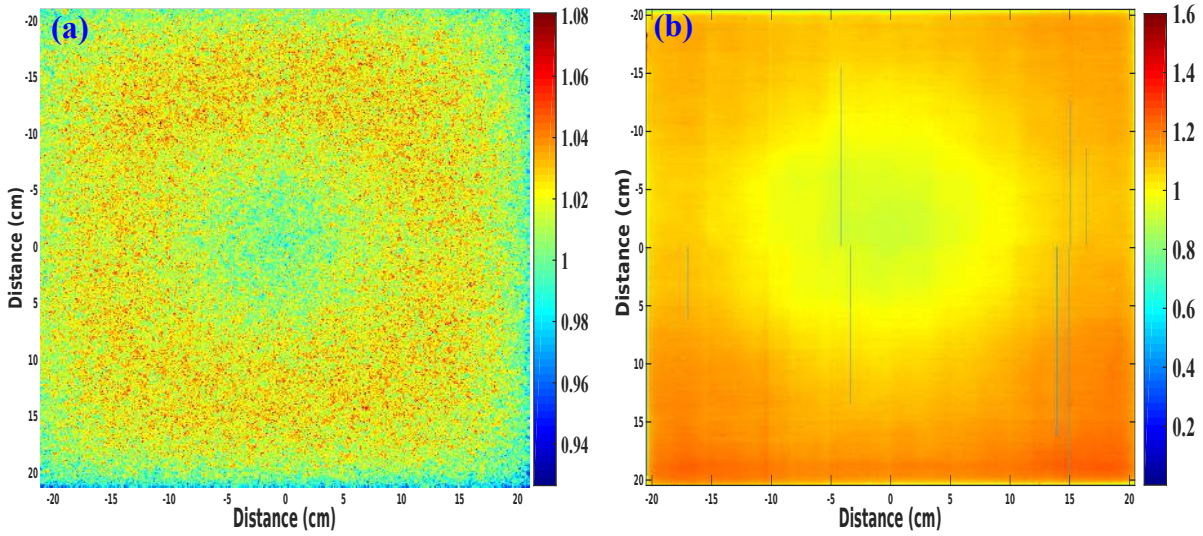

Figure 4.10: (a) Energy distribution calculated by the TPS. (b) Pixel sensitivity as detected by the EPID image.

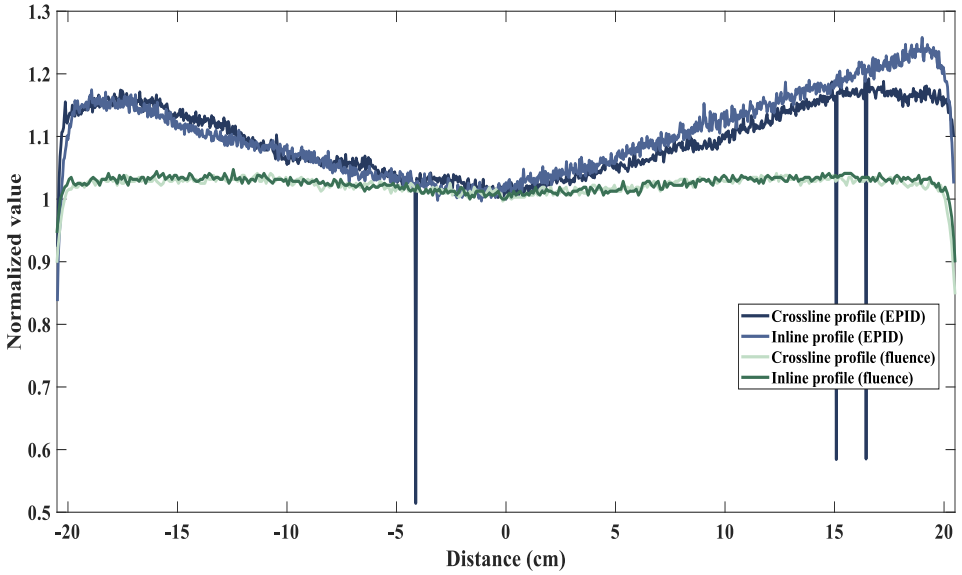

Figure 4.11: EPID profiles and fluence in cross-line and in-line directions.

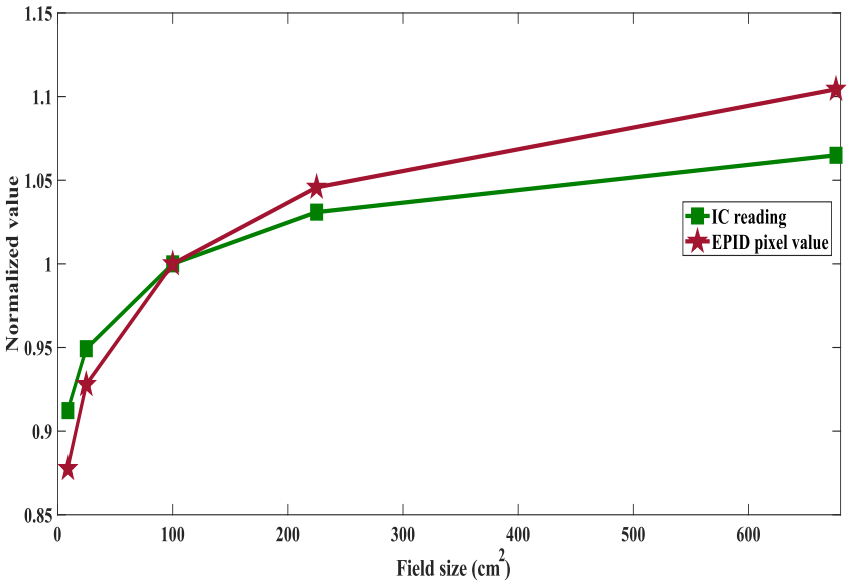

Figure 4.12: Normalized central pixel values measured by the ionization chamber and integrated by the EPID for a fluence of 100 MUs and different field sizes. Both images were normalized to their central value.

the energy fluence. On the other hand, the difference in response between the EPID and the water equivalent dosimeter appears evident when comparing for different field sizes. The over-response (for large fields) and low-response (for small fields) demonstrate the well known energy dependency of the EPID. In conclusion, the EPID has good potential to perform as a dosimetric device. However, several image corrections and calibration methods have to be applied to satisfy the dosimetry requirements for clinical usage.

Chapter 5

EPID calibration to dose in water

In general, two approaches have been proposed in the literature to calibrate EPID for 2D dosimetry. The first approach is based on the conversion of the 2D gray scale image as acquired by EPID to absorbed dose in water while the other relies on simulation (or prediction) of the 2D gray scale image. For both approaches, several methods have been described to satisfy the dosimetric purposes. In this thesis, the calibration aims at generating an independent, fast, accurate and simple pre-treatment QA tool for the different treatment techniques used in the clinic. Knowing that the prediction of the 2D gray images becomes challenging for complex treatment techniques and the accuracy of measurement heavily relies on the prediction integrity [79] [145], the other approach relying on the conversion of the 2D gray scale image to absorbed dose in water has been chosen. For this purpose, a set of calibration measurements is required. Thus, validation can be performed using any clinically available reference dosimeter.
In the light of the characteristics observed on the ELEKTA's EPID in the previews chapter 4, several corrections needed to be applied before calibration. In this chapter, the initial correction includes offset, dead pixels, and pixel sensitivity followed by calibration methods is explicitly developed to fulfill the dosimetric goal.

5.1 Material and Method

The linac, EPID and image acquisition system and software used in this section are the same used in chapter 4. The dosimeters and phantoms used for calibration and validation are declared upon its usage in the following sections.

5.1.1 Offset correction

Prior to irradiation, 5 EPID image frames were acquired without any irradiation and averaged to obtain virtually noise free pixel values. The pixel values were assumed as an

offset of the EPID and subtracted from each image frame acquired in the following.

5.1.2 Dead pixel correction

Due to irradiation or current fluctuation, some pixels may be damaged or poorly responding to radiation. Different from the manufacturer correction based on a threshold, the pixel values were discriminated according to their linear or non-linear response. All the pixels were irradiated with flood-field of intensity equal to 100 MU, and 20 image frames within the stable beam were acquired. For each pixel, the sum of 20 image frames was divided by the sum of the first 10 image frames. The pixels deviating from linearity by more than 1% were marked as dead pixels. The procedure led to a binary mask. The mask was then used to correct each image frame in the following by replacing the dead pixel with the average value of the 8 neighboring pixels.

5.1.3 Pixel sensitivity correction

Although the pixels respond linearly to the intensity of irradiation in general, they can be characterized by different response rates. This difference can be accounted for in image processing by using the sensitivity characterization presented by [87] and improved in [79]. All pixels of the EPID image frame were meant to be irradiated with photon beams of the same intensity and spectrum. However, the beam intensity and spectrum are not uniform. Besides, the uniformity is additionally compromised by the scattered beam from the EPID. Exploiting the movability of the EPID in cross-line and in-line directions, the EPID at first, was irradiated with a static 10×26 cm^2 rectangular field, centered to the EPID to gain maximal uniformity. The image frames were acquired while moving the EPID along the x-direction in 4 cm step size. Then, a static 26×10 cm^2 rectangular field at the center was used, the EPID was moved along the y-direction in 4 cm step size and the image frames were acquired. The in-line profiles were combined to form the in-line 1D profile. Figure 5.1 illustrates the acquisition process. The field size and step size were chosen according to a trade-off between accuracy and efficiency (acquisition time) of the calibration. With reasonable approximation (deviation less than 0.5%), the central 2×2 cm^2 of each square field is relatively uniform. The 2 cm cross-line profile at the field center was extracted from the cross-line profiles and then combined to form the 1D cross-line profile. In similar fashion, The 2 cm in-line profile at the field center was extracted from the in-line profiles and then combined to form the 1D in-line profile. The obtained 1D cross-line and in-line profiles were then divided by the corresponding profiles obtained with flood field. The result produced a cross-line and in-line profiles surrogating the beam inner scattering from the EPID. Assuming that the two surrogate profiles are radially symmetric, the mean of the two surrogate profiles was taken to reduce the noise. A 1D Gaussian function was used to fit the mean profile. The fitted function was then radially interpolated covering the EPID size, thus forming a 2D map of the inner scattering surrogate. The pixel sensitivity (PS) map was obtained by dividing the flood-

field image frame with the 2D map of the inner scattering surrogate. Each image frame in the following was corrected for sensitivity by multiplying the pixel values with the obtained PS map.

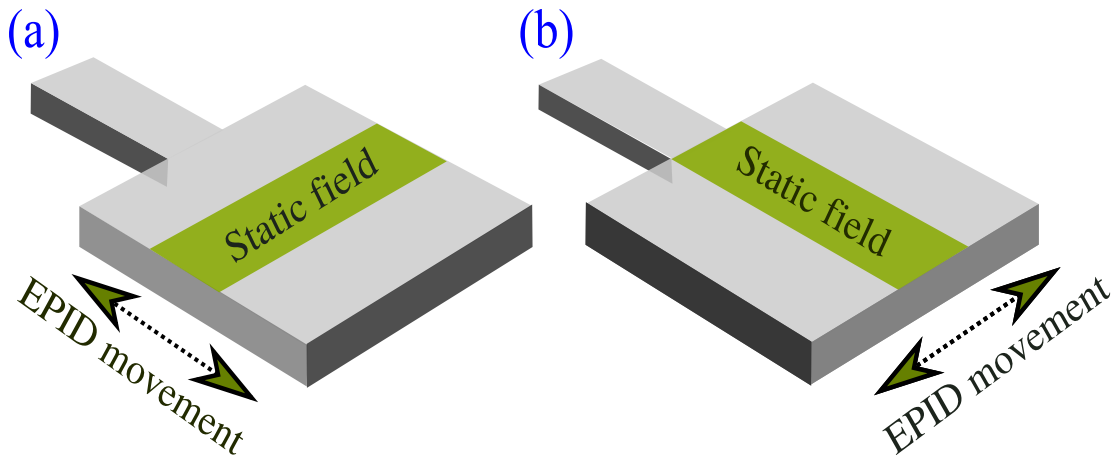

Figure 5.1: A sketch illustrating EPID image acquisition needed for PS correction during (a) movements along in-line direction and (b) movement along cross-line direction.

5.1.4 Relative off-axis ratio (ROAR)

As the beam inner scattering and the angular response in water differ from those in EPID media, an Off-Axis to central-axis Ratio for the water equivalent detector (OARw) and for the EPID (OARe) were defined. Opposite to PS correction, the EPID was fixed, and the square field moved along cross-line and in-line directions during image frames acquisition with 4 cm shift (figure 5.2). Similar to PS correction, cross-line and in-line profiles were combined and averaged. The mean profile was fitted with a second-degree polynomial function. Radial interpolation of the fitted function on the EPID image frame produced the 2D OARe. Subsequently, the corresponding reference measurement using a Farmer ionization chamber (PTW, Freiburg, Germany) (Type No. 30013) was performed in a water equivalent phantom (RW3 slab phantom), fitted and radially sampled to define the 2D OARw. The division of the OARw by the OARe produced the 2D relative off-axis ratio (ROAR) map. Each image frame in the following was multiplied by the 2D ROAR map to correct for water and EPID media difference.

5.1.5 Field size and penumbra correction

The primary photons generated from the beam source are contaminated by the scattering photons from the multi-leaf collimator (MLC) and other linac components. As the adaptation of the field size changes the spectrum of the irradiation, the energy dependence of the EPID response has to be corrected to match the reference dosimeter. Furthermore, the correction has to include the scattering from the EPID itself. Hence, the dose, as imparted

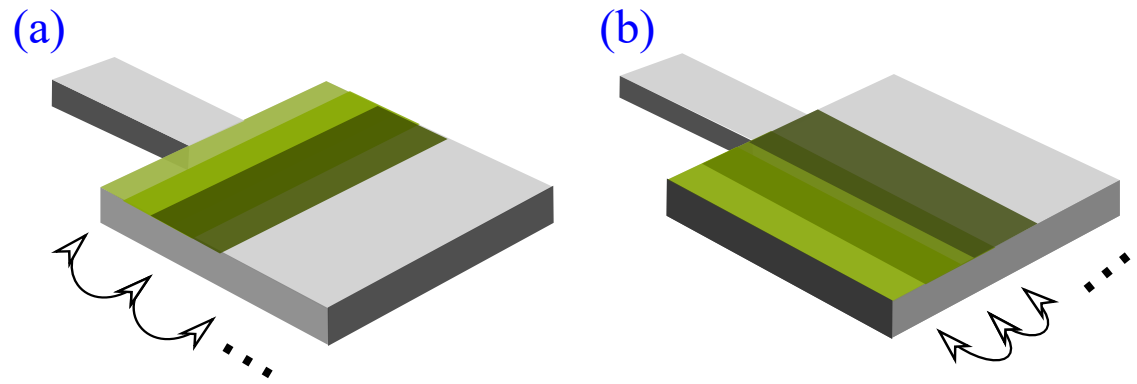

Figure 5.2: A sketch illustrating fields shift in (a) in-line direction and (b) cross-line direction with fixed EPID for ROAR correction.

to a water equivalent medium, and the characterization of the EPID response as a function of different spectra are required. The overall difference between the EPID response and the reference dosimeter can be modeled by two convolution kernels. For both field size and penumbra corrections, the choice of the fitting functions was empirically justified by a negligible fitting error. The first kernel corrects for the filed size dependence and the second one corrects for the lateral energy deposition and the shape of the penumbra, as detailed in the following. For field size dependence, a radially symmetric kernel was defined by an exponential fitting function with single decay coefficient. The unknown kernel was convolved with the integrated EPID image frames irradiated with 100 MU and square field sides of 3,5,8,10,15 and 26 cm. The central value resulting from the convolution was then compared with the reference measurement using micro-diamond detector (PTW, Freiburg, Germany) (Type No. 60019) for the corresponding field size. An iterative optimization algorithm was implemented to find the best coefficient of the exponential fitting equation minimizing that difference for each field size. The implementation of the mathematical optimization is explicitly outlined in appendix (A). The coefficients produced from the optimization were fitted to cover all possible field sizes with a second-degree polynomial fitting function. For each EPID image frame, the field area was determined by the number of irradiated pixels, considering that the energy spectrum depends on the field area of the MLC, but not on the shape [31]. For penumbra correction, in-line profiles of different field areas of MLC, as reported in figure 5.3, were measured in a water phantom using the micro-diamond detector as reference dosimeter and compared to the EPID image frame. An unknown kernel was defined by a Lorentz fitting function with 4 coefficients for each field area of the MLC. Unlike the field size correction, a constraint was introduced into the iterative optimization algorithm to normalize the maximum value of the central in-line profile. In other words, the optimization had the freedom just to redistribute the penumbra fall-off. All the EPID image frames in the following were convolved with the two obtained kernels.

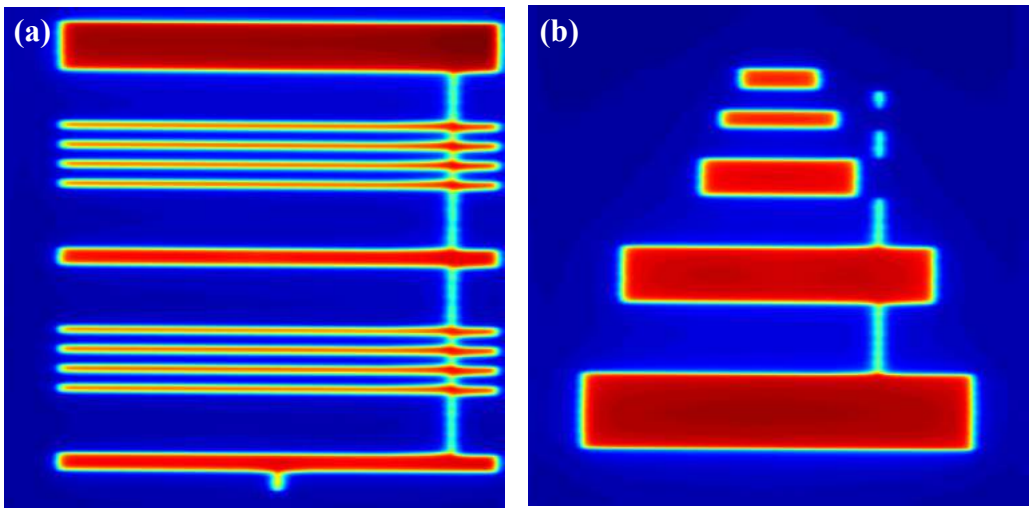

Figure 5.3: (a) and (b) EPID image frames highlighting the fields (#1 and #2) used in penumbra correction.

5.1.6 Pixel value to dose conversion

Using the micro-diamond detector as reference dosimeter, the absolute conversion factors from pixel value to dose were obtained. A measurement of the central dose for 10 $\times$ 10 cm^2 field size was performed for dose values corresponding to the delivery of MUs ranging from 2 up to 1000 MU using a fixed intensity rate of 530 MU/min. The correspondent doses was delivered to the EPID, acquiring 10 image frames after the beam delivery. The sum of the image frames was plotted against integrated doses measured by the reference dosimeter. A linear fitting was used to convert the pixel value to dose of each image frame.

5.1.7 Validation

For validation, firstly, cross-line profiles of calibrated EPID image frames obtained with different square field sizes and acquired in air were compared to corresponding reference measurements using micro-diamond detector in a water phantom. Then, a set of calibrated EPID image frames of static and step-and-shoot irradiation were validated with respect to reference measurements based on the diode array detector MapCHECK 2 (Sun nuclear corporation, Melbourne, USA) (Model No. 1177) with maximum sensitive area of 32 $\times$ 26 cm^2. MapCHECK 2 was inserted in a water equivalent phantom (RW3 slab phantom) at the EPID level (SSD = 160 cm) with 3 cm build-up and 15 cm backscatter.

5.2 Results

5.2.1 Dead pixel correction

The number of identified defected (dead) pixels is 14 over the total 1048576 pixels of the EPID image. Figure 5.4 highlights the dead pixels on the EPID image.

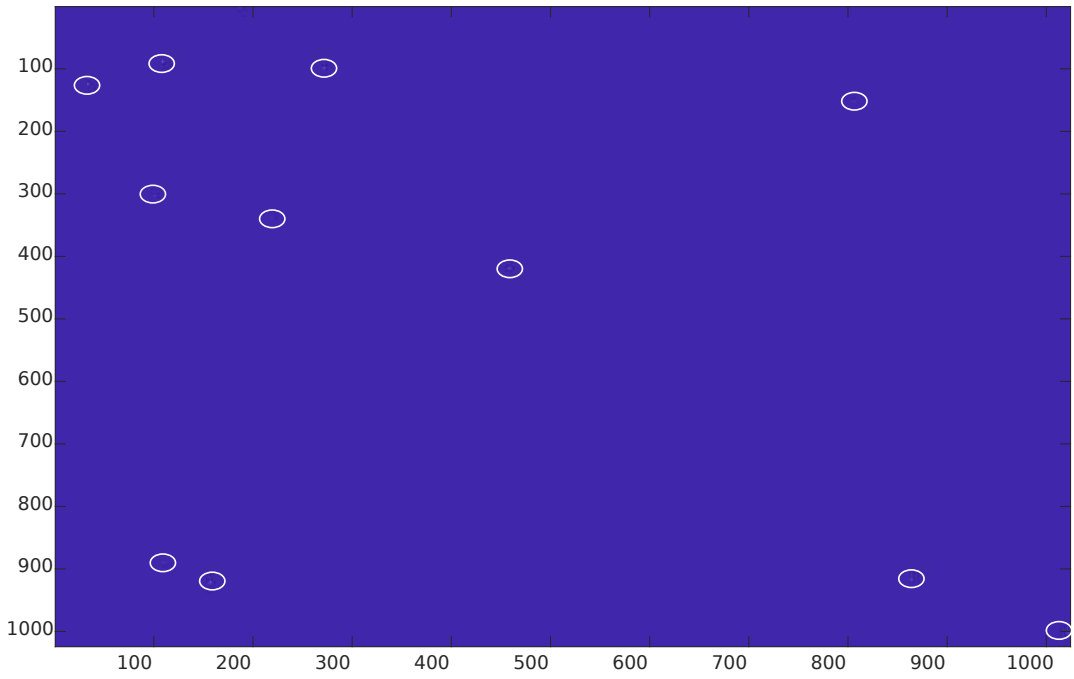

Figure 5.4: The circled dead pixels of the EPID image.

5.2.2 Pixel sensitivity correction

The profiles obtained by moving the EPID in in-line and cross-line directions are plotted in figure 5.5 along with their correspondent profiles of the flood-field. The second-degree polynomial function used to fit the profiles is reported in figure 5.6. The correction based on the senstivity map is depicted in figure 5.7, where the uncorrected and corrected flood-field EPID images are compared.

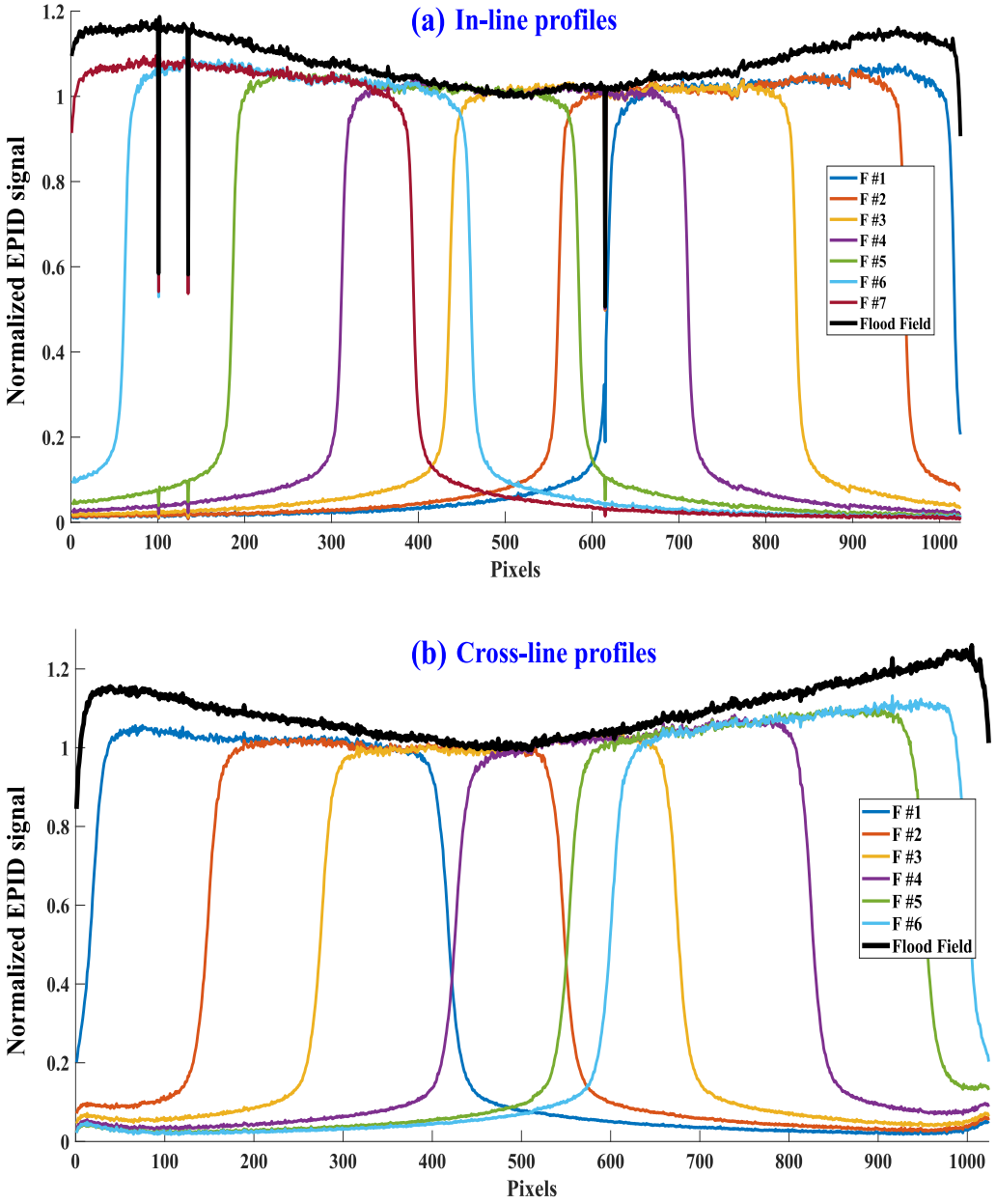

Figure 5.5: Profiles acquired by moving the EPID and the corresponding flood-field profiles for (a) in-line and (b) cross-line directions.

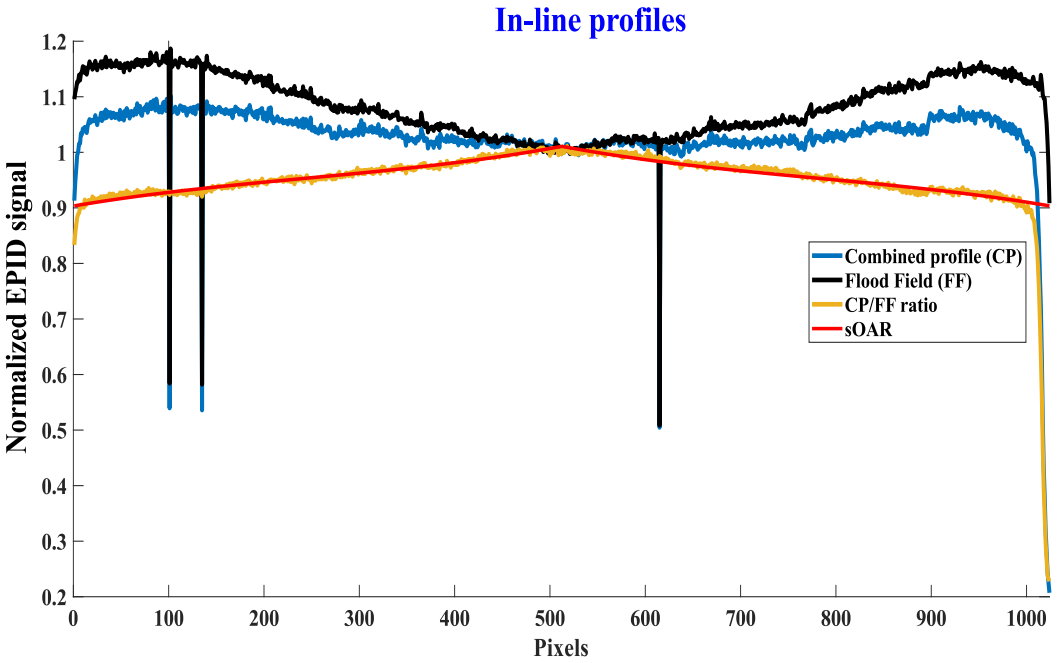

Figure 5.6: Combined profile for the in-line direction along with the flood-field profile. The ratio between the two profiles and its fitting is highlighted.

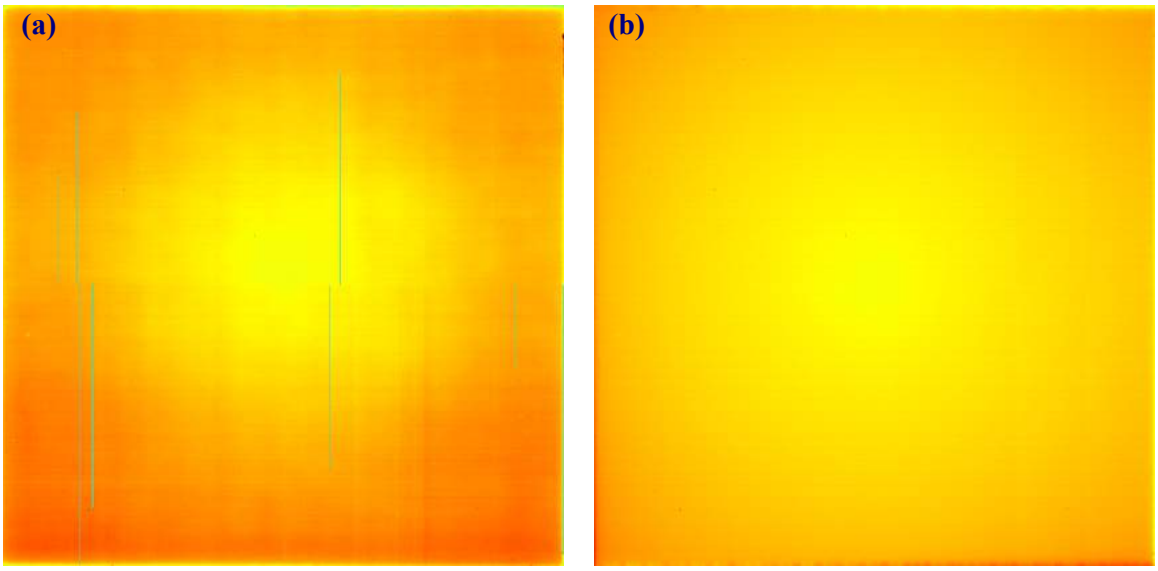

Figure 5.7: Pixel sensitivity (a) uncorrected and (b) corrected flood-field image.

5.2.3 Relative off-axis ratio (ROAR)

Figure 5.8 shows the process of generating ROAR. Figure 5.8(a) illustrates profiles acquired by EPID when moving fields in in-line and cross-line directions, respectively. Figure 5.8(b) compares between in-line profiles acquired by EPID and micro-diamond detector. Figure 5.8(c) shows the combined profile of the cross-line profiles. Figure 5.9 shows the resulted ratio between OARw and OARe interpolated radially forming the 2D ROAR.

5.2.4 Field size and penumbra correction

Figure 5.10 shows the central doses for square field sizes of 3^2, 5^2, 10^2, 15^2 and 26^2 cm^2 normalized to the 10×10 cm^2 field acquired by the micro-diamond detector and EPID and the corresponding field size correction. As visible in figure 5.10, the field size correction brings the uncorrected EPID images to the reference measurement.

For penumbra correction, the results of the convolution between the generated kernel and the EPID image is reported in figure 5.11(a). The in-line profile is detailed in figure 5.11(b) in comparison with the profiles obtained by micro-diamond detector and the (uncorrected) EPID image.

5.2.5 Pixel value to dose conversion

The relation between the integrated dose measured by micro-diamond detector and the corrected integrated central EPID pixel values for dose values corresponding to the delivery of MUs ranges from 2 up to 500 MUs is plotted in figure 5.12. The relation is defined by a liner fitting function as follows:

$$Dose(mGy) = (0.00046) \times pixelvalue + (0.75) \tag{5.1}$$

5.2.6 Validation

The comparison shows visual good agreement between the reference measurements and the calibrated EPID image frames (figure 5.13). For 2D comparison, the dose distributions obtained with MapCHECK 2 detector and the calibrated EPID image frames for different static and dynamic fields are illustrated in figure 5.13. The 2D global gamma evaluation using (3%, 3 mm) criteria results in above 99% passing rates for all the considered dose distributions.

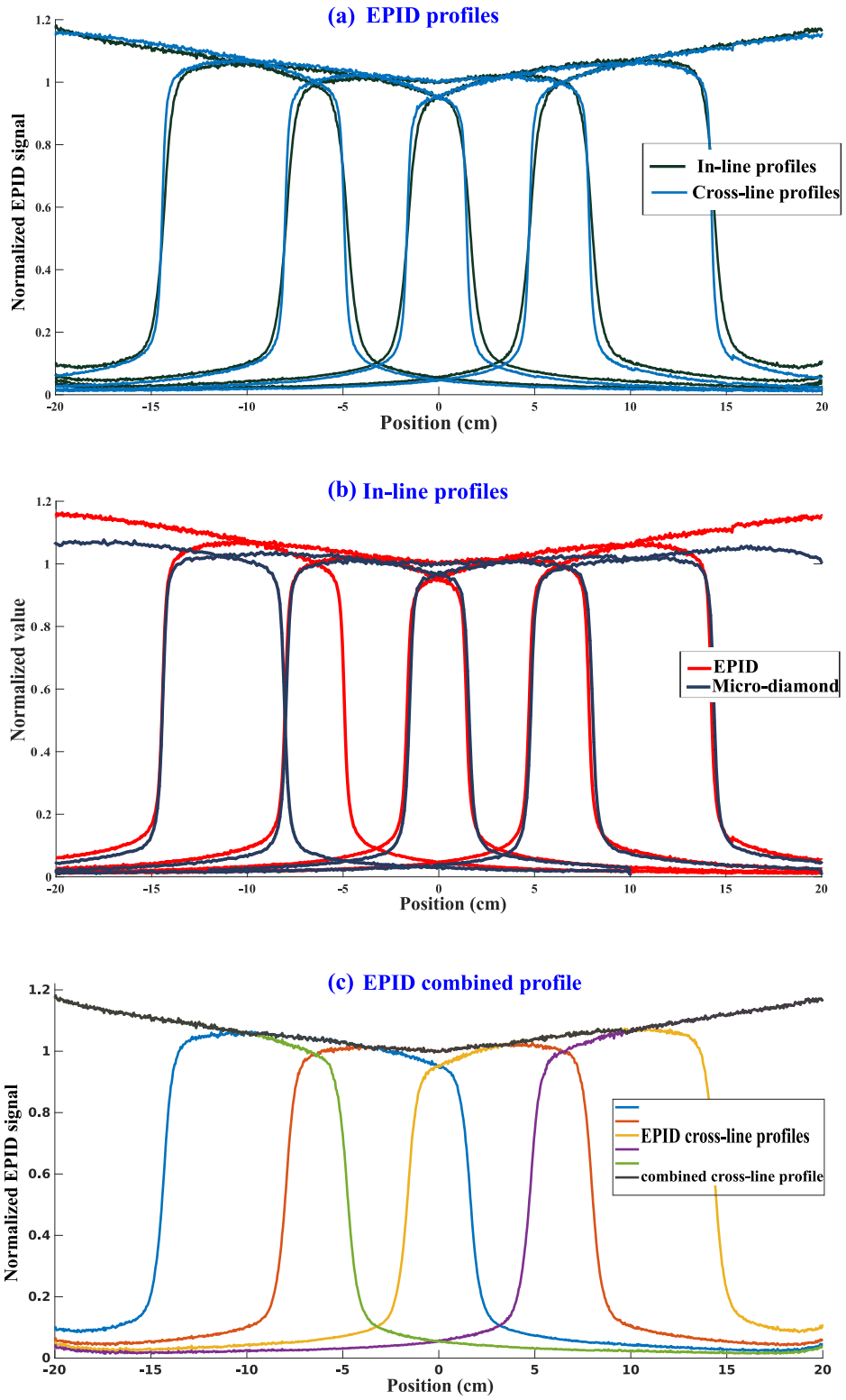

Figure 5.8: (a) In-line and cross-line profiles acquired by EPID for different fields. (b) Comparison between in-line profiles acquired by micro-diamond detector and EPID. (c) Example of combined cross-line profile.

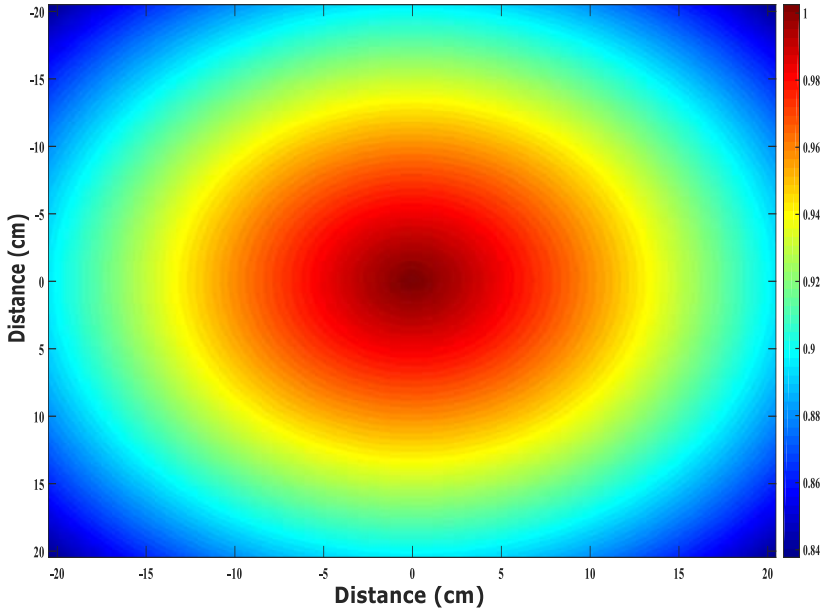

Figure 5.9: The resulting 2D ROAR.

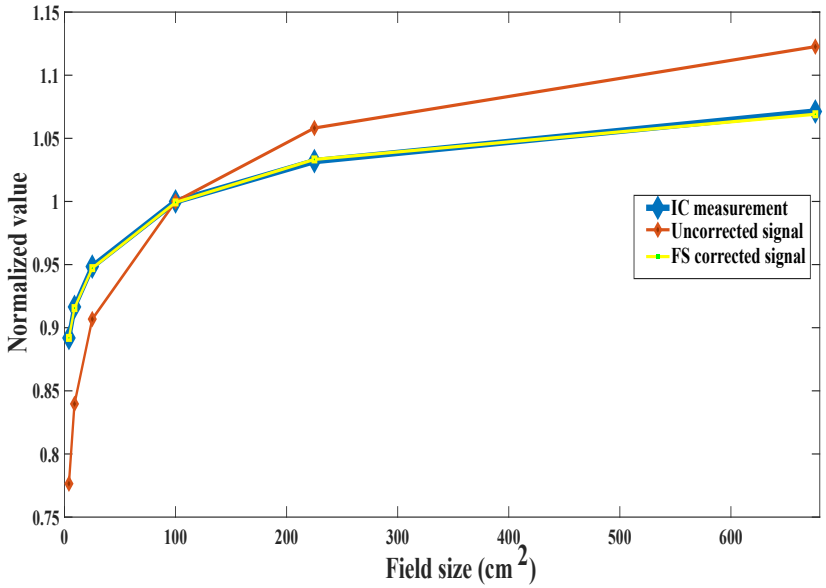

Figure 5.10: Central relative doses for different field sizes normalized to the center values measured by ion chamber and EPID before and after field size correction.

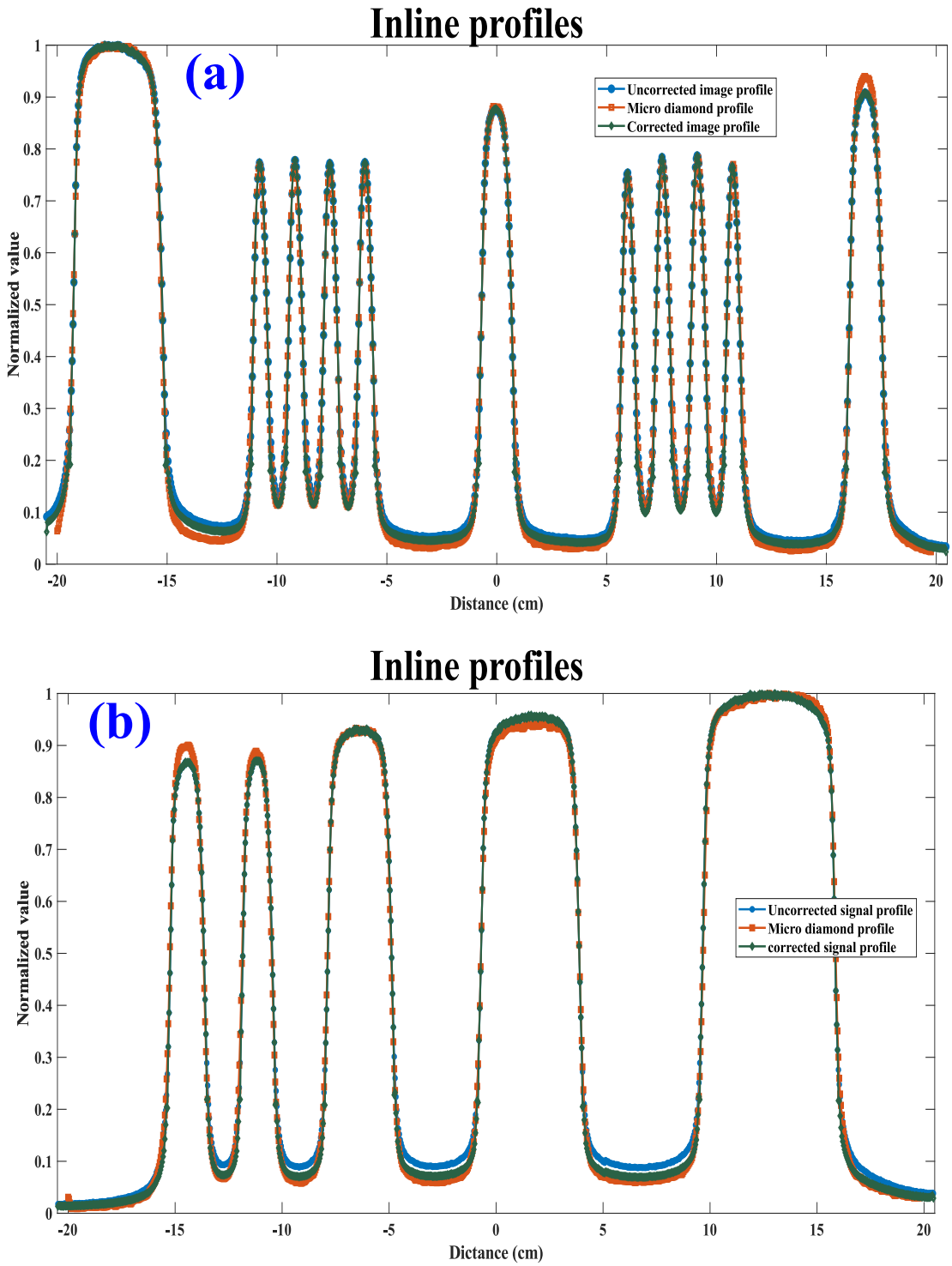

Figure 5.11: In-line profiles measured by micro-diamond and EPID before and after correction of (a) field #1 and (b) field #2.

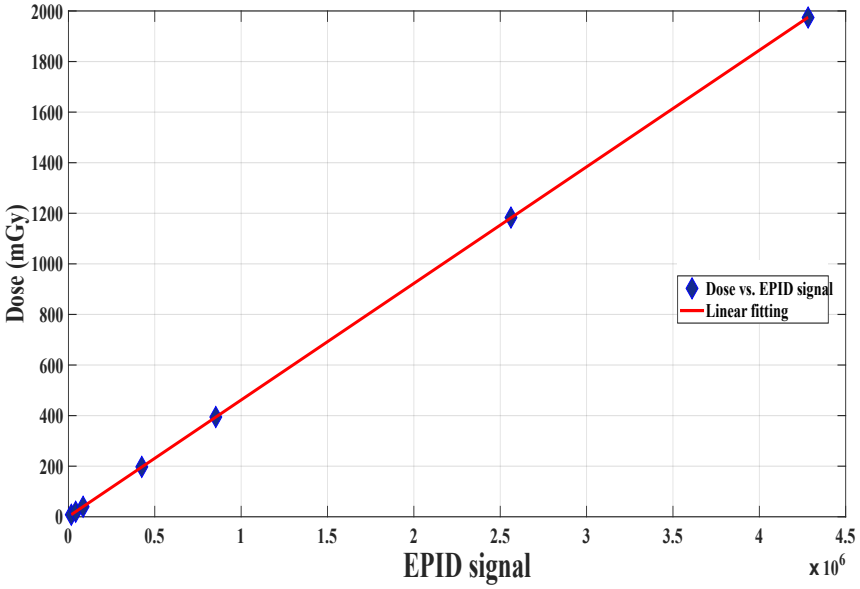

Figure 5.12: Dose vs EPID signal fitting curve.

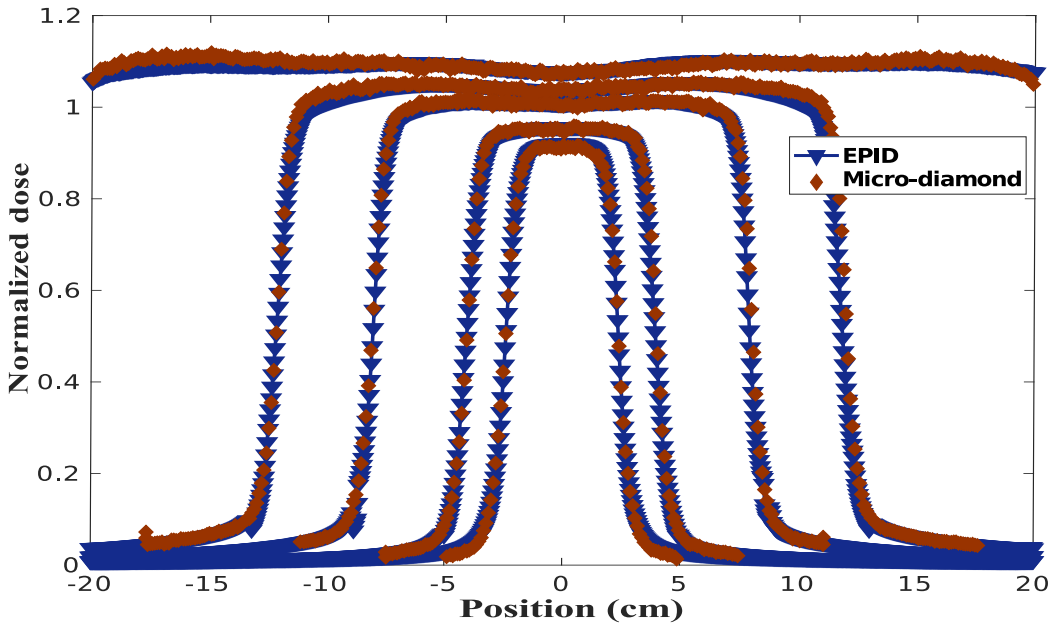

Figure 5.13: Cross-line profiles of square fields of different field sizes normalized to the 10 × 10 cm^2 field as measured by EPID and micro-diamond detector.

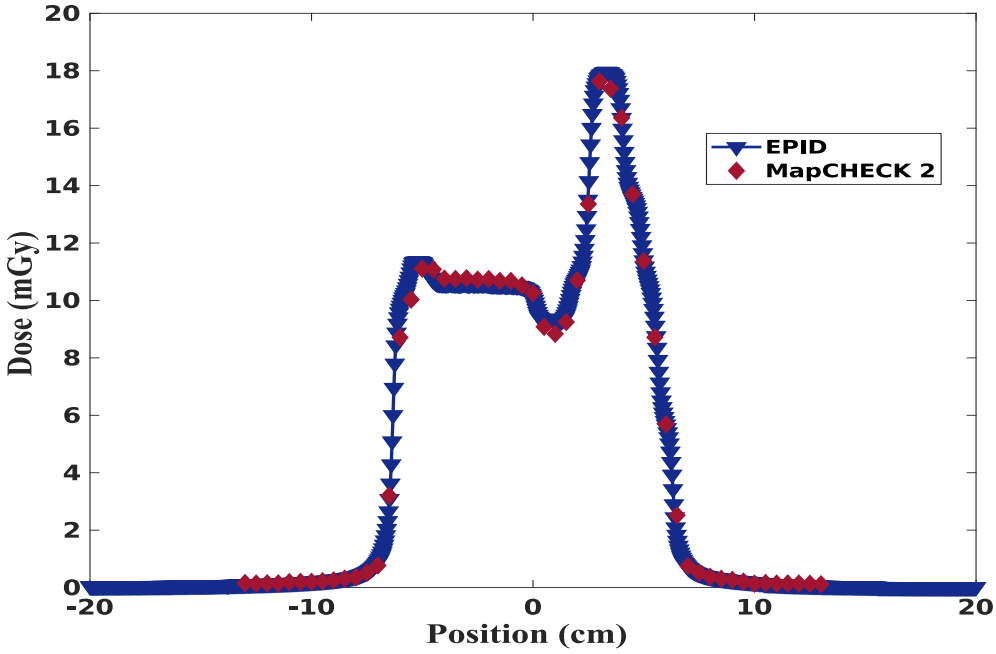

Figure 5.14: Cross-line profiles of step-and-shoot irradiation as measured by EPID and MapCHECK 2 detector.

5.3 Discussion and conclusion

Relying on the dosimetric characterization of the EPID, the primary goal of EPID image frame calibration to 2D dose distribution in water is achieved. Image offset correction is conducted using a conventional method whereas the applied method for dead pixel correction allows to recover many of the pixels marked as dead when using conventional thresholding. The created pixel sensitivity map allows to correct for pixel sensitivity with no dependency on the beam fluence uniformity resulting in a uniform response all over the EPID without compromising the beam characteristics. Thus, the off-axis comparison between EPID measurement and in-water measurement is applicable. The difference between the two off-axis (OARs) ratios after pixel sensitivity correction is solely representing differences between EPID and water media. The generated 2D ROAR relies on the radial interpolation of the mean of the combined in-line and cross-line profiles assuming radial symmetry of the 2D dose distribution. However, the radial symmetry is affected by beam characteristics, which is not perfect due to several factors including target shape, beam focal spot position and collimator (MLC and diaphragm) alignment and shape [146]. Though, the asymmetry is still within the acceptable limits recommended by international committees [147] (i.e. 1%) but adds small uncertainties. The different response as a function of the energy fluence spectra is accounted for in field size correction. The parameters of the kernel are derived based on square fields, and consequently, interpolated for analogous field area making them independent of the field shape. For complex and continuous modulation of the field shapes, the convolution kernel changes

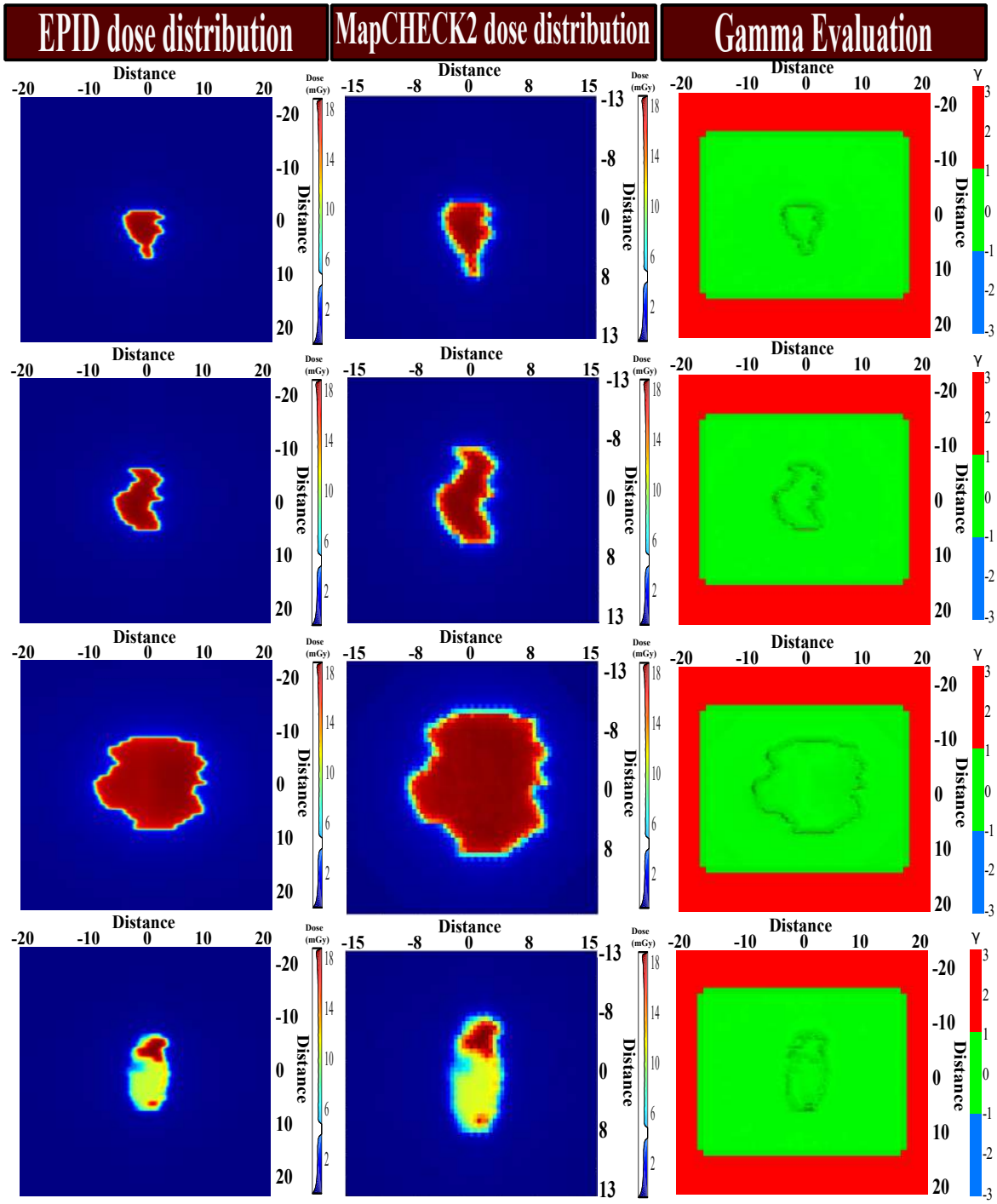

Figure 5.15: Comparison of different fields acquired by EPID and MapCHECK 2 detector.

accordingly. Therefore, image frames are calibrated individually rather than integrally.

Differently, the penumbra correction is based on static kernel which is independent of beam modulation and thus, frame by frame correction is not vital to the calibration model.

General comments
Choosing a dosimeter for reference or validation measurement is challenging. There is no single dosimeter that matches the sensitive area, resolution and potential accuracy of the EPID. Ion chambers are reasonably accurate for large fields but limited for fields smaller than 4×4 cm^2 [148]. Furthermore, ion chambers cannot provide high resolution measurements when used to produce dose profiles due to their relatively large size. Moreover, 1D dosimetry using motorized dosimeter movement requires static field irradiation during scanning. MapCHECK 2 is a 2D array detector based on diodes with a sensitive area equal to 32×26 cm^2 and pixel spacing of 7 mm. When comparing with EPID resolution (0.4 mm^2), MapCHECK 2 detector is inferior and cannot be used as a reference especially for penumbra correction. Film dosimetry is the most suitable option to match EPID resolution, but yet, repeatability and accuracy is found to be not sufficient for referencing. Thus, choice of the dosimeter depends on the aim in each step of calibration and validation. Namely, Farmer ion chamber is used for ROAR and large field measurement due to its reliability and availability. Micro-diamond detector is found to be the best option for small fields and penumbra correction. For comparing complex fields, MapCHECK 2 detector is used to provide a 2D dose distribution adequate for validation.
On a different note, image lag of the EPID system influences the dose per frame, but not the integrated dose. The acquisition of several frames before and after the irradiation releases the burden of modeling the beam-ramp up and the signal fall-off as suggested by other paper [149]. Additionally, the calibration considers low dose irradiation to account for single frame dosimetry.

Finally, the proposed method provides the 2D dose distribution with accuracy comparable to reference dosimeters in a water medium but better spatial resolution and set-up time efficiency. The method is validated for complex and small fields building the basis for validation of clinical dose delivery such as IMRT/VMAT.

Chapter 6

3D dose reconstruction algorithm

6.1 Introduction

EPID-based 2D dosimetry has been described and validated in the previous chapters enabling the comparison with in-water dosimetry. Similar results with different methodologies have also been outlined in the literature by several groups (section 3.1.4.1). In principle, 2D EPID-based dosimetry satisfies the strict requirements of the IMRT QA procedures. Features like high spatial resolution, large sensitive area, real-time measurements and high accuracy make EPID favorite in clinics over conventional dosimeters (e.g. 2D IC array and 2D diode array). Nonetheless, the validation of these methods do not account for gantry rotation. The first generation of dosimeters for 2D verification was designed to be irradiated with IMRT delivery sequence under static gantry condition. Considering the introduction of VMAT, a validation under dynamic gantry condition becomes crucial to determine that the correct dose is delivered at the correct gantry angle. Thus, doses need to be assessed during treatment delivery as a function of time or gantry angle. To this purpose, researchers working on EPID-based dosimetry proposed assessment methods relying on predicting 2D dose distributions per gantry angle and comparing the predicted and measured (calibrated) dose distributions based on control points [79] [150]. Other groups proposed an EPID-based 3D volumetric dosimetry. The EPID image is converted to fluence, back-projected upstream and then imported to a TPS or to a forward dose calculation engine to calculate the dose delivered either to a phantom or directly the patient CT [67] [117] [151]. However, 2D or 3D EPID-based dosimetry approaches rely on dose calculation or image prediction. Hence, accurate dosimetry needs careful modeling of the dynamics of the MLC, the intensity rate modification, gantry rotation and collimator rotation employed by VMAT making the forward dose calculation or image prediction a challenge.

For non-EPID-based dosimetry, commercial devices embedding a 2D detector configuration for 3D volumetric dosimetry have been adopted, such as Octavius® 4D (PTW, Freiburg, Germany), Delta4® (Scandidos AB, Uppsala, Sweden) and ArcCHECK®

(Sun Nuclear Corp., Melbourne, FL). These devices rely on interpolation and extrapolation algorithms to provide a 3D dose distribution to be directly compared to the treatment plan. They are currently widely used in clinics owing to their ability to provide clinical significance to patient-specific pre-treatment dosimetric verification thanks to the DVH analysis, although based on dose interpolation and extrapolation and therefore limited in spatial resolution. Additionally, the usage of these devices has a restriction in setup positioning and timing. Therefore, a fast, simple and accurate 3D volumetric dosimetry, independent of forward dose calculation, is desirable. This chapter presents an EPID-based, prediction-free approach developed to reconstruct a 3D dose distribution as imparted to a virtual cylindrical water phantom to be used for plan-specific pre-treatment dosimetric verification for IMRT and VMAT treatment plans.

6.2 Material and methods

The 3D dose reconstruction required the definition of two virtual water phantoms. A virtual cylindrical water phantom with a diameter and height of 26 cm was placed at the iso-center plane. This phantom was represented by a 256 $\times$ 256 $\times$ 256 matrix in x, y and z directions with isotropic pixel spacing of 1 mm. Another virtual cylindrical water phantom with a diameter and height of 32 cm was created as CT DICOM file and inserted as input to the treatment planning system (TPS) (Monaco® v5.11, ELEKTA Oncology Systems, Crawley, UK) to calculate the 3D dose distribution. For EPID reconstruction, the TPS dose calculation engine used for calibration utilizes the Voxel Monte Carlo algorithm (XVMC) [152] with 1 mm grid size and nominal uncertainty equal to 0.5%. The different dimension between the reconstruction and the calculation was meant to exclude the dosimetric complexity accompanying the build-up region. The main idea of the 3D dose reconstruction is to back-project the planar 2D dose distribution in x and y directions of the EPID image frame upstream at different depths in z direction, thus obtaining the reconstructed 3D dose distribution. For each z, a series of mathematical operations are applied to the back-projected 2D dose distribution to eventually obtain the reconstructed 3D dose distribution by means of summation. These operations are explained in the following.

6.2.1 Geometrical magnification

In back-projection, the planar 2D dose distributions were geometrically demagnified. Since the photon source may be assumed as a point source and the photon beam as divergent [15], the area A_2 at each depth D_2 can be interpolated by knowing the area A_1 at an arbitrary depth D_1 as shown in figure 6.1(a) according to the following equation:

$$A_2 = \frac{(A_1 \times D_2^2)}{D_1^2} \tag{6.1}$$

where A_1 and D_1 are the area and the distance from the beam source to the EPID. To account for geometrical magnification, the back-projected 2D dose distributions were resized to A_2 by interpolation of the EPID image frame as defined by D_2/D_1.

For size validation, a 10×10 cm^2 field was reconstructed, and the 50% positions of the penumbra fall-off of the cross-line and in-line profiles for each level were compared to the reference profiles for the correspondent level.

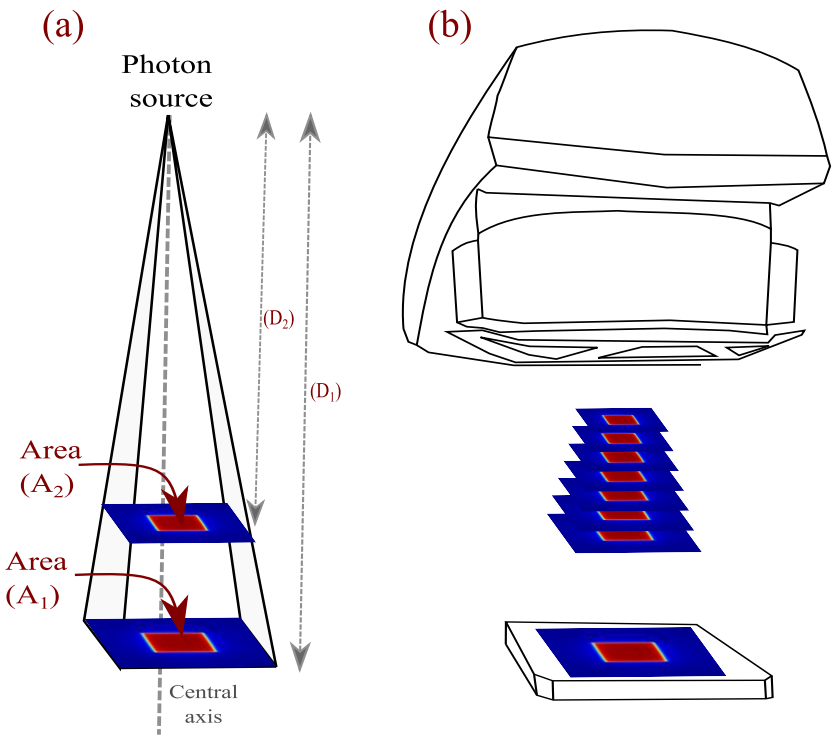

Figure 6.1: (a) Divergent photon beam originated from a point source. (b) Illustration of the image magnification for different levels.

6.2.2 Percentage depth dose (PDD) curve

Series of PDD curves of square fields of 3,5,8,10,15 and 26 cm sides were calculated using the TPS to describe the primary energy deposition, serving as a calibration for the reconstructed 3D dose distributions. For all these curves, second degree exponential fitting was applied, and the fitting parameters were extracted to obtain the PDD curve (after the build-up region) for any field size or field area. The obtained PDD was then multiplied by the corresponding back-projected distribution, as resulting from the previous operation.

6.2.3 Depth specific off-axis ratio

Due to the cylindrical shape of the virtual phantom, the off-axis energy deposition relative to the central axis is described by a depth specific off-axis ratio. A dose distribution with square field side of 26 cm (corresponding to 41 cm at EPID level) was calculated using the TPS. The same field was used to irradiate the EPID and both the simulated and the reconstructed 3D dose distributions at each depth were normalized to the central dose. The division between both matrices produced the depth specific off-axis ratio, which was multiplied to the result of the previous operations.

6.2.4 Depth specific lateral scatter kernel

Square fields of 3, 5, 8, 10, 15 and 26 cm sides were generated using the TPS to describe the lateral scatter kernel for each depth z and each field size to define the reference 2D dose distributions. The in-line and the cross-line profiles were then compared to the corresponding profiles in the back projected 2D dose distributions. The difference between the two distributions represented the lateral energy deposition. This scattering effect was handled in a similar fashion as partial volume effect in imaging [153] [154]. An iterative optimization algorithm was developed to find size and shape of convolution kernels describing this lateral energy deposition. The two 2D dose distributions were segmented into a hot region (pixels with values above 15% of the reference maximum dose) and a cold region (pixels with values lower than 15% of the reference maximum dose). The iterative optimization algorithm led to two convolution kernels expressed by a radially symmetric Lorentz fitting function with 4 coefficients. The coefficients for each depth and field size used for comparison were saved in a look-up table. The iterative optimization procedure is schematically illustrated in figure 6.2 and the code implementation is described in appendix (A). For image frame reconstruction, the field size determined in section 5.1.5 was used to call the coefficients for each depth and nearest field size. The same segmentation in hot and cold region was applied to the 2D dose distribution. The correction was therefore implemented as a separated convolution and a subsequent merging of the two regions to reproduce the reference 2D dose distribution.

6.2.5 Rotation

Time labeling of EPID image frames and gantry angle The reconstructed 3D dose distributions required to be rotated along the in-line direction in accordance with the gantry angle during irradiation. For IMRT technique, the gantry angle had discrete values for each beam. On the other hand, the continuous irradiation of the VMAT was matched with a continuous variation of the gantry angle and the rotation speed as well. Therefore, an accurate time labeling of the image frames was required. However, Elekta's EPID does not embed this information in the file header. Thus, the gantry angles were extracted from the log file of the linac trajectory, that saves the gantry angle and the time label in the

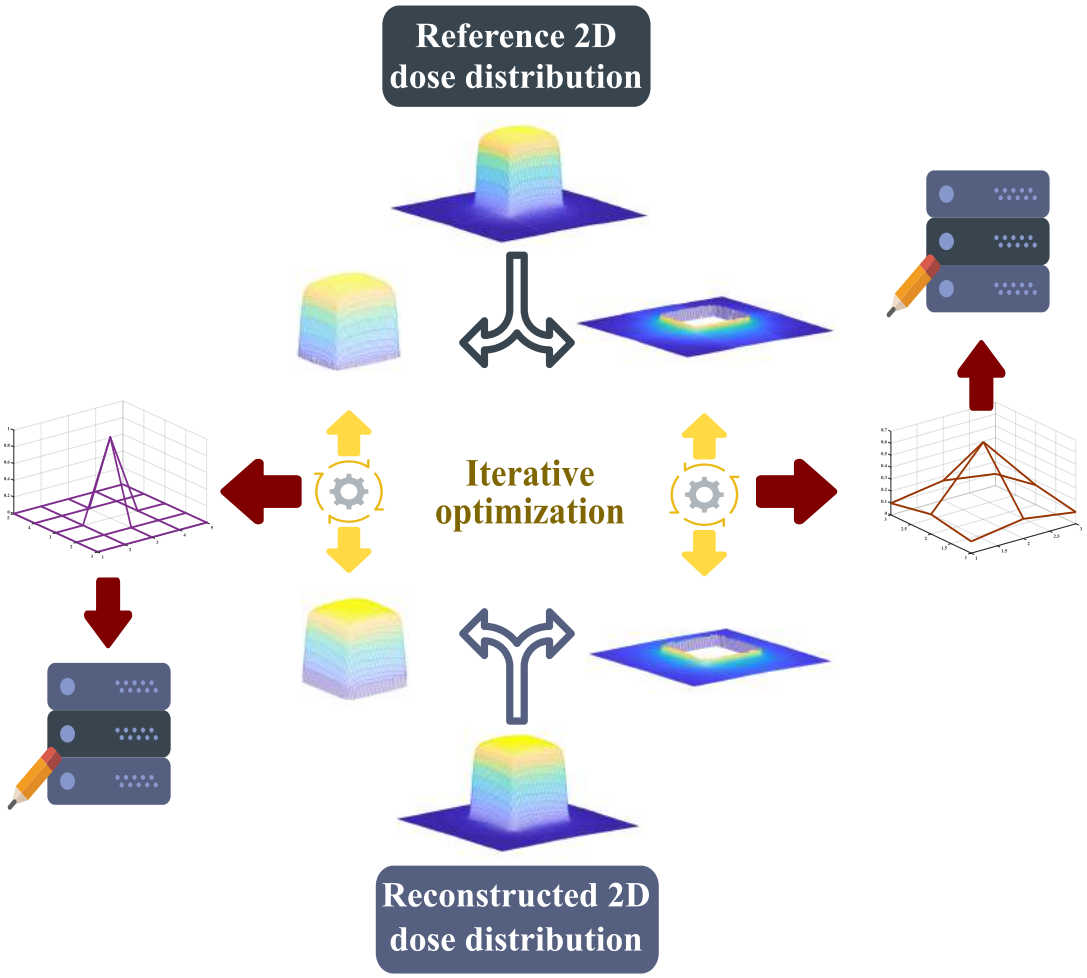

Figure 6.2: Schematic illustration of the iterative optimization procedure for a selected depth and field size. Firstly, the two 2D distributions are segmented to hot and cold regions. Secondly, an iterative optimization is applied to find the best convolution kernel needed to generate the reference 2D dose distribution out of the back-projected 2D dose distribution. The resulted kernels are saved in a look-up table.

Unix timestamp format with a time resolution up to 0.25 s. As the EPID also saves the Unix timestamp format, EPID image frames were synchronized and labeled with nearest neighbor (preceding) gantry angle.

Correction for gravitational displacement of the EPID During the gantry rotation, gravitational force is applied to the EPID causing a mechanical displacement in the cross-line (x) direction. To assess the magnitude of that displacement, 10×10 cm^2 square fields were acquired for the 360 rotational degrees in intervals of 10 degrees each [155]. By considering the central cross-line profile at gantry angle 0 degree as a reference, the position difference of the 50% penumbra fall-off between the reference and the comparing profiles were recorded. The gantry shift was reported as a function of the gantry angle. The shifts were fitted as a function of gantry angle using the following formula:

$$displacement = a_1 \exp^{(-((theta-a_2)/a_3)^2)} \tag{6.2}$$

where θ is the gantry angle and (a_1, a_2, a_3) represents the amplitude, the position and the width of the fitting function, respectively. After converting the distance to pixel, the nearest integer to the obtained displacement was used to shift the EPID image frame prior to 3D dose reconstruction.

The overall steps involved in calibration and reconstruction process are outlined in figure 6.3.

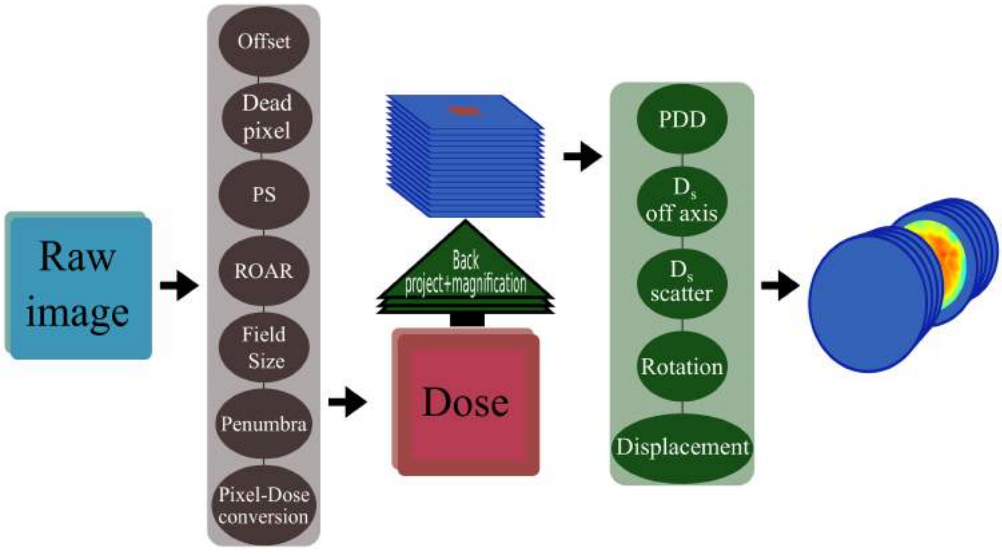

Figure 6.3: A flowchart of calibration and reconstruction process. The procedure first converts the acquired raw image frames into a 2D dose distribution. Secondly, the 2D dose distribution is back-projected upstream at several depths, hence, depth specific (Ds). The back-projected 2D dose distribution undergoes several mathematical operations to produce a 3D dose distribution in a cylindrical water phantom. The whole process is repeated for each image frame.

6.2.6 Validation and data analysis

The 3D dose reconstruction was validated with respect to measurements based on Octavius (see 6.4a). Square fields from 3×3 cm^2 up to 26×26 cm^2 and several step-and-shoot irradiations were considered. For initial validation of clinical treatment plans, one IMRT and one VMAT were considered and the 3D dose reconstructions of the treatment plans were validated against the 3D dose distribution measured and calculated by Octavius. Due to the low spatial resolution of the dose distribution from Octavius (2.5 mm) with respect to the 3D dose reconstruction (1 mm), the 3D dose calculation performed by the TPS at the desired spatial resolution was also considered. Besides, the TPS calculation is not affected by the daily setup uncertainties as the measurements. Hence, data analysis considered the TPS as the reference. Furthermore, five IMRT (two head & neck, two prostate and one scalp cases) and five VMAT (head & neck, cervix, brain, pelvis and abdomen plans) were validated as imparted to a virtual water phantom and the 3D dose reconstructions were compared to the 3D dose calculation performed by the TPS in water phantom using the same calculation engine used for calibration but with grid size equal to 2.5 mm to mimic the QA routine conducted in the clinic.

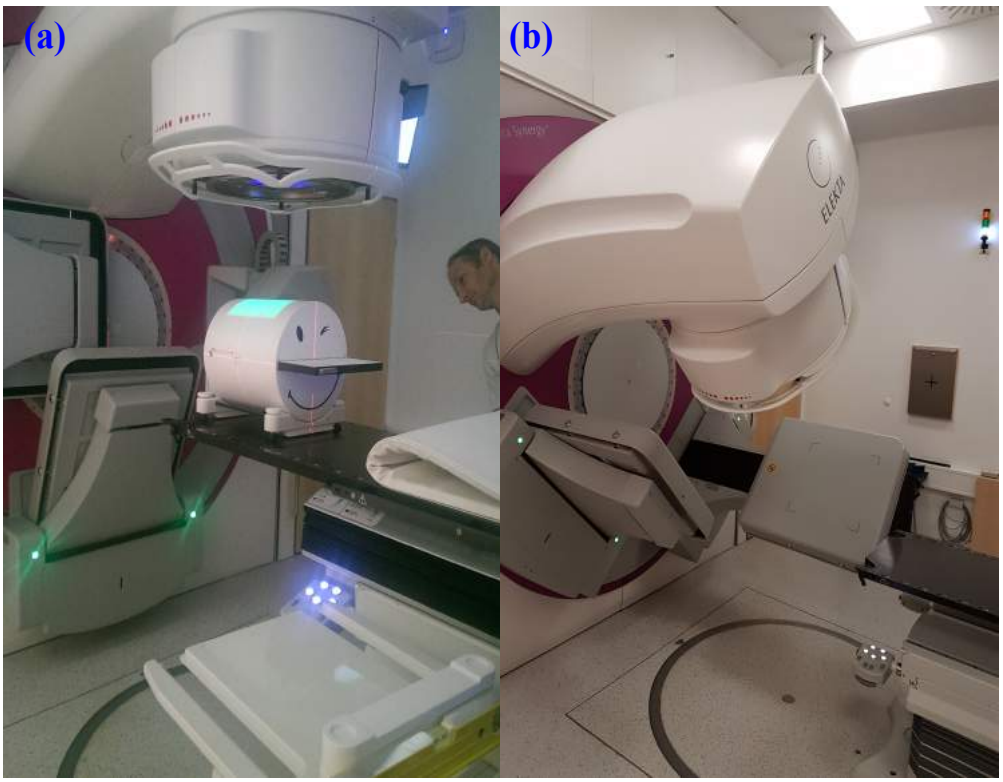

Figure 6.4: Picture of (a) Octavius setup (b) In-air image acquisition of EPID during a plan delivery.

Table 6.1: Optimization algorithm for the 4 coefficients of the Lorentz fitting function y(x) = a/((x - b)^2 + c) +d, where x represents the radial coordinate of the kernel in pixels.

Field size (cm^2) (No. of irradiated pixels)	Depth (cm)	Region	a	b	c	d	Kernel size (pixels)	Sum of squared difference (Gy)
2 2 [5865]	5	Hot	2.76	5.00	4.99	5.00	(3,3)	0.18
		Cold	0.07	0.00	-2.86	2.98	(5,5)	0.08
5 5 [38772]	13	Hot	0.07	5.00	3.75	4.50	(5,5)	0.19
		Cold	-0.04	2.63	-5.00	-5.45	(5,5)	0.30
15 15 [359099]	25	Hot	0.01	2.31	4.14	4.33	(11,11)	0.82
		Cold	0.21	0.00	2.50	-2.22	(3,3)	0.28

6.3 Results

6.3.1 Validation of PDD curves

Figure 6.5 shows the comparison between the PDD curves obtained from the reconstructed 3D dose distributions and the reference 3D dose distributions from TPS calculation for different square fields irradiated with 100 MU. The curves highlight the 6 cm difference in diameter between the virtual phantom used for 3D dose reconstruction and the one used for the TPS calculation. The 2D gamma evaluation between the corresponding 3D dose distributions using (3%, 3 mm) criteria resulted in 100% passing rate. In here, the gamma evaluator was allowed to search circularly (not spherically) in cross-line (x) and in-line (y) directions for each depth (z). The gamma index profiles along the z coordinate are plotted in the lower panels of figure 6.5.

6.3.2 Validation of depth specific lateral scatter kernel

The central cross-line dose profiles comparing the reconstructed 3D dose distributions and the reference 3D dose distribution from TPS calculation for square field sides of 2, 5, 10, 15 and 26 cm are shown in figure 6.6. The gamma evaluation between the corresponding 3D dose distributions using (3%, 3 mm) criteria resulted in 100% passing rate. Similar to the 2D gamma evaluation conducted in section 6.3.1, the cross-line gamma index profiles are plotted in the lower panels of figure 6.6. The penumbra of the profiles demonstrates the accuracy of the optimization algorithm. Table 6.1 shows the results of the optimization algorithm for the 4 coefficients of the Lorentz fitting function for selected field sizes and depths, distinguished in hot and cold regions. Figure 6.7 shows an example of a reconstructed 3D dose distribution of 5×5 cm^2 field, compared to 3D distribution calculated using TPS.

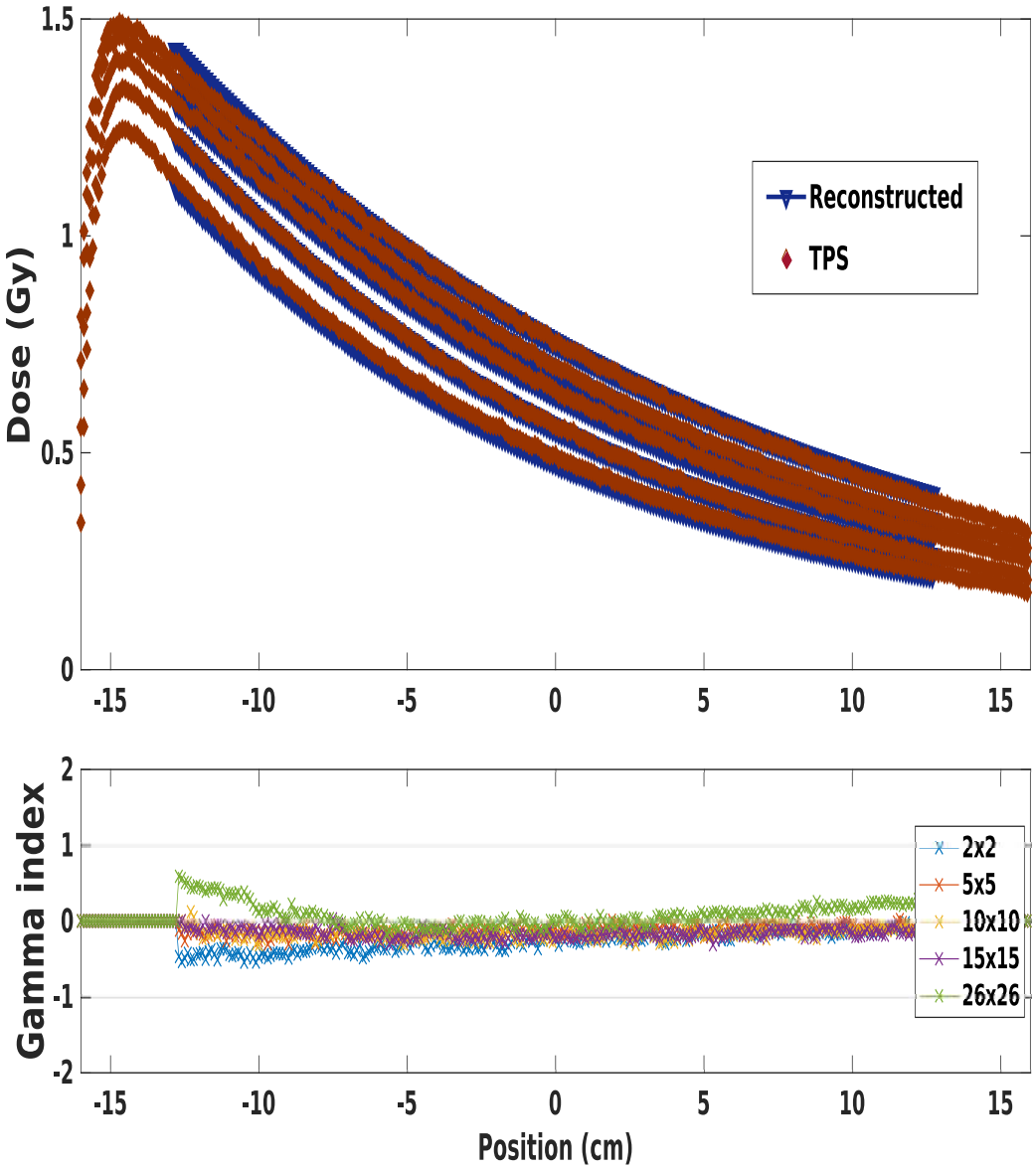

Figure 6.5: PDD curves of different square fields as obtained from the reconstructed 3D dose distributions and the reference 3D dose distribution from TPS calculation annotated with scatter plot of the gamma index resulted from evaluation between each corresponding profiles.

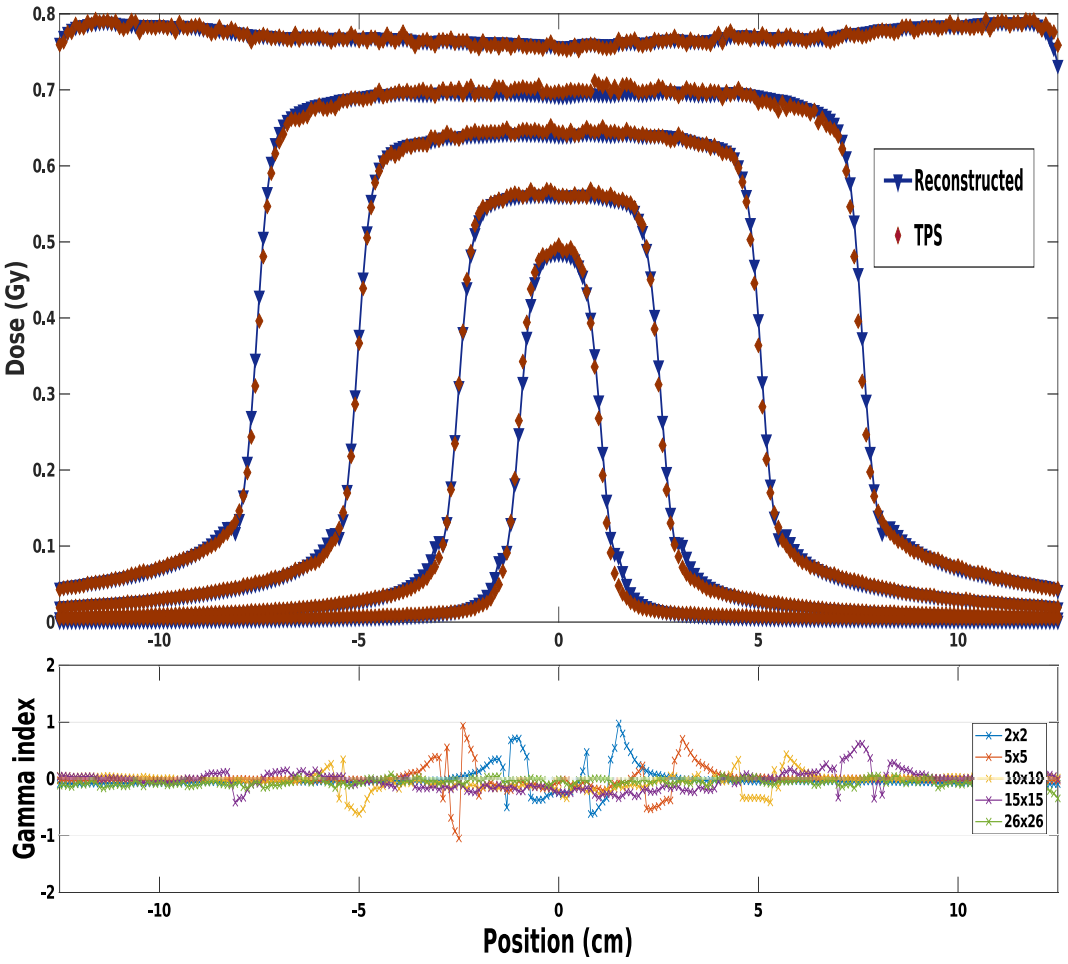

Figure 6.6: Central cross-line profiles at the iso-center of square fields of different field sizes as obtained from the reconstructed 3D dose distributions and the reference 3D dose distribution from TPS calculation annotated with scatter plot of the gamma index resulted from evaluation between each corresponding profiles

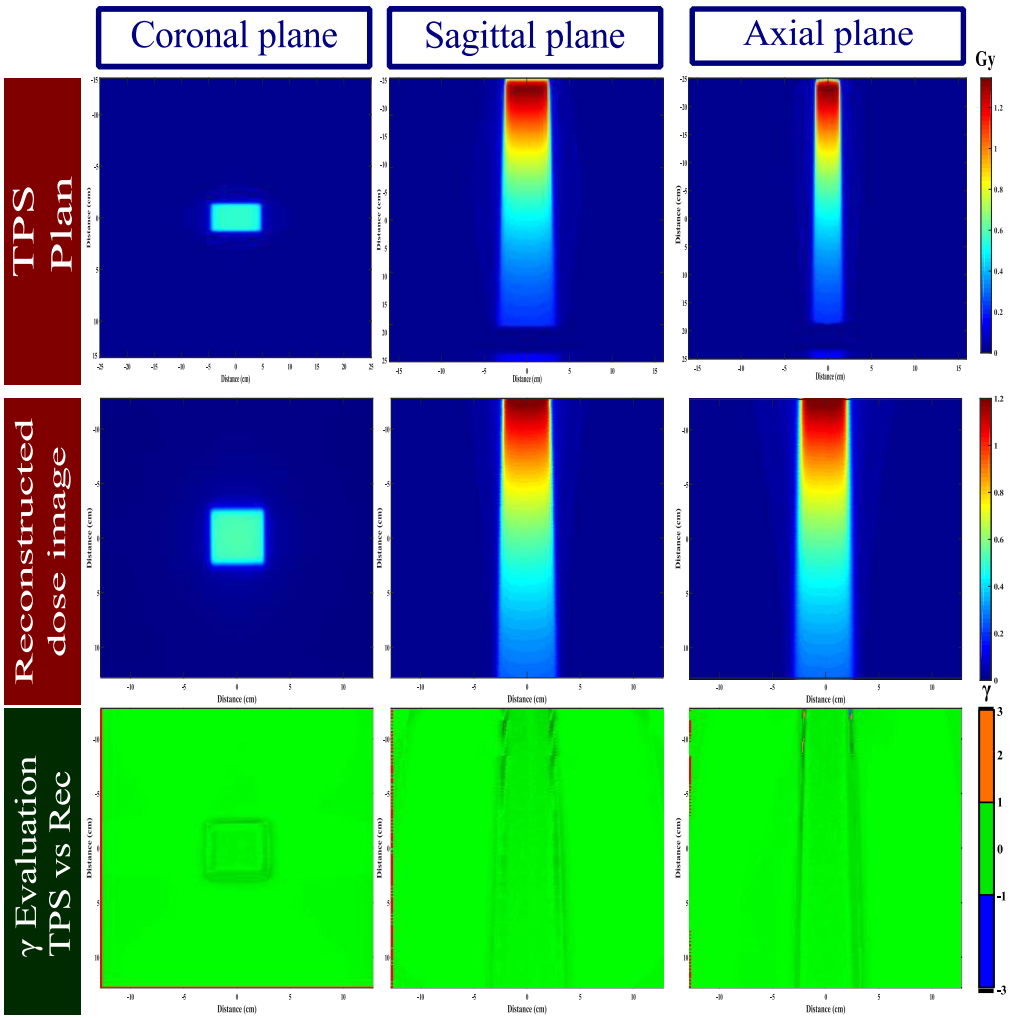

Figure 6.7: Different views of 3D dose distributions of 5×5 cm^2 field calculated using TPS and reconstructed from EPID image frames followed by gamma comparison between the two distributions.

6.3.3 Time labeling of EPID image frames and gantry angles combined with correction for gravitational displacement of the EPID

The time labeling of EPID image frames and gantry angles enables the integration of reconstructed 3D dose distributions as a function of time and gantry angle. Figure 6.8 shows an example of recorded messages plotted against acquisition time obtained from the EPID header file and linac log file.

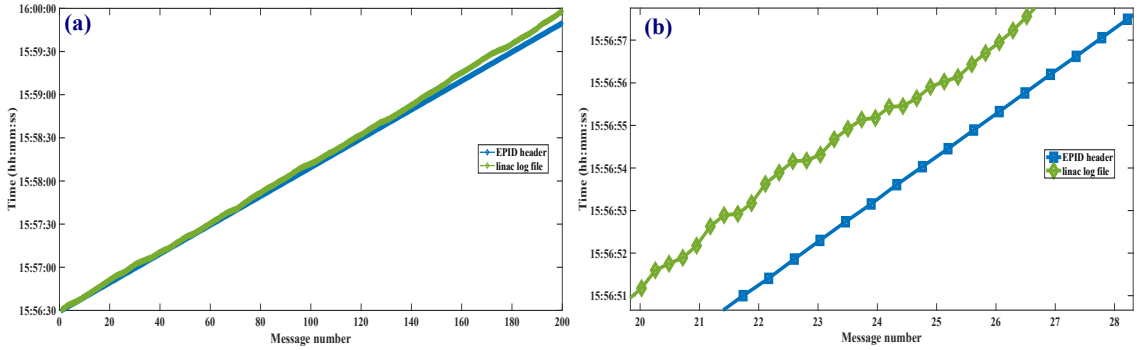

Figure 6.8: (a) Linac log file and EPID header file messaging time labels recorded during a VMAT delivery. (b) Zoomed of the time labels of (a).

For gravitational displacement correction, figure 6.9 shows the recorded EPID gravitational displacements along the cross-line direction per angle in 10 degree steps. The fitting parameters are: a_1= 10.3, a_2= 181.4 and a_3= 102.6 resulting in residual R^2 value equal to 0.99.

To test the labeling correctness, two separated rectangular shaped fields is created and planned for continuous irradiation during the 360° rotation of the linac gantry resulting in torus shape 3D dose distribution. The reconstructed image frames were rotated utilizing the gantry information extracted from the linac log file. Figure 6.10 shows that the integrated distributions compared with Octavius measurement using gamma evaluation with (3%, 3 mm) criteria resulted in $\approx$ 96% passing rate.

Figure 6.11 shows an example of reconstructed 3D dose distributions integrated over time, acquired during a cervix treatment plan for QA delivery purposes.

6.3.4 Validation and verification of clinical treatment plans

6.3.4.1 Validation

Figures 6.12 and 6.13 show different views of the reconstructed 3D dose distributions in comparison to those produced by Octavius and the TPS for prostate IMRT and head and

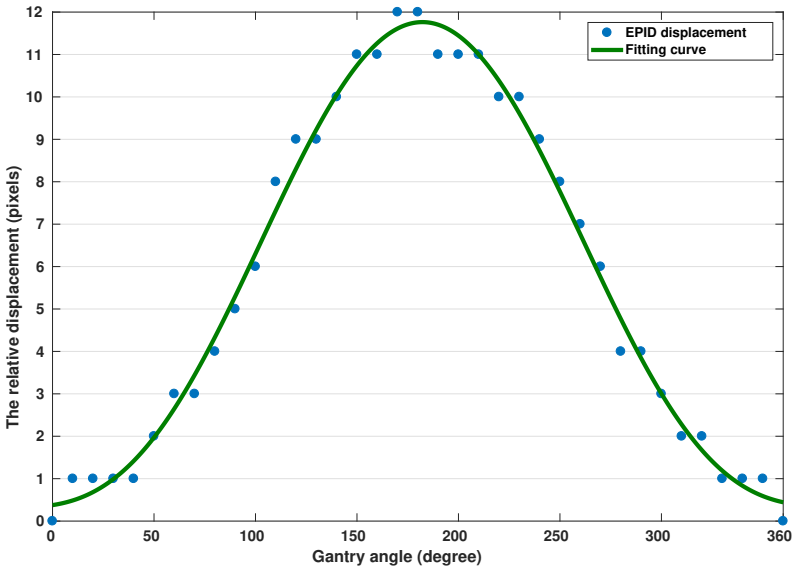

Figure 6.9: Detected and fitted cross-line shifts of the EPID as a function of the gantry angle.

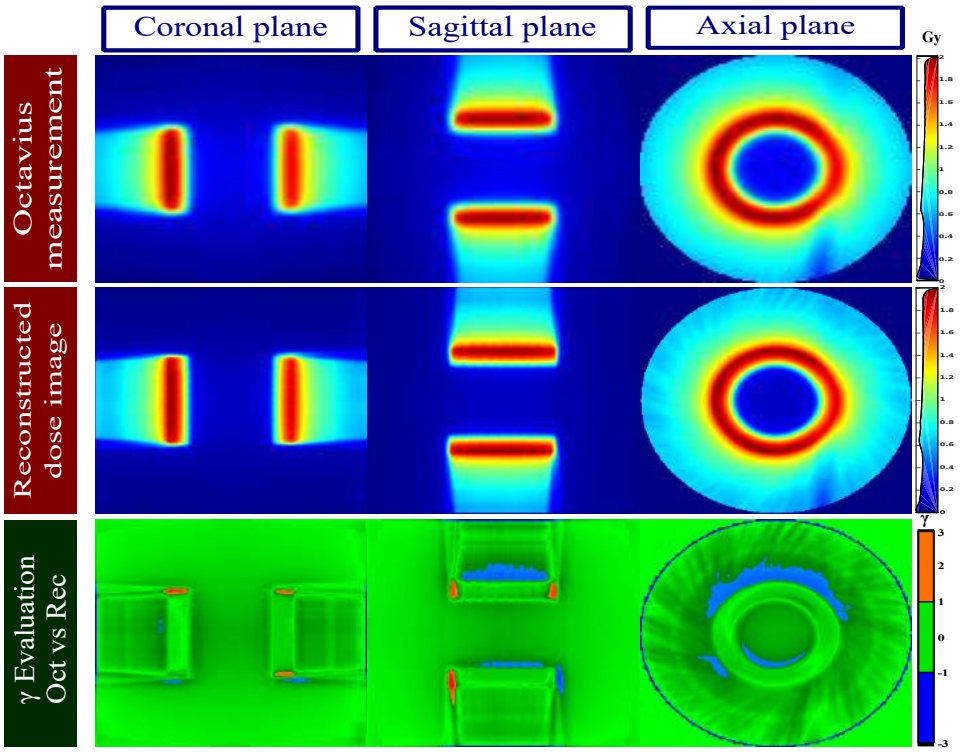

Figure 6.10: A torus shaped field measured by Octavius and reconstructed from EPID image frames followed by gamma comparison between the two 3D dose distributions.

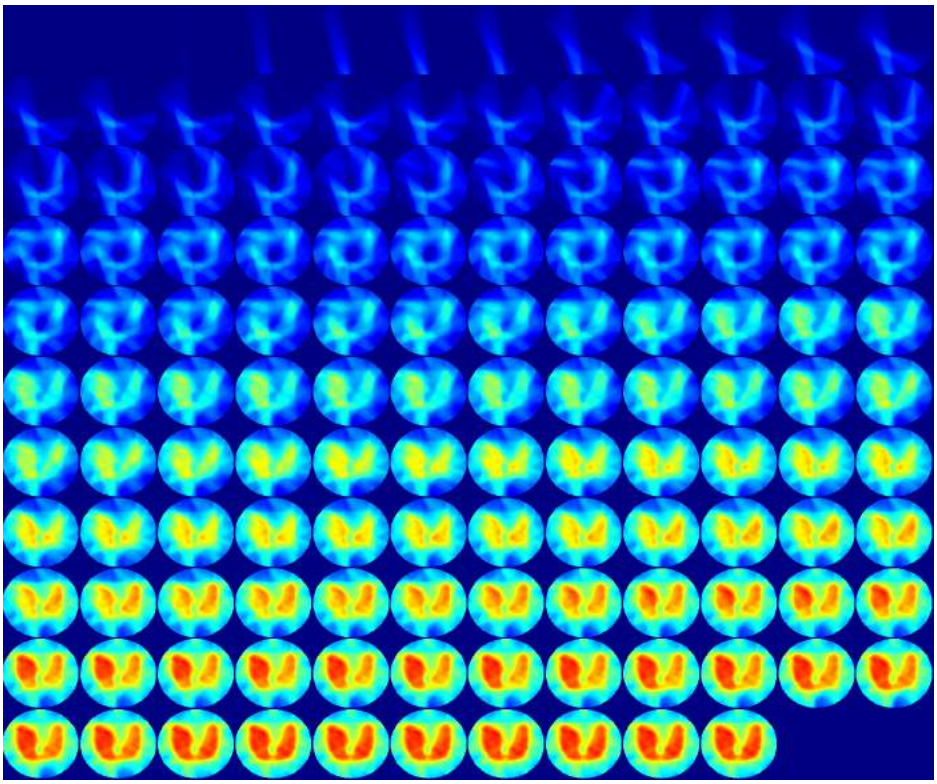

Figure 6.11: Axial views of reconstructed 3D dose distributions integrated over time during QA procedure of VMAT cervix treatment plan. The distribution sequence was resolved in 0.57 fps for illustrating purposes.

Table 6.2: Passing rates of the global gamma evaluation with (3%, 3mm) criteria for different IMRT and VMAT plans between the reconstructed 3D dose distribution and the TPS calculation

IMRT Plan	passing rate	VMAT Plan	passing rate
Head & neck (case #1)	99%	Head & neck	95%
Head & neck (case #2)	99%	Cervix	95%
Prostate (case #1)	99%	Brain	99%
Prostate (case #2)	98%	Pelvis	96%
Scalp	97%	Abdomen	96%

neck VMAT plan, respectively. The global gamma evaluation with (3%, 3 mm) criteria, applied between the reconstructed 3D dose distribution and both Octavius measurement and TPS calculation, is shown in the figures for both treatment plans. The recorded passing rates were 99% and 95% for the IMRT, and 96% and 93% for the VMAT plan, considering TPS calculation and Octavius measurement, respectively.

6.3.4.2 Verification of different IMRT and VMAT plans

Table 6.2 shows the result of the global gamma evaluation with (3%, 3 mm) criteria between the reconstructed 3D dose distributions and the TPS calculations for five IMRT plans and five VMAT plans. The median passing rates recorded for the 10 plans was 97% and the lowest rate recorded was 95% for head & neck and cervix VMAT treatment plans.

6.4 Discussion and conclusion

The goal of this chapter is to reconstruct a 3D dose distribution as back-projected from the 2D dose distribution in water obtained from EPID image. The method was developed as an inverse problem solving, making use of step by step optimization algorithms relying on the physics behind each step. As inverse problem, each optimization algorithm searches pararmeters that enable a certain model to match the observation (i.e. the reference measurement). Hence, solving the inverse problem requires a reliable reference. In clinics, obtaining a 3D distribution of dose in a cylindrical water phantom with high accuracy and good resolution is challenging. A trade-off between accuracy, spatial resolution and 3D distributions has to be considered to reach the optimum solution for QA proposes. The Octavius was the best available option to provide a reference measurement. In addition to its relatively poor resolution, Octavius measurements failed to give 100% passing rate when comparing with TPS calculations for IMRT and VMAT plans using gamma evaluation. Thus, referencing Octavius leads to additional deviations from TPS calculations. Accordingly, the 3D dose distribution generated by the TPS was considered to be the reference for the proposed calibration. However, details on the specific discussions and

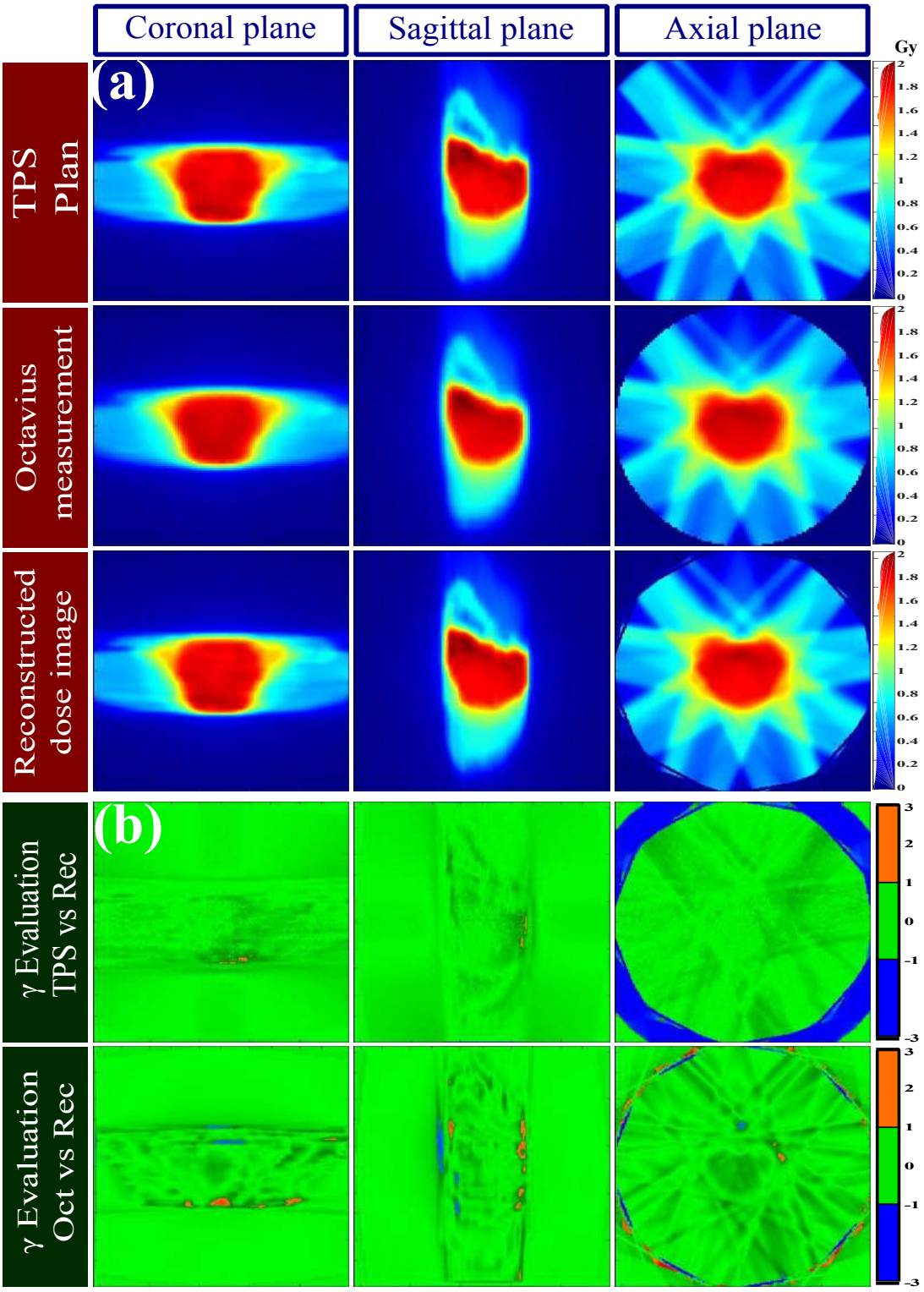

Figure 6.12: (a) Coronal, sagittal and axial views of 3D dose distributions of prostate (case #1) IMRT calculated by the TPS, measured by Octavius (Oct) and reconstructed (Rec) from EPID. (b) Different views of 3D gamma evaluation between the 3D dose distributions of the TPS calculation and reconstructed from EPID and between the 3D dose distributions of the Octavius measurement and reconstructed from EPID.

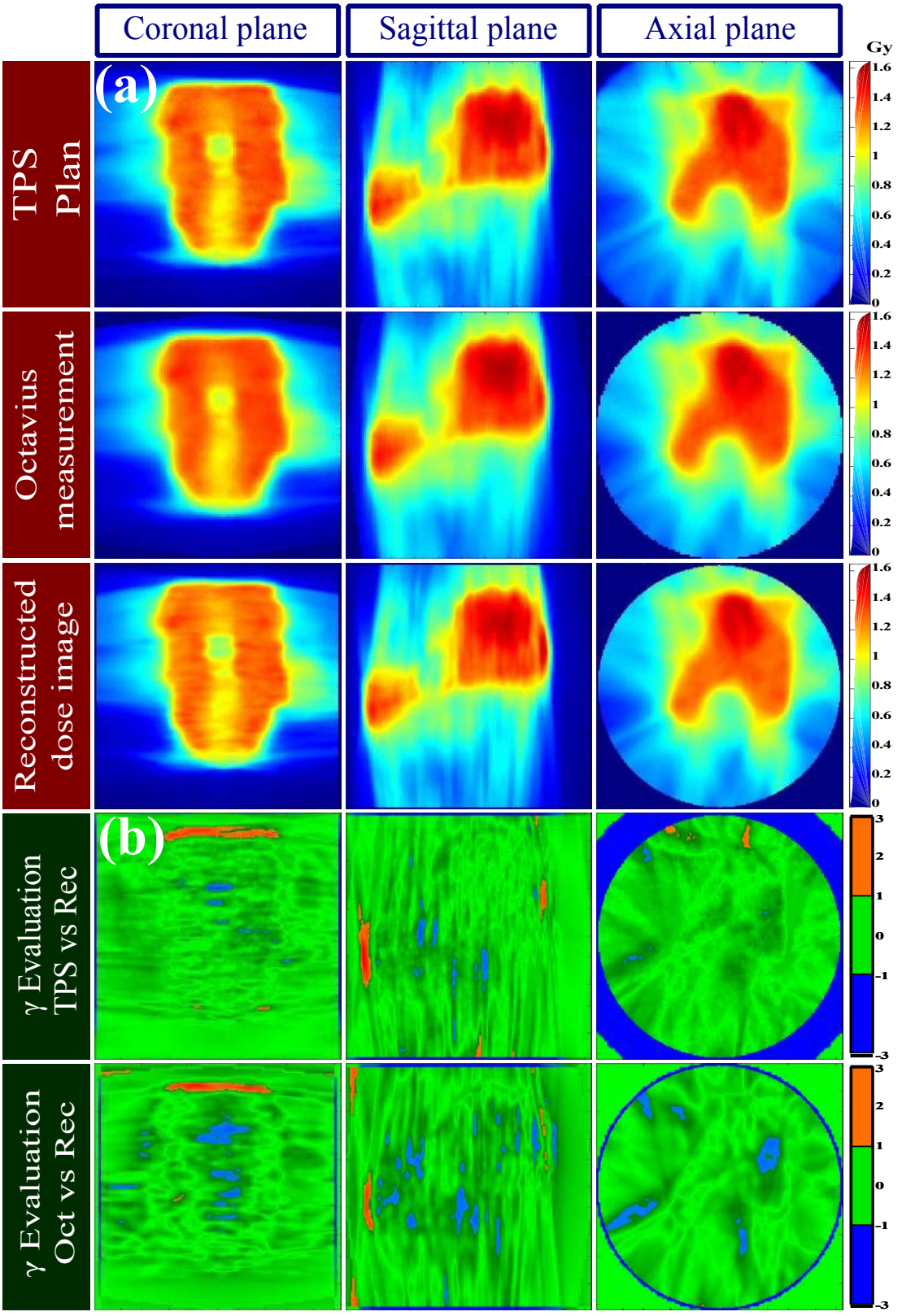

Figure 6.13: (a) Coronal, sagittal and axial views of 3D dose distributions of head and neck VMAT calculated by the TPS, measured by Octavius (Oct) and reconstructed (Rec) from EPID. (b) Different views of 3D gamma evaluation between the 3D dose distributions of the TPS calculation and reconstructed from EPID and between the 3D dose distributions of the Octavius measurement and reconstructed from EPID.

assumption that were made for each step are outlined below.

6.4.1 Geometric magnification

Geometric magnification determines the resizing factor for each depth resulting in 2D image pixel sizes of odd or even numbers. When back-projecting, the resized smaller image was aligned to the center of the previous image. The difference between the two image sizes at the edges was filled with zeros. As the difference could be odd or even, a shift of one pixel in either x or y directions was required. The correct shift direction was decided upon the reference penumbra position. When comparing, the 50% positions for some levels located between two pixels. The shift direction considered the nearest position was yielding a sub-millimeter shift from the correct position. The shifting effect appeared in low depth levels (away from EPID) where interpolation is highest and data were missing due to the decrease in resolution as shown in figure 6.7. Optimizing the geometric magnification is feasible by increasing the spatial resolution of the reference 3D images and interpolate the value at the desired pixel position. An attempt towards the improvement of geometric magnification was implemented. Particularly, the spatial resolution of the 3D image was increased to accommodate the smallest resizing. However, the additional computational resources required by that, including computation time, could not justify the negligible improvement of the outcome.

6.4.2 PDD curves and lateral dose profile

The comparison between the reconstructed 3D distributions and reference distributions resulted in $\approx$ 100% passing rate using gamma evaluation. However, a less than 0.5% deviation was noticed at the phantom edges due to the deviation in fitting functions used for reconstruction. Nonetheless, Despite testing different fitting functions in an effort to improve the results, similar residual R^2 values were obtained.

For the lateral dose deposition, the optimization algorithm generates kernels that produce dose distributions comparable to the reference. When comparing lateral profiles, gamma index showed $\approx$ 100% passing rate (figure 6.6). Though, the effect of hot- and cold-image recombination appears at the 15% dose level for each field. Smoothing the fall-off pattern can be performed but requires additional interpolation with no significant impact on the comparison.

6.4.3 Time labeling efficiency and the correction for gravitational displacement

Figure 6.8 shows recorded messaging time generated by the linac control system and EPID acquisition system with millisecond resolution. The not perfect linearity noticed in

messaging times of linac trajectory in addition to the offset in clock synchronization have negligible impact on time labeling especially when rounding the temporal resolution to hundreds of millisecond required for our proposes.

With default gantry rotational speed in VMAT delivery of about 1 degree per second and around 2.5 messages per second, the uncertainty of frame labelling is around ± 0.4 degree in comparison to ± 1.5 degree for Octavius [156]. The difference between the labeling accuracy was noticed in torus field test (figure 6.10). In addition to the effect on matrix rotation, labeling image frames with gantry angles enable correcting for the gravitational displacement of the EPID which was found to be up to 4 mm. The correction has a positive impact on gamma evaluation when using static gantry irradiation (IMRT) and continuous irradiation (VMAT).

6.4.4 Validation

For validation of clinical plans, gamma evaluation with (3%, 3 mm) criteria was used due to its ability to detect various dosimetric deviations [61]. The comparison was conducted against detector measurement and dose calculation. As the accuracy of the reference measurement affects the evaluation of the obtained results, the 3D dose reconstruction considered the 3D dose distribution from TPS calculation as a reference due to its achievable spatial resolution. However, since the calibration relied on TPS calculations, the discrepancies noted in the gamma evaluation (figure 6.12(b) and 6.13(b)) between Octavius and the 3D dose reconstruction were expected [157]. The evaluation for the different IMRT and VMAT plans in table 6.2 showed a passing rate exceeding the common tolerance level (i.e. 95%) [158] for the selected treatment plans.

Finally, as mentioned earlier, the 3D dose reconstruction relied on inverse problem solving. Each step contributes to the overall accuracy as well as to the overall acquisition time of the proposed methodology. For instance, EPID is characterized by a dose rate dependency which affects the accuracy of the reconstructed 3D dose distribution of VMAT treatment plans. In this study, no dose rate dependency corrections are performed. The maximum deviation of the cumulative dose detected by EPID with respect to ion chamber measurements is estimated to be $\approx 1.5\%$. A correction for dose rate dependency is expected to improve results in terms of gamma evaluation, reaching passing rates comparable to IMRT treatment plans. However, it extends the calibration time and requires additional information from the linac log file.

Chapter 7

Sensitivity analysis of EPID-based 3D dose reconstruction

7.1 Introduction

The proposed method has been validated for dosimetric accuracy for complex clinical plans. However, the rationale of this thesis is to establish a sensitive tool for plan-specific dose delivery QA. In general, the sensitivity of such tool quality is evaluated by its merits to catch errors before the dose delivery. Through the radiation therapy chain, dose delivery is vulnerable to several types of errors especially with the introduction of complex treatment techniques. IMRT and VMAT, for example, exploit various mechanical and dosimetric degrees of freedom making the precise interplay and coordination of each parameter essential for correct dose delivery. Hence, current technology offers numerous error sources. The goal of this chapter is to investigate the sensitivity of an EPID-based 3D dose reconstruction algorithm to detect geometric and dosimetric errors in VMAT plans.

7.2 Material and methods

A typical VMAT plan for head & neck case was generated using the TPS (Monaco® v5.11, ELEKTA Oncology Systems, Crawley, UK). The plan was delivered using the linac and the image frames were acquired during delivery using the calibrated EPID. The acquired frame images were reconstructed to a 3D dose distribution with 1 mm isotropic resolution using the developed algorithm from chapter 6. The resulted distribution was evaluated against the TPS dose distribution in a cylindrical water phantom. In parallel, intentional dosimetric and geometric errors were introduced in the original treatment plan.

For geometric sensitivity testing, firstly, two selected neighboring leaves were shifted

by 2 mm in all control points of the original treatment plan file. Secondly, a 1 degree controlled rotational shift of the gantry angles was applied. For dosimetric sensitivity testing, the total monitor units of the original plans were increased by 4%.

The resulting 3D dose distributions were compared to the original plan using global gamma evaluation with (3%, 3 mm) as acceptance criteria.

7.3 Results

Figure 7.1 shows different views at the iso-center of the original head & neck case delivered to a virtual cylindrical phantom as calculated by the TPS and reconstructed from the EPID image frames. The gamma evaluation between the two distributions resulted in 98.81% passing rate.

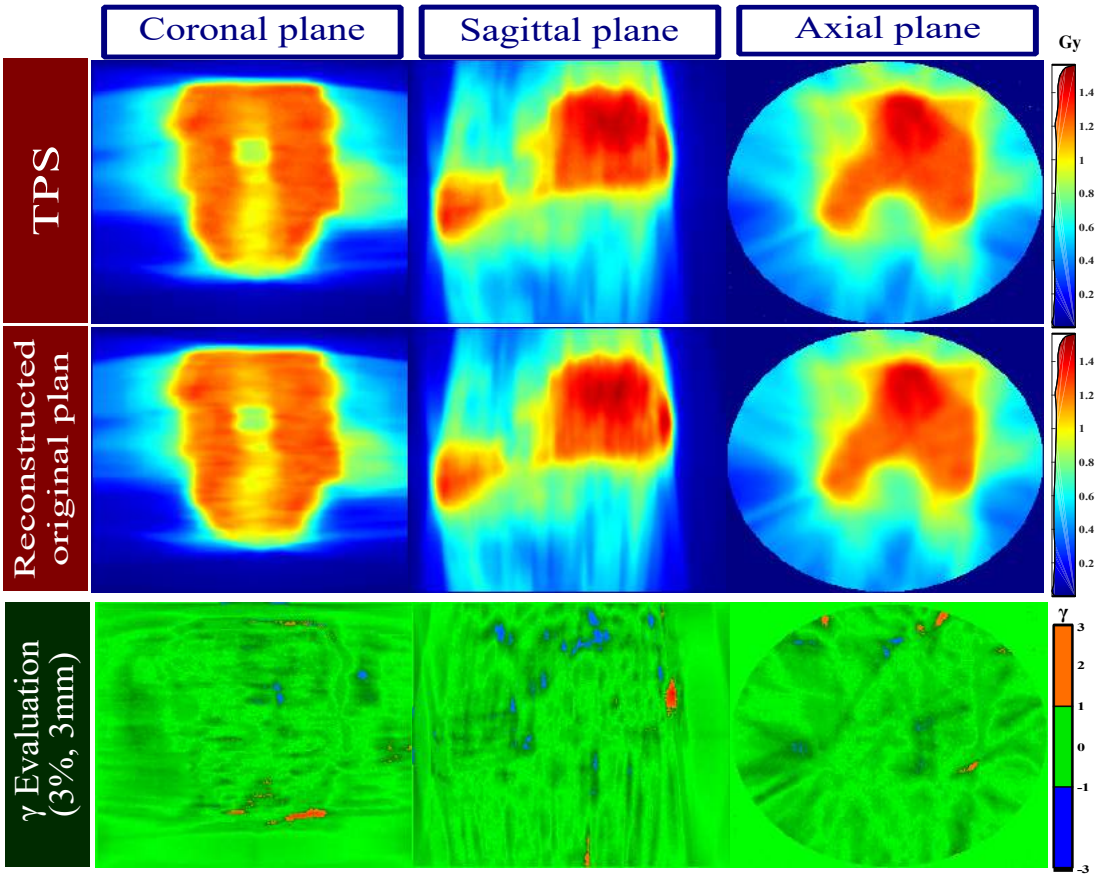

Figure 7.1: Coronal, sagittal and axial views of the original 3D dose distributions calculated by the TPS and reconstructed for head & neck VMAT delivery and the gamma evaluation between the two distribution.

The reconstructed 3D distribution of the modified plan with 2 leaves shifted with 2 mm

and its gamma evaluation against the original plan is showed in figure 7.2. The evaluation resulted in passing rate 91.72%.

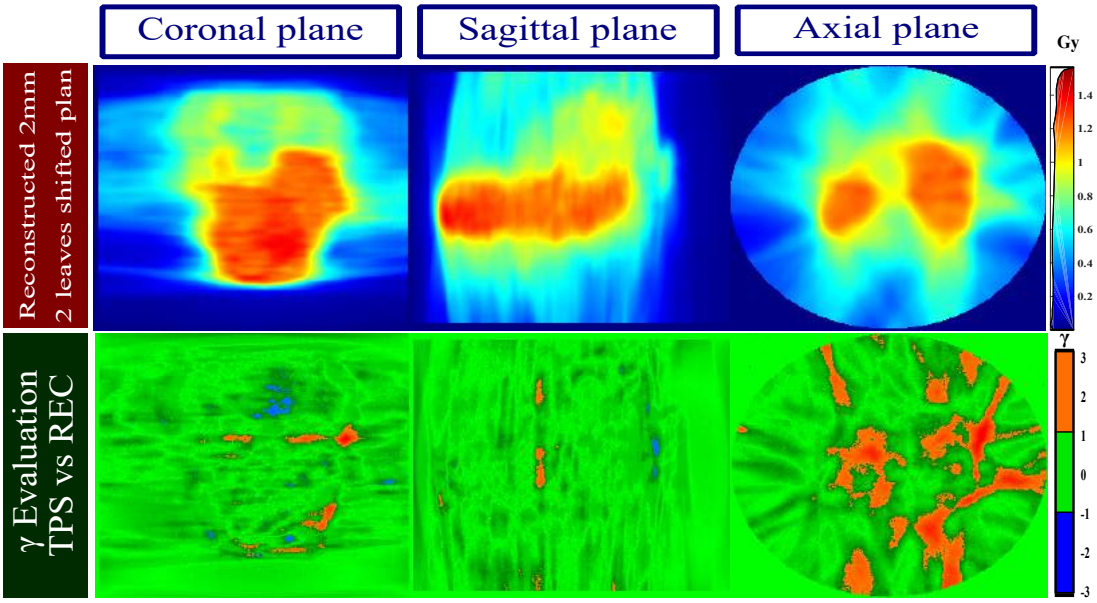

Figure 7.2: Different views of the reconstructed 3D distribution at the corresponding slice of the modified plan with 2 leaves shifted with 2 mm and the gamma evaluation against the original plan.

The reconstructed 3D distribution of the modified plan with 1° rotational shift and its gamma evaluation against the original plan is showed in figure 7.3. The evaluation resulted in passing rate 96.33%.

The reconstructed 3D distribution of the modified plan with additional 4% dose is shown in figure 7.4 along with the gamma evaluation against the original dose distribution calculated by the TPS. The gamma evaluation resulted in 76.55%.

7.4 Discussion and conclusion

The head & neck VMAT case was considered for the sensitivity test due to the associated complexity including a wide range of fields sizes, dose rates and the full rotation of the gantry. In principle, the sensitivity of the algorithm should be higher for less complicated plans in terms of field sizes, dose rates and gantry angles (e.g. brain VMAT, head & neck IMRT etc). The design of the test conducted in this chapter regarded those parameters required to be verified in a patient specific QA [61]. Namely, verification of MUs, data transfer, and dose delivery. Moreover, the sensitivity test was designed to check the feasibility of the proposed reconstruction methodology to detect mechanical malfunctioning.

The gamma evaluation was used for analysis due to its simultaneous criteria of geometric

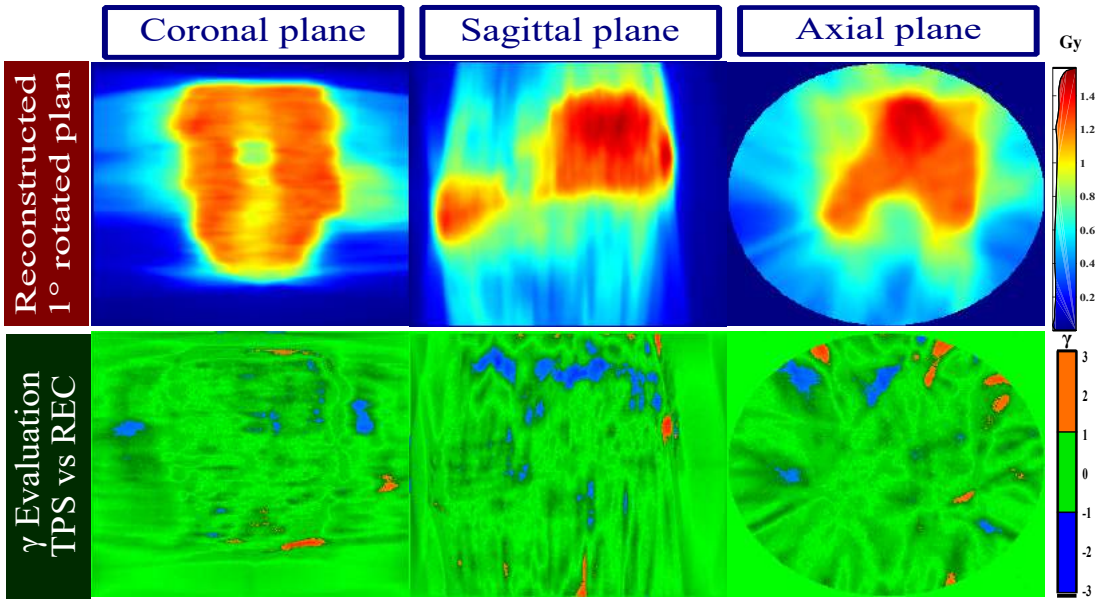

Figure 7.3: Different views of the reconstructed 3D distribution at the iso-center of the modified plan with 1° rotational shift and the gamma evaluation against the original plan.

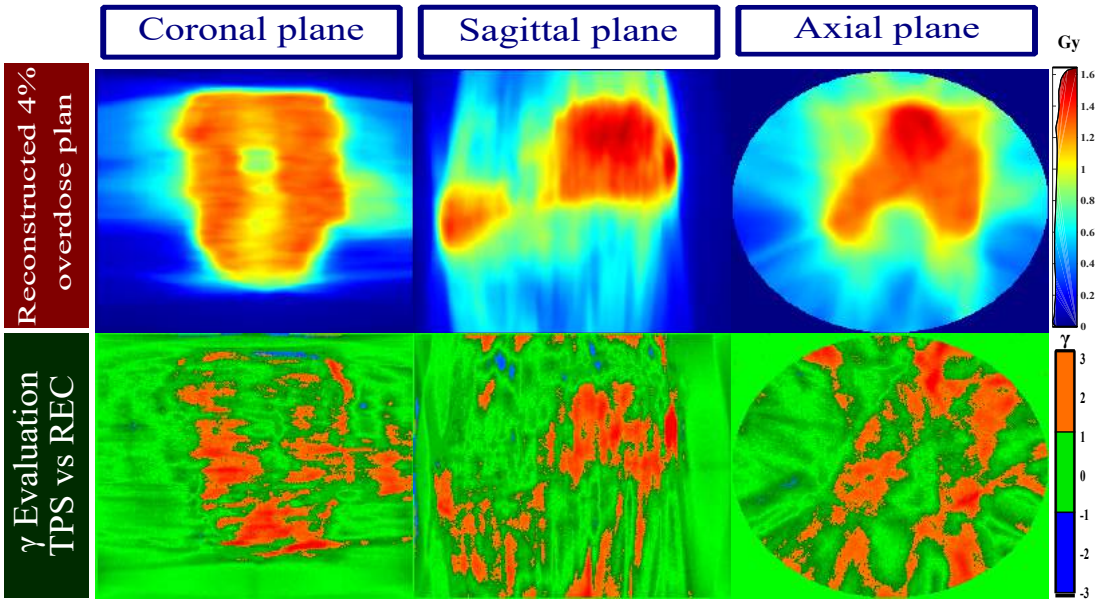

Figure 7.4: Different views of the reconstructed 3D distribution at the iso-center of the modified plan with 4% over dose and the gamma evaluation against the original plan.

and dosimetric differences. The values chosen for the evaluation criteria (i.e. 3% and 3mm) were assessed after having explored several values, the chosen evaluation criteria produced the desired sensitivity matching the accuracy achieved by the methodology. The algorithm demonstrated to be capable of catching geometric errors of MLC in order of 2 mm, gantry angle shift of 1 degree and dosimetric error of $\pm$4%.

In particular, when shifting the two leaves 2 mm away from the original position, the passing rate was reduced by 7.09%. Using a 3D visualization of the gamma index distribution, position and deviation were detected. For rotational shift, the passing rate reduction was relatively small (i.e. 2.48%) leaving overall passing rate above the threshold (i.e. 95%). Though, the rotational shift effect was visible in the 3D visualization.

For the dosimetric sensitivity test, the additional 4% dose caused a reduction of the passing rate equal to 22.26%. The overdose was indicated in the high dose region while minor effect was observable for the low dose region.

For both geometric and dosimetric parameters, stricter gamma criteria can in principle increase the sensitivity to errors. However, since the development of the reconstruction algorithm was designed to pass the gamma evaluation with (3% and 3mm) criteria, the distinction between the deviation related to accuracy or to error in delivery (less than introduced in this chapter) becomes more challenging.

On the other hand, the required sensitivity depends on the clinical relevance of the deviation. In particular, the sensitivity of the proposed methodology meets the requirement used by our clinic.

Chapter 8

Discussion and outlook

The primary objective of this work was to develop a patient-specific QA tool based on EPID. The dosimetric characterization of the used EPID showed technical challenges when using it as a dosimeter in clinical practice. Some of the challenges were related to the physical properties of a-Si detectors such as their non-water equivalent energy response. Other challenges were related to a specific model of EPID or image acquisition software from a particular vendor. The difference between models was presented by comparing dosimetric properties of different EPIDs reported in the literature. Accordingly, a novel method for converting 2D images to dose in water specific for the adopted model was developed. The calibration method was validated for complex radiation fields against different dosimeters. Consequently, a 3D dose reconstruction method was developed based on a series of mathematical operations. The method was solely dependent on the TPS during calibration. As a result, a prediction free 3D dose distribution was obtainable with good accuracy and high spatial resolution even for complex fields. The reconstructed 3D dose distributions of clinical IMRT and VMAT plans were validated against measurements and dose calculation resulting in passing rates that exceeded the recommended limits. The overall method of calibration and reconstruction proved to be sensitive to clinically relevant geometric and dosimetric errors, thus making the approach a good choice for plan-specific QA thanks to superior spatial resolution and comparable accuracy with respect to a commercial dosimeter. Additionally, in air acquisition of images paves the way towards fully automation of a pre-treatment QA procedure. During the method development process, image acquisition and dose reconstruction were performed on two separate computers. However, in order to achieve the minimum human intervention, a simple interface was developed for image acquisition and dose reconstruction in single PC dedicated to EPID dosimetry. For daily clinical pre-treatment QA routine, the QA procedure required only EPID unfolding and alignment to the center of the field. Then the in-air acquisition of the image frames is performed by one click. Currently, the 3D dose reconstruction takes roughly 8 seconds for each image frame. For instance, the irradiation of the head & neck VMAT treatment plan took about 3.7 min and resulted in 510 image frames. By using a personal computer equipped with a 3.40 GHz CPU (Intel® Core TM i7-6700) and 32.0 (GB) RAM, the 3D dose reconstruction required

about 45 min. Parallel computing on a multi-cores computer can considerably reduce the computation time of repetition cycle (i.e. ”for loop”). On the other hand, the calibration processes currently requires human intervention in several steps. The calibration approach relied on mathematical operations (namely: curve fitting, interpolation ...) and optimization algorithms. As outlined in appendix (A), the optimization is designed to generate convolution kernels converting an input image to the desired output. The optimization algorithm searches for the single global minimum in the parameter space. The convergence between global or local minima depends on several factors such as the optimization algorithm and the abundance of available information on the parameter space. For each step, an optimization algorithm was implemented so that the overall calibration approach results as a serious of operations to be performed.

Machine learning algorithm (ML) is a group of computational methods that make use of statistical information about input data to achieve a desired task -without being explicitly programmed- or to produce a particular outcome [159] [160]. Ideally, ML can emulate human decision making after conducting several learning mechanisms to reach the ultimate goal. ML can be applied to any desired discipline in different forms. Envisioning an ML application to the proposed calibration process, three components could be identified: 1) statistical modeling of the parameters, 2) evaluation of the outcome based on initial parameters and 3) optimization of the initial parameters. The logic flow-chart of the process is similar to the optimization process used in the calibration. However, the current optimizer deals with a single parameter for each calibration step. For ML, all the steps could be accounted for in a set of parameters, and the learning process is supervised to reach the ultimate goal. Using the high number of iterative cycle, the optimal combination of convolution kernels and fitting functions could be obtained without human intervention.

8.1 Plan evaluation

In this thesis, gamma evaluation was the adopted method to assess the quality of the dose delivery in comparison to the planned one. The acceptance criteria were chosen in accordance to recommendations and general guidance reported in literature [61]. A recently published report by AAPM considered different QA programs practiced in numerous clinics [161]. Several IMRT patient-specific QA programs and evaluation methods using different types of dosimeters have been reported. Each of these clinics determines their tolerance limits in conjunction with other metrics to serve the final goal of the QA program taking into consideration the technical boundaries of the used QA tool. The report recommends that a universal tolerance limit of gamma passing rate of $\geq 95\%$ with (3%, 2 mm) should be considered. However, this tolerance limit in gamma evaluation resulted too strict for the accuracy of the proposed method, which would require a refinement. On the other hand, some researchers have criticized the gamma evaluation standalone, stating that it cannot predict clinically relevant error [162]. In particular, the passing rate metric could not distinguish between insignificant low dose error and significant overdose to organs at risk. Therefore, DVH has been introduced as an essential tool for patient-specific

QA. As deriving the DVH requires 3D dose distribution, 2D detectors were developed to reconstruct a 3D distribution. Commercial devices currently could provide such a distributions but, yet, they are based on dose interpolation and extrapolation and therefore limited in spatial resolution. A major concern when using the 3D distributions for generating DVHs is that they are measured (and interpolated) in a water equivalent phantom with iso-center and material composition different than those of the patient. This affects the accuracy of the DVH, considering that DVH has been introduced to evaluate the dose calculation accuracy. Validation of the dose calculation accuracy has a fundamental role in patient-specific QA. However, current TPS do not include an accurate modeling of the MLC and surrounding collimators [18] [163]. Besides, dose calculation based on analytical algorithms proved to have uncertainty up to 4.9% in inhomogeneous phantom [164]. Consequently, the usage of an accurate, independent and machine-specific dose calculation engine is essential for implementing an integrated patient-specific QA. For this reason, we put forward a new approach in QA procedures composed by two separate stages: a plan-specific dose delivery and a patient-specific dose calculation.

8.2 Toward a comprehensive patient-specific pre-treatment QA

As demonstrated in this thesis, reconstruction of 3D dose distributions using EPID provided a robust tool for plan delivery verification of complex treatment plans. The method was proved to be sensitive to geometric and dosimetric errors prone to be generated by mis-transferring of data between planning and controlling systems or malfunctioning of linac components. The integrity of the dose calculation within the patient anatomy would need an additional tool for verification. To this purpose, an equipment-specific MC model (implemented in GEANT4) was developed in the framework of another phd project for the Elekta Agility collimator (see 8.1)[55]. The model was used for simulations of the dose distribution of IMRT and VMAT treatment plans in a patient CT. The model includes detailed features of each component in the linac head and t is embedded in a code that converts the DICOM file of the patient CT to attenuation coefficients at the exact position of the patient. Furthermore, the code reads the RTPLAN DICOM file and translates the information to parameters used for MLC positions, dose rates and gantry angle. Although the model is still in the validation phase, the dose calculation accuracy is potentially better than analytical based calculation engines. Once the model is validated for homogenous and inhomogenous phantom, it could be used for patient-specific pre-treatment verification of dose calculation. Furthermore, the calculation of the DVH would gain in accuracy, being based on the accurate modeling of patient anatomy.

This dose calculation verification together with the plan-specific QA tool developed in this thesis would make the pre-treatment QA more robust and sensitive to errors that could occur in the radiation therapy work-flow. A flowchart of the proposed QA procedure (and its two constitutional stages) is outlined in figure 8.2.

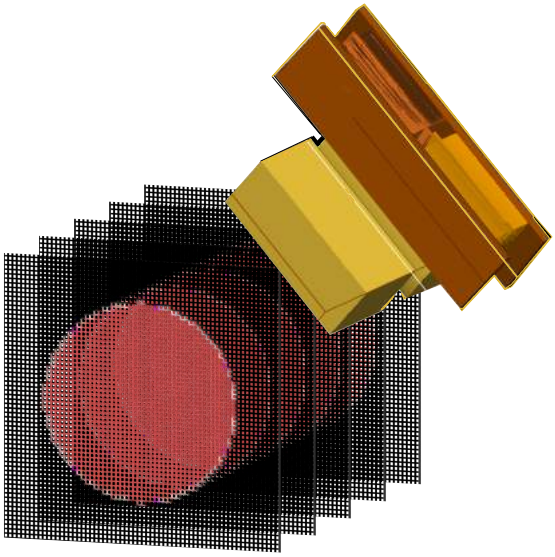

Figure 8.1: The GEANT4 model of the ELEKTA synergy linac and the CT of a water phantom (courtesy S. Veloza and J. Martin).

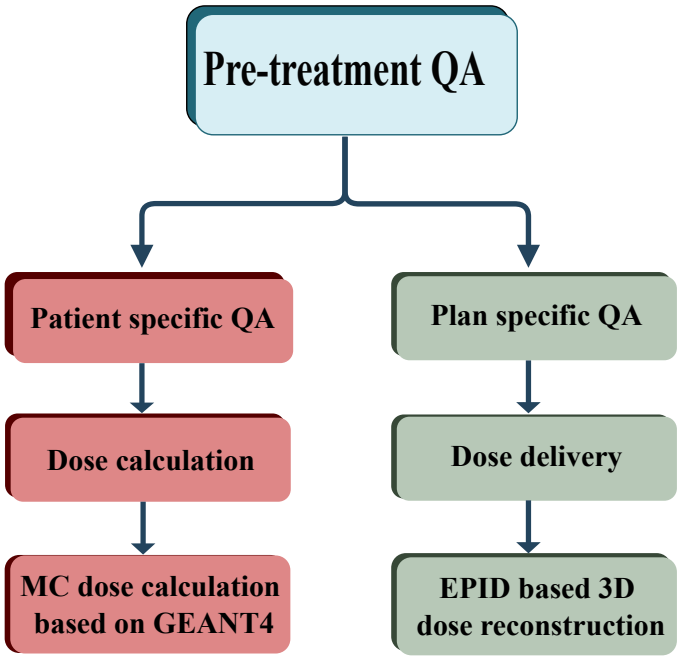

Figure 8.2: A flowchart of the pre-treatment QA procedure and its two constitutional stages.

However, the drawback of the MC implementation for dose verification is the computational time required to achieve statistically adequate accuracy and precision. Currently, the developed model needs a few hours to simulate a full IMRT treatment plan. The simulation time is set to be reduced significantly using parallel computing. In order to not affect clinical routine, the MC calculation could be performed overnight. Though, parallel computing opens opportunities for more time efficient QA procedures.

8.3 In-vivo dosimetry

EPID-based in-vivo dosimetry has proliferated in the past few years. The final aim is to provide an accurate and independent dose verification of the treatment delivery. In addition to sensitivity to errors in dose calculation, data transfer, and dose delivery as in pre-treatment QA, in-vivo dosimetry would enable the identification of errors generated by patient setup and changes in patient anatomy. However, current applications of EPID-based dosimetry are focused on pre-treatment dose verification and applications for in-vivo dosimetry are still limited. In brief, the proposed concept for EPID-based in-vivo dosimetry relies on either predicting images at the EPID level through patient anatomy extracted from the treatment planning CT or estimating fluences from the EPID image to forward calculate the dose as imparted in the patient CT. The ability of both approaches to detect errors undetectable by a solely pre-treatment QA has been demonstrated by different groups [120] [123] [135]. All these methods were very sensitive to anatomical changes. Although this is one of the main advantages of in-vivo over pre-treatment dosimetry, the interpretation of observed differences between measured and predicted 3D dose distributions is complicated. Since the in-vivo methods rely on the treatment planning patient CT, the generated dose distribution is valid for dose verification only and is not representative of the ”true” dose delivered to the patient. Consequently, when a deviation is detected, the decision making for re-planning or other adaptive strategies is performed qualitatively by visual inspection of the CBCT acquired prior to treatment [165]. Indeed, implementing the in-vivo dosimetry provides a better safety net for the treatment delivery in comparison to full dependence on pre-treatment QA. However, it is still a dosimetric verification tool rather than independent dosimetry, and its accuracy is associated with good modeling of the linac components and modulation (e.g. MLC movement) and patient anatomy. As an alternative approach to EPID-based in-vivo dosimetry, the proposed comprehensive patient-specific QA, including the plan-specific QA object of this thesis work, is planned to be implemented in our clinic.

The rationale for in-vivo dosimetry is to verify patient setup and patient anatomy which have not been verified by the patient-specific QA. The proposal is based on using a daily CBCT acquired prior to dose delivery with interpolated MLC positions from EPID images and doses measured by linac monitor chambers. All these data are imported into the machine-specific MC calculation engine to generate a 3D dose distribution. Thus, the proposed in-vivo dosimetry is independent of TPS calculation or patient planning CT. The generated 3D dose distribution can be compared to the planned distribution using gamma

evaluation or DVH. Consequently, in case of detected deviation, the decision making can be guided by quantitative evaluation with higher confidence level. Additionally, the in-vivo 3D dose distributions of both fraction by fraction and/or dose accumulation can be stored and used for auditing purposes. The feasibility and proof of concept of this proposal are yet to be tested. Factors like the additional dose due to imaging to the patient, the extended computational time and the added workload on staff have to be considered with respect to the outcome benefit.

Chapter 9

Conclusion

Treating cancer tumor with photon radiation has begun nearly a century ago. As the technology proliferated in the last two decades, the techniques of delivering radiation dose have been enormously developed in terms of accuracy and precision. The improvement has made use of complex auxiliary systems attached to the linac aiming at the best conforming of the dose to the tumor in conjunction with the best dose sparing of healthy tissues. Currently, the delivery of the radiation dose reached an unprecedented level of accuracy, thanks to the advancement in linac mechanics and its control system along with its authentic dose calculation engine. However, in order to fully exploit the anticipated advantages of the accuracy of the current technology, a robust QA program has to be conducted. As the introduction of supporting systems to the treatment chain increases, new measures for the QA program has to be introduced as well. Yet, this accompaniment is not optimum since the development of the QA methods and apparatus has been slower than the treatment technology.

For complex treatment delivery techniques in radiation therapy such as IMRT/VMAT, a patient-specific QA approach has been recommended. This approach requires, in addition to independent dose calculation engine, a dosimetry system with high accuracy and resolution and preferably able to generate a 3D dose distribution. Dosimeters with such (or approaching these) characteristics are commercially available but with the limitation of increased set-up time. The EPID, a built-in imaging detector in most modern linacs poses potential dosimetric features. In this thesis, the dosimetric features of a specific EPID have been explicitly investigated. Making use of the knowledge gained from EPID characterization, a method to calibrate EPID to be used as a dosimeter in water has been presented. Converting a the 2D image, as acquired from EPID, into a 2D dose distribution enables the comparison with reference dosimeters. The accuracy of the calibration method has been validated for regular QA tests and real clinical scenarios. As this calibration presents a useful tool for QA programs, the advantage of producing 2D dose distributions with high accuracy and resolution with no need for human intervention in either detector positioning nor passive processing (as in films and TLDs). In fact, the trend of QA tool development tends to march toward 3D dosimetry. Accordingly, a novel approach to reconstruct a

3D dose distribution from 2D dose distributions has also been developed in this thesis. A series of mathematical operations have been explicitly implemented to generate a 3D distribution matching the desired spatial resolution and having comparable accuracy with the TPS dose calculation. The operations resulted in an algorithm that back-project the 2D dose distributions at different levels thus forming (reconstructing) a 3D dose distribution. Additionally, the back-projection mimics energy deposition and attenuation as in a virtual cylindrical phantom. Therefore, the reconstructed 3D dose distributions have been validated for conventional and complex clinical treatment plans against reference measurements. The methodology has also been tested for sensitivity to small geometric and dosimetric deviations, satisfying the required criteria.

As the aim of this thesis is to develop a QA tool for patient-specific QA, the developed work presents a preferable methodology over others proposed in literature and also over commercial devices. The advantages of the presented work are the fast and in-air acquisition of the measurements combined with a non labor intensive set-up, and the prediction-free (except in calibration process) and the water-equivalent features of the reconstructed 3D dose distribution with relatively good accuracy and optimal and desired spatial resolution. These advantages represent favorable characteristics for clinical dosimetry and specifically for patient-specific QA program. Besides the clinical application demonstrated in this thesis, the methodology can be used for research and auditing purposes.

As final remark, the remaining limitation of the proposed methodology is the current implementation of the calibration process. However, technical improvements of the implemented codes are foreseen. The development includes a user-friendly interface, optimization of computational time and generalization to other EPID models.

Appendix A

Mathematical optimization and code implementation

A.1 Overview

Mathematical optimization is the process to search the best solution out of a set of possible choices with respect to a pre-specified criterion. Depending on the criteria, the optimization process consists of minimization or maximization (depending on the criteria) of the objective function f(x), where x is an N-dimensional vector referred to as the parameters of variables within is the feasible set S (search space). Typically, the optimization consists of iterations where the vector of parameters minimizing or maximizing the objective function is carried on. The search space can be limited by constraints, such that h(x) = c and g(x) $\leq d$ [166]. The feasible solution that minimizes or maximizes the objective function is the optimal solution. The optimal solution can be either a global or local minima . While local minimum applies for a neighborhood, the global one applies for the entire search space S. An example of different minima of the function in equation A.1 is illustrated in figure (A.1).

$$h(x) = 2 + \cos(x) + \frac{cos(2x - 0.5)}{2} \tag{A.1}$$

Several algorithms have been proposed for solving optimization problems. However, many solvers suffer from distinguishing between global and local minima. Therefore, global optimization mathematics and numerical analysis tools were developed as supporting algorithms for problem solvers. As a result, the optimization code constitute of a problem solver and analysis tools to verify the best solution from a set of input values from within an allowed set, computing the output of the function and recording the best output values found during the process.

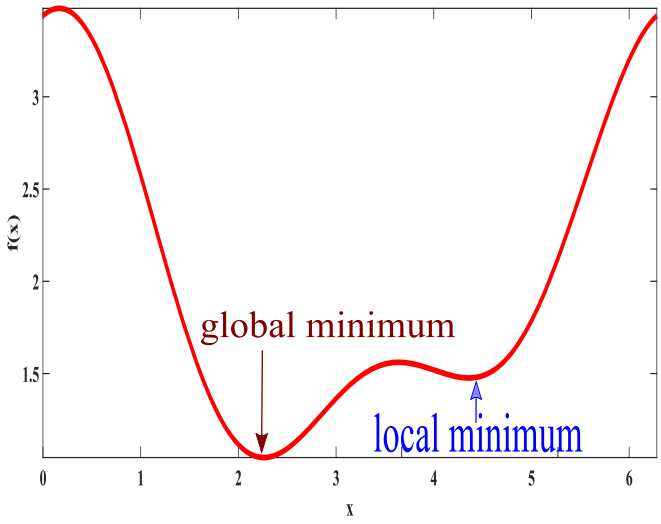

Figure A.1: Local and global minima for function A.1.

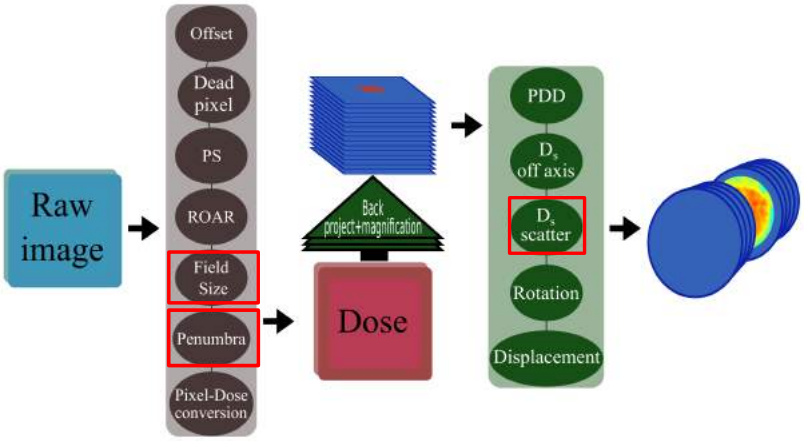

Figure A.2: The steps of the methodology presented in this thesis that required an optimization process are marked with red square in the flowchart.

A.2 Code implementation

MATLAB in conjunction with Optimization Toolbox™ offers several algorithms for numerical optimization. The optimization processes implemented in this thesis relied on MATLAB. The steps of the methodology (EPID calibration and 3D dose reconstruction) that required an optimization process are marked in figure (A.2). The choice of the algorithm and the implemented objective function are outlined in the following.

- **Field size correction** the aim of this optimization was to obtain the single parameter relevant to the exponential fitting function defining the field size dependent

convolution kernel. The objective function to be minimized was the square difference between the reference measurement and the central values of the integrated image frames. A non-linear, unconstrained and derivative-free algorithm as implemented in ”fminsearch.m” was used. Details of the optimization process are in the following.

FS correction

```
%Set the objective function
function [f]=Kfun(b,Raw,IC)
x=0:30;
model=b(1).*exp(-(x).^2);
[xx,yy] = ndgrid(round(-p:p),round(-p:p));
dist    =   sqrt(xx.^2 + yy.^2);
RadialKernel    =   interp1(x, model,dist);
RadialKernel(isnan(RadialKernel))=model(1);

ConvImage=(conv2(Raw,RadialKernel,'same'));

% get the centeral dose
center  =   [512.5,512.5];
radius  =  5; % in pixels
[XX,YY] = ndgrid((1:1024)-center(1),(1:1024)-center(2));
ROIMask = ((XX.^2 + YY.^2)<radius^2);
Elut= mean2(ConvImage(ROIMask));
f=sum((Elut-IC).^2);
end


% Set the optimization solver and its options
b0= 0.02; % Initial guess
parfor f=1:5 % number of measurements
[PAR_FS(f).I,opt_value] = fminsearch(@(b)
 Kfun(b,Raw(f).I,IC(f)),b0,...
    optimset('MaxFunEvals',1e5,'MaxIter',1e4,'display',...
    'iter','TolFun',1e-20));
end
% Raw is the integrated EPID image
% IC is reference measurements
% PAR_FS is the parameters resulted from the optimization.
% opt_value is the optimum (dif).

% Find the number of the irradiated pixels for the integrated EPID
 images
% (Raw)
for f=1:8
[IPix(f),~]=size(find(Raw(f).Image>(0.5).*3.3817e+04));
end

% Fit PAR_FS against IPix.
```

- **Penumbra correction** the objective function was defined as the sum square difference between the two profiles measured by the reference detector and the image frame. As the required convolution kernel was modeled by a Lorentz fitting function with 4 coefficients (vector of parameters), the initialization parameters were guessed randomly. Details of the optimization process are in the following.

Penumbra correction

```
% Create the objective function
function [dif]=PfunProf(b,EP_I,Micro_Profile)

% EP_I is the EPID integrated image
% Micro_diamond profile (make sure it has same size as EPID inline
 profile.

%create a convolution kernel
  x=0:30;
    model=b(1)./(((x - b(2)).^2 )+ b(3) + b(4))  ;
    [xx,yy] = ndgrid(-10:1:10,-10:1:10);
    dist    =   sqrt(xx.^2 + yy.^2);
    RadialKernel    =   interp1(x, model,dist);
    RadialKernel(isnan(RadialKernel))=model(1);
    RadialKernel = RadialKernel./sum(sum(RadialKernel));

ConvImage=conv2(EP_I,RadialKernel,'same');

Epidprof= ConvImage(512,:)';  % Central inline profile

Epidprof=Epidprof(13:1007);    % Allign with Microdiamond profile

dif=sum((Epidprof-Micro_Profile).^2);
end
```

```
% Set the optimization solver and its options
v0 = [0.03  1  0.9  0.9]; % Initial guess
[PAR,opt_value] = fminsearch(@(b)
 PfunProf(b,ImageProfile,PlanProfile), ...
    v0,optimset('MaxFunEvals',1e5,'MaxIter',1e6,'display','iter',...
    'TolX',1e-12,'TolFun',1e-200));

% PAR is the parameters resulted from the optimization.
% opt_value is the optimum (dif).
```

- **Depth specific lateral scatter correction** two convolution kernels and therefore two separated optimization processes were considered, corresponding to the segmented hot and cold regions of the image frame. The optimization function was the sum square difference of the mean between the in-line and cross-line profiles. The convolution kernel was modeled as a Lorentz fitting function with 4 coefficients. In this step, the algorithm implemented in ”fminsearch.m” converged to local minima. To try to approach global convergence [167], the algorithm particle swarm was used with certain constraints. As the ”particle swarm” algorithm is a population-based optimization method (inspired by the motion of a bird flock, or fish schooling), the computation speed is slower than a derivative- free method. The optimization process implemented to generate the two kernels parameters is below.

Depth specific lateral scatter correction

```
%set the objective function
function [dif]=Lateral_Dep(b,Image,Ref)

%create a convolution kernel
x=-10:10;
model=b(1)./(((x - b(2)).^2 )+ b(3) + b(4))  ;
F=15;
[xx,yy] = ndgrid(round(-F:F),round(-F:F));
dist    =   sqrt(xx.^2 + yy.^2);
RadialKernel    =   interp1(x,model,dist);
RadialKernel(isnan(RadialKernel))=0;
RadialKernel(isinf(RadialKernel))=0;

% convolve Image
cImage=conv2(Image,RadialKernel,'same');

% Extract Cross-line and In-line profiles
Cr_Pl=Ref(128,:);
Cr_cIm=cImage(128,:);

In_Pl=Ref(:,128);
In_cIm=cImage(:,128);

% sum square difference
dif_In=sum((Cr_cIm-Cr_Pl).^2);
dif_Cr=sum((In_cIm-In_Pl).^2);

%Average
dif=(dif_In+dif_Cr)./2;
end
```

```
% set the comparision images
for z=1:256 % z is the number of planar xy images

 Image= REC_Dose(:,:,z); % Reconstructed matrix from EPID
 Ref= TPS(:,:,z); % Reference matrix

% find the area with Dose higher than 15%
[row1(z).I,col1(z).I]=(find(Image>=(0.15).*max(Image(:))));

%Create hot images
for i=1:length(row1(z).I)
dummy_Image_high(row1(z).I(i),col1(z).I(i),z)=...
    Image(row1(z).I(i),col1(z).I(i));
end

for i=1:length(row1(z).I)
dummy_Ref_high(row1(z).I(i),col1(z).I(i),z)=Ref(row1(z).I(i),col1(z).I(i));
end

% set the optimization options
lb=[-5 eps -5 -5]; %lower limit
ub=[10 5 5 5 ];     % higher limit
options =
 optimoptions('particleswarm','SwarmSize',2000,'HybridFcn',...
    @fmincon, 'UseParallel',1,'InitialSwarmSpan',1e3,'TolFun',...
    1e-6,'display','iter');


%set the optimization solver
[FF_high_min(z,:),opt_val_h(z)] = particleswarm(@(b)...
    Lateral_Dep(b,dummy_Image_high(:,:,z),dummy_Ref_high(:,:,z)),...
    4,lb,ub,options);
```

```
%repeat the same procedure for the low dose region

[row2(z).I,col2(z).I]=(find(Image<(0.15).*max(Image(:))));

%Create cold images
for i=1:length(row2(z).I)
dummy_Image_low(row2(z).I(i),col2(z).I(i),z)=...
    Image(row2(z).I(i),col2(z).I(i));
end
for i=1:length(row2(z).I)
dummy_Ref_low(row2(z).I(i),col2(z).I(i),z)=Ref(row2(z).I(i),col2(z).I(i));
end

% set the optimization options
lb=[-5 eps -5 -5];
ub=[10 5 5 5 ];
options =
 optimoptions('particleswarm','SwarmSize',2000,'HybridFcn',...
    @fmincon, 'UseParallel',1,'InitialSwarmSpan',1e3,'TolFun',...
    1e-6,'display','iter');

%set the optimization solver
[FF_low_min(z,:),opt_val_l(z)] = particleswarm(@(b) ...
    Lateral_Dep(b,dummy_Image_low(:,:,z),dummy_Ref_low(:,:,z)),...
    4,lb,ub,options);

 end
```

Finally, it is worth mentioning that the choice of the optimization algorithms excluded those not embedded in MATLAB. Better results in terms of accuracy and precision and better performance (computational speed, depending on the applicability of parallel computing) can achieved with different algorithms.

Appendix B

List of publications and conference contributions

Peer-reviewed articles

Abdulaziz Alhazmi, Chiara Gianoli, Sebastian Neppl, Juliana Martins, Stella Veloza, Mark Podesta, Frank Verhaegen, Michael Reiner, Claus Belka, and Katia Parodi. A novel approach to epid-based 3d volumetric dosimetry for imrt and vmat qa. *Physics in Medicine & Biology*, 63(11):115002, 2018.

Conference contributions

Abdulaziz Alhazmi, Chiara Gianoli, Juliana Martins, Sebastian Neppl, Stella Veloza, Michael Reiner, Claus Belka, and Katia Parodi. A novel epid-based 3d dose reconstruction for imrt qa. *Medical Physics*, 44(6):2887-2887, 2017. *(Poster)*

Juliana Cristina Martins, Abdulaziz Alhazmi, Sebastian Neppl, Claus Belka, Michael Reiner, Katia Parodi, and Stella Veloza. An equipment-specific geant4 model for the elekta agility collimator. *Physica Medica*, 42:30-31, 2017. *(Talk)*

Abdulaziz Alhazmi, Chiara Gianoli, Juliana Martins, Sebastian Neppl, Stella Veloza, Michael Reiner, Claus Belka, and Katia Parodi. Sensitivity analysis of epid-based 3d dose reconstruction for vmat qa. *Radiotherapy and Oncology*, 127, 2018. *(e-Poster)*

Abdulaziz Alhazmi, Chiara Gianoli, Juliana Martins, Sebastian Neppl, Stella Veloza, Michael Reiner, Claus Belka, and Katia Parodi. Proposal of a comprehensive pre-treatment qa procedure in imrt/vmat techniques. *Physica Medica*, 52:149, 2018.*(e-Poster)*

Rangoli Saxena, Juliana Cristina Martins, Abdulaziz Alhazmi, Sebastian Neppl, Michael Reiner, Claus Belka, Stella Veloza, and Katia Parodi. Optimization of phase space files from clinical linear accelerators. *Physica Medica*, 52:12, 2018. *(Poster)*

Abdulaziz Alhazmi, Chiara Gianoli, Sebastian Neppl, Juliana Cristina Martins, Stella Veloza, Mark Podesta, Frank Verhaegen, Michael Reiner, Claus Belka, Katia Parodi. EPID-based 3D dose reconstruction for plan specific pre-treatment QA. *DGMP 2018 (In press)*

Rangoli Saxena, Juliana Cristina Martins, Abdulaziz Alhazmi, Sebastian Neppl, Michael Reiner, Claus Belka, Stella Veloza, Katia Parodi. Optimization of IAEA Phase Space Files for Monte Carlo Dose Calculation. *DGMP 2018 (In press)*

Bibliography

[1] II Abubakar, T Tillmann, and A Banerjee. Global, regional, and national age-sex specific all-cause and cause-specific mortality for 240 causes of death, 1990-2013: a systematic analysis for the global burden of disease study 2013. *Lancet*, 385 (9963):117–171, 2015.

[2] Bernard Stewart, Christopher Wild, et al. World cancer report 2014. *Health*, 2017.

[3] Christina Fitzmaurice, Daniel Dicker, Amanda Pain, Hannah Hamavid, Maziar Moradi-Lakeh, Michael F MacIntyre, Christine Allen, Gillian Hansen, Rachel Woodbrook, Charles Wolfe, et al. The global burden of cancer 2013. *JAMA oncology*, 1(4):505–527, 2015.

[4] Jacques Ferlay. Globocan 2008 v2. 0, cancer incidence and mortality worldwide: Iarc cancerbase no. 10. *http://globocan. iarc. fr*, 2010.

[5] Cai Grau, Josep M Borras, Julian Malicki, Ben Slotman, Peter Dunscombe, Mary Coffey, Donal Hollywood, Ferran Guedea, Chiara Gasparotto, and Yolande Lievens. Radiotherapy capacity in europe. *The Lancet Oncology*, 14(6):e196–e198, 2013.

[6] Kimberly D Miller, Rebecca L Siegel, Chun Chieh Lin, Angela B Mariotto, Joan L Kramer, Julia H Rowland, Kevin D Stein, Rick Alteri, and Ahmedin Jemal. Cancer treatment and survivorship statistics, 2016. *CA: a cancer journal for clinicians*, 66 (4):271–289, 2016.

[7] Wolfgang C. Schlegel, L.W. Brady, H.P. Heilmann, Thomas. Bortfeld, M. Molls, and Anca L. Grosu. *New Technologies in Radiation Oncology*. Medical Radiology. Springer Berlin Heidelberg, 2009. ISBN 9783540800057.

[8] Faiz Khan. *The Physics of Radiation Therapy*. Lippincott Williams & Wilkins, 2010. ISBN 9780781788564.

[9] Arabinda Kumar Rath and Narayan Sahoo. *Particle Radiotherapy: Emerging Technology for Treatment of Cancer*. Springer, 2016.

[10] Seymour H Levitt, James A Purdy, Carlos A Perez, and Srinivasan Vijayakumar. *Technical basis of radiation therapy*. Springer, 2012.

[11] Yasumasa. Nishimura and Ritsuko Komaki. *Intensity-Modulated Radiation Therapy: Clinical Evidence and Techniques*. Springer Japan, 2015. ISBN 9784431554868.

[12] Rajesh A Kinhikar, Amol B Pawar, Umesh Mahantshetty, Vedang Murthy, Deepak D Dheshpande, Shyam K Shrivastava, et al. Rapid arc, helical tomotherapy, sliding window intensity modulated radiotherapy and three dimensional conformal radiation for localized prostate cancer: a dosimetric comparison. *Journal of cancer research and therapeutics*, 10(3):575, 2014.

[13] Simon. Lo, Bin S. Teh, Jiade. Lu, and Tracey E. Schefter. *Stereotactic Body Radiation Therapy*. Medical Radiology. Springer Berlin Heidelberg, 2012. ISBN 9783642256059.

[14] RG Parker, CR Bogardus, GE Hanks, CG Orton, and M Rotman. Radiation oncology in integrated cancer management: Report of the inter-society council for radiation oncology. *Merrifield, VA: American College of Radiology Publications, ISCRO*, 1991.

[15] Ervin B Podgorsak et al. Radiation oncology physics. *Vienna: International Atomic Energy Agency*, pages 123–271, 2005.

[16] Jeffrey F Williamson, Peter B Dunscombe, Michael B Sharpe, Bruce R Thomadsen, James A Purdy, and James A Deye. Quality assurance needs for modern image-based radiotherapy: recommendations from 2007 interorganizational symposium on "quality assurance of radiation therapy: challenges of advanced technology". *International Journal of Radiation Oncology* Biology* Physics*, 71(1): S2–S12, 2008.

[17] International Atomic Energy Agency. *Accuracy Requirements and Uncertainties in Radiotherapy*. IAEA Human Health Series. International Atomic Energy Agency, 2017. ISBN 9789201008152.

[18] Ben Mijnheer. *Clinical 3D Dosimetry in Modern Radiation Therapy*. CRC Press, 2017.

[19] Ross I Berbeco. *Beam's Eye View Imaging in Radiation Oncology*. CRC Press, 2017.

[20] Ervin B Podgorsak. *Radiation physics for medical physicists*. Springer Science & Business Media, 2010.

[21] Glenn F Knoll. *Radiation detection and measurement*. John Wiley & Sons, 2010.

[22] International Atomic Energy Agency. *Implementation of the international code of practice on dosimetry in radiotherapy (TRS 398): review of testing results*. Implementation of the International Code of Practice on Dosimetry in Radiotherapy (Trs:398): Review of Testing Results. International Atomic Energy Agency, 2005. ISBN 9789201050052.

[23] Peter R Almond, Peter J Biggs, Bert M Coursey, WF Hanson, M Saiful Huq, Ravinder Nath, and DWO Rogers. Aapm's tg-51 protocol for clinical reference dosimetry of high-energy photon and electron beams. *Medical physics*, 26(9):1847–1870, 1999.

[24] José Manuel Lárraga-Gutiérrez, Paola Ballesteros-Zebadúa, Miguel Rodríguez-Ponce, Olivia Amanda García-Garduño, and Olga Olinca Galván De la Cruz. Properties of a commercial ptw-60019 synthetic diamond detector for the dosimetry of small radiotherapy beams. *Physics in Medicine & Biology*, 60(2):905, 2015.

[25] Syed Naeem Ahmed. *Physics and engineering of radiation detection*. Academic Press, 2007.

[26] S Reinhardt, M Hillbrand, JJ Wilkens, and W Assmann. Comparison of gafchromic ebt2 and ebt3 films for clinical photon and proton beams. *Medical physics*, 39(8): 5257–5262, 2012.

[27] Naoki Hayashi, Ryan L Malmin, and Yoichi Watanabe. Dosimetric verification for intensity-modulated arc therapy plans by use of 2d diode array, radiochromic film and radiosensitive polymer gel. *Journal of radiation research*, 55(3):541–552, 2014.

[28] Yuji Nakaguchi, T Oono, F Araki, and M Maruyama. Physical characterizations for an integrated 160-leaf multi-leaf collimator with a new concept design. *Nihon Hoshasen Gijutsu Gakkai zasshi*, 69(7):778–783, 2013.

[29] James L Bedford, Michael DR Thomas, and Gregory Smyth. Beam modeling and vmat performance with the agility 160-leaf multileaf collimator. *Journal of applied clinical medical physics*, 14(2):172–185, 2013.

[30] Frank Verhaegen and Jan Seuntjens. Monte carlo modelling of external radiotherapy photon beams. *Physics in medicine & biology*, 48(21):R107, 2003.

[31] Timothy C Zhu, Anders Ahnesjö, Kwok Leung Lam, X Allen Li, Chang-Ming Charlie Ma, Jatinder R Palta, Michael B Sharpe, Bruce Thomadsen, and Ramesh C Tailor. Report of aapm therapy physics committee task group 74: In-air output ratio, sc, for megavoltage photon beams. *Medical physics*, 36(11):5261–5291, 2009.

[32] TD Sterling. Derivation of a mathematical expression for the percent depth dose of cobalt 60 beams and visualization of multiple fields dose distributions. *Br J Radiol*, 37:544–550, 1964.

[33] David S Chang, Foster D Lasley, Indra J Das, Marc S Mendonca, Joseph R Dynlacht, et al. *Basic radiotherapy physics and biology*. Springer, 2014.

[34] Anders Ahnesjö and Maria Mania Aspradakis. Dose calculations for external photon beams in radiotherapy. *Physics in Medicine & Biology*, 44(11):R99, 1999.

[35] Anders Ahnesjö, Lars Weber, Anders Murman, Mikael Saxner, Ingvar Thorslund, and Erik Traneus. Beam modeling and verification of a photon beam multisource model. *Medical physics*, 32(6Part1):1722–1737, 2005.

[36] Tommy Knöös, Elinore Wieslander, Luca Cozzi, Carsten Brink, Antonella Fogliata, Dirk Albers, Håkan Nyström, and Søren Lassen. Comparison of dose calculation algorithms for treatment planning in external photon beam therapy for clinical situations. *Physics in Medicine & Biology*, 51(22):5785, 2006.

[37] Christopher M Bragg and John Conway. Dosimetric verification of the anisotropic analytical algorithm for radiotherapy treatment planning. *Radiotherapy and oncology*, 81(3):315–323, 2006.

[38] Wen-Zhou Chen, Ying Xiao, and Jun Li. Impact of dose calculation algorithm on radiation therapy. *World journal of radiology*, 6(11):874, 2014.

[39] W Ralph Nelson, David WO Rogers, and H Hirayama. The egs4 code system. Technical report, 1985.

[40] J Baro, J Sempau, JM Fernández-Varea, and F Salvat. Penelope: an algorithm for monte carlo simulation of the penetration and energy loss of electrons and positrons in matter. *Nuclear Instruments and Methods in Physics Research Section B: Beam Interactions with Materials and Atoms*, 100(1):31–46, 1995.

[41] J Briesmeister. Mcnp–a general monte carlo n-particle transportation code. Technical report, LA-1625-M, version, 1997.

[42] Sea Agostinelli, John Allison, K al Amako, Jo Apostolakis, H Araujo, P Arce, M Asai, D Axen, S Banerjee, G 2 Barrand, et al. Geant4—a simulation toolkit. *Nuclear instruments and methods in physics research section A: Accelerators, Spectrometers, Detectors and Associated Equipment*, 506(3):250–303, 2003.

[43] R Capote, R Jeraj, CM Ma, DWO Rogers, F Sánchez-Doblado, J Sempau, J Seuntjens, and JV Siebers. Phase-space database for external beam radiotherapy. summary report of a consultants' meeting. Technical report, International Atomic Energy Agency, 2006.

[44] Miguel Antonio Cortés-Giraldo, José Manuel Quesada, María Isabel Gallardo, and Roberto Capote. An implementation to read and write iaea phase-space files in geant4-based simulations. *International journal of radiation biology*, 88(1-2):200–208, 2012.

[45] Obioma Nwankwo, Gerhard Glatting, Frederik Wenz, and Jens Fleckenstein. A single-source photon source model of a linear accelerator for monte carlo dose calculation. *PloS one*, 12(9):e0183486, 2017.

[46] Iwan Kawrakow, Matthias Fippel, and Klaus Friedrich. 3d electron dose calculation using a voxel based monte carlo algorithm (vmc). *Medical physics*, 23(4): 445–457, 1996.

[47] Josep Sempau, Scott J Wilderman, and Alex F Bielajew. Dpm, a fast, accurate monte carlo code optimized for photon and electron radiotherapy treatment planning dose calculations. *Physics in Medicine & Biology*, 45(8):2263, 2000.

[48] Jens Fleckenstein, Lennart Jahnke, Frank Lohr, Frederik Wenz, and Jürgen Hesser. Development of a geant4 based monte carlo algorithm to evaluate the monaco vmat treatment accuracy. *Zeitschrift für Medizinische Physik*, 23(1):33–45, 2013.

[49] Satish Pelagade, Kalpana Thakur, Tushar Bopche, Devang Bhavsar, Daxa Patel, Ruchita Shah, and Rakeshkumar Vyas. Commissioning and quality assurance of a commercial intensity modulated radiotherapy (imrt) treatment planning system preciseplan. *Turkish Journal of Cancer*, 37(1), 2007.

[50] Benjamin E Nelms and Jeff A Simon. A survey on planar imrt qa analysis. *Journal of applied clinical medical physics*, 8(3):76–90, 2007.

[51] Markus Alber, Sara Broggi, Carlos De Wagter, Ines Eichwurzel, Per Engström, Claudio Fiorino, Dietmar Georg, Günther Hartmann, Tommy Knöös, Antonio Leal, et al. Guidelines for the verification of imrt. *ESTRO booklet*, 7, 2008.

[52] Todd Pawlicki, Sua Yoo, Sharon K McMillan, Roger K Rice, J Donald Russell, John M Pacyniak, Milton K Woo, Parminder S Basran, Jason Shoales, Arthur L Boyer, et al. Moving from imrt qa measurements toward independent computer calculations using control charts. *Radiotherapy and Oncology*, 89(3):330–337, 2008.

[53] Baozhou Sun, Dharanipathy Rangaraj, Sunita Boddu, Murty Goddu, Deshan Yang, Geethpriya Palaniswaamy, Sridhar Yaddanapudi, Omar Wooten, and Sasa Mutic. Evaluation of the efficiency and effectiveness of independent dose calculation followed by machine log file analysis against conventional measurement based imrt qa. *Journal of applied clinical medical physics*, 13(5):140–154, 2012.

[54] Jia-Ming Wu, Chung-Ming Kuo, and Ching-Jiang Chen. Dose verification in intensity modulation radiation therapy: a fractal dimension characteristics study. *BioMed research international*, 2013, 2013.

[55] Juliana Cristina Martins, Abdulaziz Alhazmi, Sebastian Neppl, Claus Belka, Michael Reiner, Katia Parodi, and Stella Veloza. Abstract id: 144 an equipment-specific geant4 model for the elekta agility collimator. *Physica Medica: European Journal of Medical Physics*, 42:30–31, 2017.

[56] Benjamin Nelms, Cassandra Stambaugh, Dylan Hunt, Brian Tonner, Geoffrey Zhang, and Vladimir Feygelman. Methods, software and datasets to verify dvh calculations against analytical values: Twenty years late (r). *Medical physics*, 42 (8):4435–4448, 2015.

[57] Michael Goitein. *Radiation Oncology: A Physicist's-Eye View*. Biological and Medical Physics, Biomedical Engineering. Springer New York, 2007. ISBN 9780387726458.

[58] Ann Barrett, Jane Dobbs, and Tom Roques. *Practical Radiotherapy Planning Fourth Edition*. Taylor & Francis, 2009. ISBN 9780340927731.

[59] Mark Podesta, Lucas CGG Persoon, and Frank Verhaegen. A novel time dependent gamma evaluation function for dynamic 2d and 3d dose distributions. *Physics in Medicine & Biology*, 59(20):5973, 2014.

[60] Alan C Hartford, James M Galvin, David C Beyer, Thomas J Eichler, Geoffrey S Ibbott, Brian Kavanagh, Christopher J Schultz, and Seth A Rosenthal. American college of radiology (acr) and american society for radiation oncology (astro) practice guideline for intensity-modulated radiation therapy (imrt). *American journal of clinical oncology*, 35(6):612–617, 2012.

[61] Gary A Ezzell, Jay W Burmeister, Nesrin Dogan, Thomas J LoSasso, James G Mechalakos, Dimitris Mihailidis, Andrea Molineu, Jatinder R Palta, Chester R Ramsey, Bill J Salter, et al. Imrt commissioning: multiple institution planning and dosimetry comparisons, a report from aapm task group 119. *Medical physics*, 36(11):5359–5373, 2009.

[62] P Ortiz and M Wheatley. Lessons learned from accidental exposures in radiotherapy. *IAEA Safety Reports Series*, 17:59–61, 2000.

[63] P Scalliet et al. Comprehensive audits of radiotherapy practices: a tool for quality improvement: quality assurance team for radiation oncology (quatro). *International Atomic Energy Agency, Vienna*, 2007.

[64] Jack Valentin. *ICRP Publication 86: Prevention of Accidents to Patients Undergoing Radiation Therapy*, volume 86. Elsevier Health Sciences, 2000.

[65] IC Icrp. Preventing accidental exposures from new external beam radiation therapy technologies, icrp 112. *Ann ICRP*, 39, 2009.

[66] Norman A Baily, Richard A Horn, and Thomas D Kampp. Fluoroscopic visualization of megavoltage therapeutic x ray beams. *International Journal of Radiation Oncology* Biology* Physics*, 6(7):935–939, 1980.

[67] Wouter Van Elmpt, Leah McDermott, Sebastiaan Nijsten, Markus Wendling, Philippe Lambin, and Ben Mijnheer. A literature review of electronic portal imaging for radiotherapy dosimetry. *Radiotherapy and Oncology*, 88(3):289–309, 2008.

[68] Larry E Antonuk, John Yorkston, Weidong Huang, Jeffrey H Siewerdsen, John M Boudry, Youcef El-Mohri, and Mary Victoria Marx. A real-time, flat-panel, amorphous silicon, digital x-ray imager. *Radiographics*, 15(4):993–1000, 1995.

[69] Michael G Herman, James M Balter, David A Jaffray, Kiarin P McGee, Peter Munro, Shlomo Shalev, Marcel Van Herk, and John W Wong. Clinical use of electronic portal imaging: report of aapm radiation therapy committee task group 58. *Medical Physics*, 28(5):712–737, 2001.

[70] Coen W Hurkmans, Peter Remeijer, Joos V Lebesque, and Ben J Mijnheer. Set-up verification using portal imaging; review of current clinical practice. *Radiotherapy and Oncology*, 58(2):105–120, 2001.

[71] K A Langmack. Portal imaging. *The British Journal of Radiology*, 74(885):789–804, 2001. doi: 10.1259/bjr.74.885.740789. PMID: 11560826.

[72] Larry E Antonuk. Electronic portal imaging devices: a review and historical perspective of contemporary technologies and research. *Physics in Medicine & Biology*, 47(6):R31, 2002.

[73] D Verellen, M De Ridder, K Tournel, M Duchateau, T Reynders, T Gevaert, N Linthout, and G Storme. An overview of volumetric imaging technologies and their quality assurance for igrt. *Acta Oncologica*, 47(7):1271–1278, 2008.

[74] Joerg Rottmann, Daniel Morf, Rony Fueglistaller, George Zentai, Josh Star-Lack, and Ross Berbeco. A novel epid design for enhanced contrast and detective quantum efficiency. *Physics in Medicine & Biology*, 61(17):6297, 2016.

[75] Marios Myronakis, Josh Star-Lack, Paul Baturin, Joerg Rottmann, Daniel Morf, Adam Wang, Yue-Houng Hu, Daniel Shedlock, and Ross I Berbeco. A novel multi-layer mv imager computational model for component optimization. *Medical physics*, 2017.

[76] David A Jaffray, Jeffrey H Siewerdsen, John W Wong, and Alvaro A Martinez. Flat-panel cone-beam computed tomography for image-guided radiation therapy. *International Journal of Radiation Oncology• Biology• Physics*, 53(5):1337–1349, 2002.

[77] LE Antonuk, J Yorkston, J Boudry, MJ Longo, J Jimenez, and RA Street. Development of hydrogenated amorphous silicon sensors for high energy photon radiotherapy imaging. *IEEE Transactions on Nuclear Science*, 37(2):165–170, 1990.

[78] Youcef El-Mohri, Larry E Antonuk, John Yorkston, K-W Jee, Manat Maolinbay, Kwok Leung Lam, and JH Siewerdsen. Relative dosimetry using active matrix flat-panel imager (amfpi) technology. *Medical physics*, 26(8):1530–1541, 1999.

[79] Mark Podesta, Sebastiaan M J J G Nijsten, Lucas C G G Persoon, Stefan G Scheib, Christof Baltes, and Frank Verhaegen. Time dependent pre-treatment epid dosimetry for standard and fff vmat. *Physics in Medicine & Biology*, 59(16):4749, 2014.

[80] M Van Herk. Physical aspects of a liquid-filled ionization chamber with pulsed polarizing voltage. *Medical physics*, 18(4):692–702, 1991.

[81] H Meertens, M Van Herk, J Bijhold, and H Bartelink. First clinical experience with a newly developed electronic portal imaging device. *International Journal of Radiation Oncology• Biology• Physics*, 18(5):1173–1181, 1990.

[82] VGM Althof, JCJ De Boer, H Huizenga, JC Stroom, AG Visser, and BN Swanenburg. Physical characteristics of a commercial electronic portal imaging device. *Medical physics*, 23(11):1845–1855, 1996.

[83] BJM Heijmen, KL Pasma, M Kroonwijk, VGM Althof, JCJ De Boer, AG Visser, and H Huizenga. Portal dose measurement in radiotherapy using an electronic portal imaging device (epid). *Physics in Medicine & Biology*, 40(11):1943, 1995.

[84] KL Pasma, M Kroonwijk, JCJ De Boer, AG Visser, and BJM Heijmen. Accurate portal dose measurement with a fluoroscopic electronic portal imaging device (epid) for open and wedged beams and dynamic multileaf collimation. *Physics in Medicine & Biology*, 43(8):2047, 1998.

[85] BMC McCurdy and PB Greer. Dosimetric properties of an amorphous-silicon epid used in continuous acquisition mode for application to dynamic and arc imrt. *Medical physics*, 36(7):3028–3039, 2009.

[86] Awusi Kavuma, Martin Glegg, Garry Currie, and Alex Elliott. Assessment of dosimetrical performance in 11 varian a-si500 electronic portal imaging devices. *Physics in Medicine & Biology*, 53(23):6893, 2008.

[87] Peter B Greer. Correction of pixel sensitivity variation and off-axis response for amorphous silicon epid dosimetry. *Medical physics*, 32(12):3558–3568, 2005.

[88] Leah N McDermott, RJW Louwe, J-J Sonke, MB Van Herk, and Ben J Mijnheer. Dose–response and ghosting effects of an amorphous silicon electronic portal imaging device. *Medical physics*, 31(2):285–295, 2004.

[89] Peter Winkler, Alfred Hefner, and Dietmar Georg. Dose-response characteristics of an amorphous silicon epid. *Medical physics*, 32(10):3095–3105, 2005.

[90] Mukhtar Alshanqity and Andrew Nisbet. Dosimetric performance of a-si electronic portal imaging devices. *International Journal of Medical Physics, Clinical Engineering and Radiation Oncology*, 5(02):162, 2016.

[91] C Kirkby and R Sloboda. Consequences of the spectral response of an a-si epid and implications for dosimetric calibration. *Medical physics*, 32(8):2649–2658, 2005.

[92] Boyd MC McCurdy, Kurt Luchka, and Stephen Pistorius. Dosimetric investigation and portal dose image prediction using an amorphous silicon electronic portal imaging device. *Medical physics*, 28(6):911–924, 2001.

[93] Brian W King, Daniel Morf, Peter Greer, et al. Development and testing of an improved dosimetry system using a backscatter shielded electronic portal imaging device. *Medical physics*, 39(5):2839–2847, 2012.

[94] DA Roberts, JM Moran, LE Antonuk, Y El-Mohri, and BA Fraass. Charge trapping at high doses in an active matrix flat panel dosimeter. *IEEE Transactions on Nuclear Science*, 51(4):1427–1433, 2004.

[95] Jeffrey V Siebers, Jong Oh Kim, Lung Ko, Paul J Keall, and Radhe Mohan. Monte carlo computation of dosimetric amorphous silicon electronic portal images. *Medical physics*, 31(7):2135–2146, 2004.

[96] C Kirkby and R Sloboda. Comprehensive monte carlo calculation of the point spread function for a commercial a-si epid. *Medical physics*, 32(4):1115–1127, 2005.

[97] Samuel J Blake, Philip Vial, Lois Holloway, Peter B Greer, Aimee L McNamara, and Zdenka Kuncic. Characterization of optical transport effects on epid dosimetry using geant4. *Medical physics*, 40(4), 2013.

[98] Daniel W Bailey, Lalith Kumaraswamy, Mohammad Bakhtiari, Harish K Malhotra, and Matthew B Podgorsak. Epid dosimetry for pretreatment quality assurance with two commercial systems. *Journal of applied clinical medical physics*, 13(4):82–99, 2012.

[99] Zheng Chang, Qiuwen Wu, Justus Adamson, Lei Ren, James Bowsher, Hui Yan, Andrew Thomas, and Fang-Fang Yin. Commissioning and dosimetric characteristics of truebeam system: composite data of three truebeam machines. *Medical physics*, 39(11):6981–7018, 2012.

[100] Charbel Merheb, Clément Chevillard, Wassim Ksouri, Maher Fawzi, Marc Bollet, and Alain Toledano. Comparison between two different algorithms used for pretreatment qa via asi portal images. *Journal of applied clinical medical physics*, 16 (3):141–153, 2015.

[101] Hosang Jin, Fredrick B Jesseph, and Salahuddin Ahmad. A comparison study of volumetric modulated arc therapy quality assurances using portal dosimetry and mapcheck 2. *Progress in Medical Physics*, 25(2):65–71, 2014.

[102] Maritza A Hobson and Stephen D Davis. Comparison between an in-house 1d profile correction method and a 2d correction provided in varian's pdpc package for improving the accuracy of portal dosimetry images. *Journal of applied clinical medical physics*, 16(2):43–50, 2015.

[103] Maria Sjölin and Jens Morgenthaler Edmund. Incorrect dosimetric leaf separation in imrt and vmat treatment planning: Clinical impact and correlation with pretreatment quality assurance. *Physica Medica: European Journal of Medical Physics*, 32(7):918–925, 2016.

[104] Philip Vial, Peter B Greer, Lyn Oliver, and Clive Baldock. Initial evaluation of a commercial epid modified to a novel direct-detection configuration for radiotherapy dosimetry. *Medical physics*, 35(10):4362–4374, 2008.

[105] Daniel W Bailey, Lalith Kumaraswamy, Mohammad Bakhtiari, and Matthew B Podgorsak. A two-dimensional matrix correction for off-axis portal dose prediction errors. *Medical physics*, 40(5), 2013.

[106] K Chytyk and BMC McCurdy. Comprehensive fluence model for absolute portal dose image prediction. *Medical physics*, 36(4):1389–1398, 2009.

[107] Peter B Greer, Patrick Cadman, Christopher Lee, and Karl Bzdusek. An energy fluence-convolution model for amorphous silicon epid dose prediction. *Medical physics*, 36(2):547–555, 2009.

[108] Janett Liebich, Jörg Licher, Christian Scherf, Eugen Kara, Nadine Koch, Claus Rödel, and Ulla Ramm. Simple proposal for dosimetry with an elekta iviewgt tm electronic portal imaging device (epid) using commercial software modules. *Strahlentherapie und Onkologie*, 187(5):316, 2011.

[109] L Conte, C Mordacchini, L Pozzi, and C Vite. An empirical calibration method for an a-si portal imaging device: applications in pretreatment verification of imrt. *La radiologia medica*, 117(6):1044–1056, 2012.

[110] ME Monville, Z Kuncic, and PB Greer. Simulation of real-time epid images during imrt using monte-carlo. *Physica Medica: European Journal of Medical Physics*, 30(3):326–330, 2014.

[111] Brian W King and Peter B Greer. A method for removing arm backscatter from epid images. *Medical physics*, 40(7), 2013.

[112] Jérémy Camilleri, Jocelyne Mazurier, Denis Franck, Philippe Dudouet, Igor Latorzeff, and Xavier Franceries. 2d epid dose calibration for pretreatment quality control of conformal and imrt fields: A simple and fast convolution approach. *Physica Medica: European Journal of Medical Physics*, 32(1):133–140, 2016.

[113] Giorgia Nicolini, Eugenio Vanetti, Alessandro Clivio, Antonella Fogliata, Stine Korreman, Jiri Bocanek, and Luca Cozzi. The glaas algorithm for portal dosimetry and quality assurance of rapidarc, an intensity modulated rotational therapy. *Radiation Oncology*, 3(1):24, 2008.

[114] Benjamin E Nelms, Karl H Rasmussen, and Wolfgang A Tomé. Evaluation of a fast method of epid-based dosimetry for intensity-modulated radiation therapy. *Journal of applied clinical medical physics*, 11(2):140–157, 2010.

[115] Markus Wendling, Leah N McDermott, Anton Mans, Jan-Jakob Sonke, Marcel van Herk, and Ben J Mijnheer. A simple backprojection algorithm for 3d in vivo epid dosimetry of imrt treatments. *Medical physics*, 36(7):3310–3321, 2009.

[116] Markus Wendling, Leah N McDermott, Anton Mans, Ígor Olaciregui-Ruiz, Raul Pecharromán-Gallego, Jan-Jakob Sonke, Joep Stroom, Marcel van Herk, and Ben J Mijnheer. In aqua vivo epid dosimetry. *Medical physics*, 39(1):367–377, 2012.

[117] PM McCowan, G Asuni, T van Beek, E van Uytven, K Kujanpaa, and BMC McCurdy. A model-based 3d patient-specific pre-treatment qa method for vmat using the epid. *Physics in Medicine & Biology*, 62(4):1600, 2017.

[118] W Ansbacher. Three-dimensional portal image-based dose reconstruction in a virtual phantom for rapid evaluation of imrt plans. *Medical physics*, 33(9):3369–3382, 2006.

[119] Narges Miri, Joerg Lehmann, Kimberley Legge, Philip Vial, and Peter B Greer. Virtual epid standard phantom audit (vespa) for remote imrt and vmat credentialing. *Physics in Medicine & Biology*, 62(11):4293, 2017.

[120] SMJJG Nijsten, WJC Van Elmpt, M Jacobs, BJ Mijnheer, ALAJ Dekker, P Lambin, and AWH Minken. A global calibration model for a-si epids used for transit dosimetry. *Medical physics*, 34(10):3872–3884, 2007.

[121] Andrea Fidanzio, Alessandra Mameli, Elisa Placidi, Francesca Greco, Gerardina Stimato, Diego Gaudino, Sara Ramella, Rolando D'Angelillo, Francesco Cellini, Lucio Trodella, et al. Epid cine acquisition mode for in vivo dosimetry in dynamic arc radiation therapy. *Nuclear Instruments and Methods in Physics Research Section B: Beam Interactions with Materials and Atoms*, 266(4):658–666, 2008.

[122] Andrea Fidanzio, Savino Cilla, Francesca Greco, Laura Gargiulo, Luigi Azario, Domenico Sabatino, and Angelo Piermattei. Generalized epid calibration for in vivo transit dosimetry. *Physica Medica: European Journal of Medical Physics*, 27 (1):30–38, 2011.

[123] Andrea Fidanzio, Luigi Azario, Francesca Greco, Savino Cilla, and Angelo Piermattei. Routine epid in-vivo dosimetry in a reference point for conformal radiotherapy treatments. *Physics in Medicine & Biology*, 60(8):N141, 2015.

[124] Anthony E Millin, Rebecca S Windle, and D Geraint Lewis. A comparison of electronic portal dosimetry verification methods for use in stereotactic radiotherapy. *Physica Medica: European Journal of Medical Physics*, 32(1):188–196, 2016.

[125] K Ricketts, C Navarro, K Lane, M Moran, C Blowfield, U Kaur, G Cotten, D Tomala, C Lord, J Jones, et al. Implementation and evaluation of a transit dosimetry system for treatment verification. *Physica Medica: European Journal of Medical Physics*, 32(5):671–680, 2016.

[126] Stefano Peca and Derek W Brown. Two-dimensional in vivo dose verification using portal imaging and correlation ratios. *Journal of applied clinical medical physics*, 15(4):117–128, 2014.

[127] Markus Wendling, Robert JW Louwe, Leah N McDermott, Jan-Jakob Sonke, Marcel van Herk, and Ben J Mijnheer. Accurate two-dimensional imrt verification using a back-projection epid dosimetry method. *Medical physics*, 33(2):259–273, 2006.

[128] T Kairn, D Cassidy, PM Sandford, and AL Fielding. Radiotherapy treatment verification using radiological thickness measured with an amorphous silicon electronic portal imaging device: Monte carlo simulation and experiment. *Physics in Medicine & Biology*, 53(14):3903, 2008.

[129] Awusi Kavuma, Martin Glegg, Mohamed Metwaly, Garry Currie, and Alex Elliott. A novel method for patient exit and entrance dose prediction based on water equivalent path length measured with an amorphous silicon electronic portal imaging device. *Physics in Medicine & Biology*, 55(2):435, 2009.

[130] C Bojechko and EC Ford. Quantifying the performance of in vivo portal dosimetry in detecting four types of treatment parameter variations. *Medical physics*, 42(12): 6912–6918, 2015.

[131] K Chytyk-Praznik, E VanUytven, TA Vanbeek, PB Greer, and BMC McCurdy. Model-based prediction of portal dose images during patient treatment. *Medical physics*, 40(3), 2013.

[132] Sean L Berry, Ren-Dih Sheu, Cynthia S Polvorosa, and Cheng-Shie Wuu. Implementation of epid transit dosimetry based on a through-air dosimetry algorithm. *Medical physics*, 39(1):87–98, 2012.

[133] Tae Seong Baek, Eun Ji Chung, Jaeman Son, and Myonggeun Yoon. Feasibility study on the verification of actual beam delivery in a treatment room using epid transit dosimetry. *Radiation Oncology*, 9(1):273, 2014.

[134] Wouter van Elmpt, Sebastiaan Nijsten, Steven Petit, Ben Mijnheer, Philippe Lambin, and André Dekker. 3d in vivo dosimetry using megavoltage cone-beam ct and epid dosimetry. *International Journal of Radiation Oncology• Biology• Physics*, 73(5):1580–1587, 2009.

[135] Anton Mans, Peter Remeijer, Igor Olaciregui-Ruiz, Markus Wendling, Jan-Jakob Sonke, Ben Mijnheer, Marcel van Herk, and Joep C Stroom. 3d dosimetric verification of volumetric-modulated arc therapy by portal dosimetry. *Radiotherapy and oncology*, 94(2):181–187, 2010.

[136] R Pecharromán-Gallego, Anton Mans, Jan-Jakob Sonke, Joep C Stroom, Ígor Olaciregui-Ruiz, Marcel Herk, and Ben J Mijnheer. Simplifying epid dosimetry for imrt treatment verification. *Medical physics*, 38(2):983–992, 2011.

[137] Ben J Mijnheer, Patrick González, Igor Olaciregui-Ruiz, Roel A Rozendaal, Marcel van Herk, and Anton Mans. Overview of 3-year experience with large-scale electronic portal imaging device–based 3-dimensional transit dosimetry. *Practical radiation oncology*, 5(6):e679–e687, 2015.

[138] Eric Van Uytven, Timothy Van Beek, Peter M McCowan, Krista Chytyk-Praznik, Peter B Greer, and Boyd McCurdy. Validation of a method for in vivo 3d dose reconstruction for imrt and vmat treatments using on-treatment epid images and a model-based forward-calculation algorithm. *Medical physics*, 42(12):6945–6954, 2015.

[139] Peter Michael McCowan. in vivo patient dose verification of volumetric modulated arc therapy including stereotactic body radiation treatment applications using portal dose images. 2015.

[140] Jihyung Yoon, Jae Won Jung, Jong Oh Kim, and Inhwan Yeo. A monte carlo calculation model of electronic portal imaging device for transit dosimetry through heterogeneous media. *Medical physics*, 43(5):2242–2250, 2016.

[141] Benjamin E Nelms, Daniel Opp, Joshua Robinson, Theresa K Wolf, Geoffrey Zhang, Eduardo Moros, and Vladimir Feygelman. Vmat qa: Measurement-guided 4d dose reconstruction on a patient. *Medical physics*, 39(7Part1):4228–4238, 2012.

[142] Mu-Han Lin, Jinsheng Li, Lu Wang, Sion Koren, Jiajing Fan, Eugene Forkal, and C-M Ma. 4d patient dose reconstruction using online measured epid cine images for lung sbrt treatment validation. *Medical physics*, 39(10):5949–5958, 2012.

[143] Cecile JA Wolfs, Mariana G Brás, Lotte EJR Schyns, Sebastiaan MJJG Nijsten, Wouter van Elmpt, Stefan G Scheib, Christof Baltes, Mark Podesta, and Frank Verhaegen. Detection of anatomical changes in lung cancer patients with 2d time-integrated, 2d time-resolved and 3d time-integrated portal dosimetry: a simulation study. *Physics in Medicine & Biology*, 62(15):6044, 2017.

[144] Mark Podesta, Sebastiaan MJJG Nijsten, Julia Snaith, Marc Orlandini, Tim Lustberg, Davy Emans, Trent Aland, and Frank Verhaegen. Measured vs simulated portal images for low mu fields on three accelerator types: possible consequences for 2d portal dosimetry. *Medical physics*, 39(12):7470–7479, 2012.

[145] Jose A Baeza, Cecile JA Wolfs, Sebastiaan MJJG Nijsten, and Frank Verhaegen. Validation and uncertainty analysis of a pre-treatment 2d dose prediction model. *Physics in Medicine & Biology*, 63(3):035033, 2018.

[146] P Francescon, S Cora, and N Satariano. Calculation of kqclin, qmsrfclin, fmsr for several small detectors and for two linear accelerators using monte carlo simulations. *Medical physics*, 38(12):6513–6527, 2011.

[147] Eric E Klein, Joseph Hanley, John Bayouth, Fang-Fang Yin, William Simon, Sean Dresser, Christopher Serago, Francisco Aguirre, Lijun Ma, Bijan Arjomandy, et al. Task group 142 report: Quality assurance of medical accelerators a. *Medical physics*, 36(9Part1):4197–4212, 2009.

[148] Indra J Das, Chee-Wai Cheng, Ronald J Watts, Anders Ahnesjö, John Gibbons, X Allen Li, Jessica Lowenstein, Raj K Mitra, William E Simon, and Timothy C Zhu. Accelerator beam data commissioning equipment and procedures: Report of the tg-106 of the therapy physics committee of the aapm. *Medical physics*, 35(9): 4186–4215, 2008.

[149] Jared Starman, Josh Star-Lack, Gary Virshup, Edward Shapiro, and Rebecca Fahrig. Investigation into the optimal linear time-invariant lag correction for radar artifact removal. *Medical physics*, 38(5):2398–2411, 2011.

[150] Henry C Woodruff, Todsaporn Fuangrod, Pejman Rowshanfarzad, Boyd McCurdy, and Peter B Greer. Gantry-angle resolved vmat pretreatment verification using epid image prediction. *Medical physics*, 40(8), 2013.

[151] Igor Olaciregui-Ruiz, Roel Rozendaal, René FM van Oers, Ben Mijnheer, and Anton Mans. Virtual patient 3d dose reconstruction using in air epid measurements and a back-projection algorithm for imrt and vmat treatments. *Physica Medica*, 37: 49–57, 2017.

[152] Matthias Fippel. Fast monte carlo dose calculation for photon beams based on the vmc electron algorithm. *Medical physics*, 26(8):1466–1475, 1999.

[153] Marine Soret, Stephen L Bacharach, and Irene Buvat. Partial-volume effect in pet tumor imaging. *Journal of Nuclear Medicine*, 48(6):932, 2007.

[154] Elisabetta De Bernardi, F Fiorani Gallotta, Chiara Gianoli, F Zito, P Gerundini, and Giuseppe Baselli. Ml segmentation strategies for object interference compensation in fdg-pet lesion quantification. *Methods of information in medicine*, 49(05):537–541, 2010.

[155] Guang-hua Jin, Jin-han Zhu, Li-xin Chen, Xiao-wu Deng, Bo-tian Huang, Ke Yuan, and Xiao-wei Liu. Gantry angle-dependent correction of dose detection error due to panel position displacement in imrt dose verification using epids. *Physica Medica*, 30(2):209–214, 2014.

[156] Bin Yang, Hui Geng, Ying Ding, Chi Wah Kong, Chi Wai Cheung, Tin Lok Chiu, Wai Wang Lam, Kin Yin Cheung, and Siu Ki Yu. Development of a novel methodology for qa of respiratory-gated and vmat beam delivery using octavius 4d phantom. *Medical Dosimetry*, 2018.

[157] Sankar Arumugam, Aitang Xing, Tony Young, David Thwaites, and Lois Holloway. Three dimensional dose verification of vmat plans using the octavius 4d dosimetric system. In *Journal of Physics: Conference Series*, volume 573, page 012081. IOP Publishing, 2015.

[158] Anna Fredh, Jonas Bengtsson Scherman, Lotte S Fog, and Per Munck af Rosenschöld. Patient qa systems for rotational radiation therapy: a comparative experimental study with intentional errors. *Medical physics*, 40(3):031716, 2013.

[159] Miroslav Kubat. *An introduction to machine learning*, volume 681. Springer, 2015.

[160] Issam Naqa, Ruijiang Li, and Martin Murphy. *Machine Learning in Radiation Oncology: Theory and Applications*. Springer International Publishing, 2015. ISBN 9783319183053.

[161] Moyed Miften, Arthur Olch, Dimitris Mihailidis, Jean Moran, Todd Pawlicki, Andrea Molineu, Harold Li, Krishni Wijesooriya, Jie Shi, Ping Xia, et al. Tolerance limits and methodologies for imrt measurement-based verification qa: Recommendations of aapm task group no. 218. *Medical physics*, 45(4):e53–e83, 2018.

[162] Benjamin E Nelms, Heming Zhen, and Wolfgang A Tomé. Per-beam, planar imrt qa passing rates do not predict clinically relevant patient dose errors. *Medical physics*, 38(2):1037–1044, 2011.

[163] Shifeng Chen, Byong Yong Yi, Xiaocheng Yang, Huijun Xu, Karl L Prado, and Warren D D'souza. Optimizing the mlc model parameters for imrt in the raystation treatment planning system. *Journal of applied clinical medical physics*, 16(5): 322–332, 2015.

[164] Stephen F Kry, Paola Alvarez, Andrea Molineu, Carrie Amador, James Galvin, and David S Followill. Algorithms used in heterogeneous dose calculations show systematic differences as measured with the radiological physics center's anthropomorphic thorax phantom used for rtog credentialing. *International Journal of Radiation Oncology* Biology* Physics*, 85(1):e95–e100, 2013.

[165] Lucas CGG Persoon, Ada GTM Egelmeer, Michel C Öllers, Sebastiaan MJJG Nijsten, Esther GC Troost, and Frank Verhaegen. First clinical results of adaptive radiotherapy based on 3d portal dosimetry for lung cancer patients with atelectasis treated with volumetric-modulated arc therapy (vmat). *Acta Oncologica*, 52(7): 1484–1489, 2013.

[166] Costas D Maranas and Ali R Zomorrodi. *Optimization methods in metabolic networks*. John Wiley & Sons, 2016.

[167] Angel E Muñoz Zavala, Arturo Hernández Aguirre, Enrique R Villa Diharce, and Salvador Botello Rionda. Constrained optimization with an improved particle swarm optimization algorithm. *International Journal of Intelligent Computing and Cybernetics*, 1(3):425–453, 2008.

Acknowledgements

All praise and glory to Almighty Allah who gave me the courage and patience to carry out this work. The presented work is a result of joint forces and would not have been possible without the help and support of many people. No words could be enough to express my gratitude to them. Yet, in the following, I will try to give the credits to those who contributed to make this work and my whole PhD studies possible.

Firstly, for offering me the opportunity to work on this very fruitful topic and her unsurpassed support during my PhD journey, I would like to thank my main advisor Prof. Dr. Katia Parodi. Enormous gratitude for her encouragement, motivation, patience, guidance, insightful scientific comments, ideas and suggestions and the unlimited utilization of all resources to support me personally and to support this work. Working under the supervision of Prof. Dr. Parodi was an honor for me and truly enhance my skills scientific and personal wise.

I am especially grateful to Dr. Chiara Gianoli, my mentor during my PhD journey. She was informative, emotionally supportive and always available when needed. Her tiredness, non-complaining attitude during critical times was very encouraging. Her guidance and support were remarkable even in the period when she gave birth to her beautiful daughter Margarita. Truly, Dr. Chiara is the perfect supporter any PhD student could wish for.

I would also like to thank Dr. Sabine Reinhardt who supervised me on daily basis for the first couple of years to set the basis of this work. My thanks also go to the EPID dosimetry group. Namely, Dr. Stella Veloza for her kindness, support and valuable discussions and, the lady who sat next to me, Juliana Martins for doing everything she could to provide the mental, technical and scientific support day in and day out. A thank you note goes also to Rangoli Saxena who done a great job in a short period of time.

Since the beginning of my PhD thesis, our group has been working in close collaboration with MAASTRO clinic, Maastricht, Netherlands. I am very grateful to Dr. Mark Podesta and Prof. Dr. Frank Verhaegen for helping to initiate the EPID project at LMU, transfer their knowledge and continuing the remote support during the entire project.

Special thanks go to my fellow and friend Dr. Saad Aldawood, who introduces me at first to Prof. Dr. Parodi, and helped me with all logistics to ensure the perfect settlement in the city of Munich, and continued his genurcity by being a good friend.

For the experimental part of this thesis, I am deeply grateful to the physicists at LMU Klinikum großhadern. Especially, Sebastian Neppl who spent countless night hours helping me with measurements and was responsive and efficient whenever his help was needed. I would also like to thank Dr. Michael Reiner for sharing important information, enlightening discussions and ensuring the full support is presented in order to make our work succeed.

I am grateful to Prof. Dr. Marco Riboldi for taking the time to review this thesis as the

second referee.

I would also like to thank Dr. Peter Thirolf, Dr. George Dedes, Dr. Guillaume Landry and all the other postdoc/ staff at LS. Parodi chair for their technical support and valuable discussions during seminars and private discussions. I thank my fellow Dr. Sebastian Lehrack, Dr. Matthias Würl and Franz Englbrecht for engaging me into the German (Bavarian) culture and providing the needed support to integrate into the German system. For all my collogues at LS. Parodi chair, many thanks for making the time of my PhD delightful and joyful.

Further thanks go to my Saudi friends in Munich Dr. Sulaiman Algomiz and Ayman Alismail. True friends, I leaned on in good and tough times.

Many thanks to my colleagues at Prince Sultan military medical city Dr. Abdullah Al-rushoud, Saleh Bamajboor, Marouf Adili and Ali Zailaa for facilitating the means to make my scientific trip to their institute enlightening and scientifically helpful.

I gratefully acknowledge the funding of my PhD provided by the custodian of the two holy mosques' overseas scholarship program.

For their lifelong encouragements and unrestricted support, I would like to express my special appreciation and thanks to my parents Abdulwhab and Sarah and my brothers and sisters. Their presence fulfilled my life with blessings and happiness.

Lastly, I am indebted to my wife Nadiyah for her patience, infinite encouragements and accepting my faults during my studies. Big thanks to my daughter Bailsan and my son Omar for their sacrificing through the most important years of their lives. I hope I can compensate the time I spent away doing my research.